PALEOTSUNAMI INVESTIGATION IN SEDIMENTS OF DEMRE LAGOON (EASTERN MEDITERRANEAN)

A THESIS SUBMITTED TO
THE GRADUATE SCHOOL OF NATURAL AND APPLIED SCIENCES
OF
MIDDLE EAST TECHNICAL UNIVERSITY

BY

SERAP ŞEN

IN PARTIAL FULFILLMENT OF THE REQUIREMENTS
FOR
THE DEGREE OF MASTER OF SCIENCE
IN
GEOLOGICAL ENGINEERING

JUNE 2022

Approval of the thesis:

PALEOTSUNAMI INVESTIGATION IN SEDIMENTS OF DEMRE LAGOON (EASTERN MEDITERRANEAN)

submitted by **SERAP ŞEN** in partial fulfillment of the requirements for the degree of **Master of Science** i**n Geological Engineering, Middle East Technical University** by,

Prof. Dr. Halil Kalıpçılar
Dean, Graduate School of **Natural and Applied Sciences** _____

Prof. Dr. Erdin Bozkurt
Head of the Department, **Geological Engineering** _____

Assoc. Prof. Dr. Ulaş Avşar
Supervisor, **Geological Engineering, METU** _____

Examining Committee Members:

Prof. Dr. Ahmet Cevdet Yalçıner
Department of Civil Eng., METU _____

Assoc. Prof. Dr. Ulaş Avşar
Department of Geological Eng., METU _____

Prof. Dr. Erdin Bozkurt
Department of Geological Eng., METU _____

Prof. Dr. M. Lütfi Süzen
Department of Geological Eng.,METU. _____

Assoc. Prof. Dr. Bora Uzel
Department of Geological Eng., Dokuz Eylül Uni. _____

Date: 15.06.2022

I hereby declare that all information in this document has been obtained and presented in accordance with academic rules and ethical conduct. I also declare that, as required by these rules and conduct, I have fully cited and referenced all material and results that are not original to this work.

Name Last name : Serap Şen

Signature :

ABSTRACT

PALEOTSUNAMI INVESTIGATION IN SEDIMENTS OF DEMRE LAGOON (EASTERN MEDITERRANEAN)

Şen, Serap
Master of Science, Geological Engineering
Supervisor: Assoc. Prof. Dr. Ulaş Avşar

June 2022, 94 pages

There are historical tsunami records in the Eastern Mediterranean region, which is geodynamically active and has several tsunamigenic sources. This study aims to investigate the geological traces of these tsunamis in Demre Lagoon. In this context, ITRAX micro-XRF core scanning was performed on four cores taken from the lagoon, and their radiographic images and elemental variations were revealed. In addition, grain-size analysis was performed on 3 of the cores, and the percentage variation of the detrital sediment coarser than 125 μm along the core was found. Foraminifera abundance along the same 3 cores was also determined. According to these approaches, 9 instantaneously deposited sedimentary events were detected. These events have been stratigraphically correlated throughout the cores. Radiocarbon dating was used to date the events, and the dates of the events were determined according to the age-depth model. Accordingly, 6 of the events match the historical tsunamis of 1870 CE, 1303 CE, 1033/1068 CE, 551 CE, 365 CE, and 148 or 115 CE. The other 3 events, approximately dated to the late 2^{nd}, early 7^{th} and early 10^{th} centuries, were not correlated with any historical tsunami record. The tsunami deposits in Demre Lagoon are characterized by more homogeneous, denser, and finer-grained sediments, and depleted in Ti, Sr, Cl, and Br compared to the background sedimentation.

Keywords: Paleotsunami, Eastern Mediterranean, Demre Lagoon, Tsunami Deposits

ÖZ

DEMRE LAGÜNÜ (DOĞU AKDENİZ) ÇÖKELLERİNDE PALEOTSUNAMİ ARAŞTIRMASI

Şen, Serap
Yüksek Lisans, Jeoloji Mühendisliği
Tez Yöneticisi: Doç. Dr. Ulaş Avşar

Haziran 2022, 94 sayfa

Jeodinamik olarak aktif olan ve birçok tsunamijenik kaynağa sahip olan Doğu Akdeniz bölgesinde tarihsel tsunami kayıtları mevcuttur. Bu çalışma, Demre Lagünü'ndeki tsunamilerin jeolojik izlerini araştırmayı amaçlamaktadır. Bu kapsamda lagünden alınan dört adet karot üzerinde ITRAX mikro-XRF taraması yapılarak radyografik görüntüler ve jeokimyasal veriler elde edilmiştir. Ayrıca karotlardan üçü üzerinde tane-boyutu analizi yapılmış ve karot boyunca 125 μm'den iri taneli kırıntılı tortulların değişimi hesaplanmıştır. Ek olarak, aynı üç karotta 4 cm'de bir foraminifer bolluğu belirlenmiştir. Yapılan analiz sonuçlarına göre, tsunamiler ile ilişkili olabilecek 9 sedimanter seviye tespit edilmiştir. Bu seviyeler karotlar arasında stratigrafik olarak deneştirilmiştir. Seviyelerin tarihlendirilmesinde radyokarbon tarihleme metodu kullanılmış ve seviyelerin tarihleri yaş-derinlik modeline göre belirlenmiştir. Buna göre, tespit edilen olaylardan altı tanesi M.S. 1870, 1303, 1033/1068, 551, 365 ve 148 yada 115 tarihsel tsunamileriyle eşleşmektedir. Yaklaşık olarak 2. Yüzyıl başlangıcına, 7. Yüzyıl sonuna ve 10. Yüzyıl sonuna tarihlendirilen diğer 3 olay ise herhangi bir tarihsel tsunami kaydı ile ilişkilendirilememiştir. İncelenen tsunami çökelleri istifin geri kalanına kıyasla daha homojen, yoğun ve ince-taneli çökellerle karakterize edilmekte olup, Ti, Sr, Cl ve Br konsantrasyonları da istifin geri kalanına kıyasla daha düşüktür.

Anahtar Kelimeler: Eski Tsunami Kayıtları, Doğu Akdeniz, Demre Lagünü, Tsunami Çökelleri

To my family…

ACKNOWLEDGMENTS

This study, supported by the European Commission “Marie Sklodowska-Curie Actions – Individual Fellowships” program, was carried out within the scope of “Towards a paleotsunami chronology in the southern Aegean and Levantine seas, Eastern Mediterranean (EASTMED-PALEOTSUNAMI)” project (#706671) hosted by the Geological Engineering Department of METU.

First of all, I wish to express my deepest gratitude to my supervisor Assoc.Prof. Dr. Ulaş Avşar for his guidance, advice, criticism, encouragements and insights throughout the research.

I would like to thank Assoc. Prof. Dr. Özgür Avşar, Mehmet Ali Baykış and Burak Sevinçer from Muğla Sıtkı Koçman University, and Bülent Tokay, Levent Tosun and Akın Çil from METU for their support in the coring process. I am grateful to Ayşegül Doğan and Damla Buse Gümüşboğa for their help in laboratory analysis, and Gamze Tanık for her comments and guidance in foraminifer investigations.

TABLE OF CONTENTS

LIST OF TABLES

TABLES

LIST OF FIGURES

FIGURES

CHAPTER 1

INTRODUCTION

The Earth is a dynamic planet and the geological processes that formed it continue to occur both below and above the surface. Many natural disasters such as earthquakes, tsunamis, volcanic eruptions, mudslides, and landslides can be caused by these geodynamic processes that are out of human control. These geohazards are responsible for many casualties. In addition to loss of life, geohazards cause substantial physical damage to buildings and key infrastructures, and economic effect owing to interruptions in transportation and communication, water supply, and energy services. Furthermore, as the World's population grows, the potential threats of geohazards are becoming more prevalent. As one of the most terrifying natural disasters, tsunamis require thorough investigation. Because escaping a tsunami is practically impossible, human life loss is one of the most significant and tragic consequences of tsunamis. Secondly, in the tsunami's run-up zone, structures are severely damaged by the waves and the retreating water. Seawater inundates coastal communities, destroying critical infrastructure, including sewage systems and potable water sources. It is not just humans who suffer when a tsunami strikes; insects, animals, plants, and other natural resources may all be wiped out. When toxic chemicals wash into the ocean, they harm marine life, killing land animals and sea creatures alike. Toxic waste and debris left behind after a natural disaster is one of the most pressing environmental concerns in tsunami-hit countries.

The 2004 Sumatra and 2011 Tohoku tsunamis, in particular, were among the most destructive tsunamis in history, affecting significant lives and infrastructure and serving as a reminder of the threats of tsunamis. The earthquake of a magnitude of 9.15 that occurred in the Indian Ocean on November 26, 2004, was the trigger of 2004 Sumatra tsunami. 280,000 people were killed across South Asia, Southeast

Asia, and East Africa, with 167,000 deaths in Sumatra (Meltzner et al., 2006; Chlieh et al., 2007; Lavigne et al., 2013). In addition to the loss of life, it was determined that this disaster directly impacted 654 municipalities and 63,977 families (the Republic of Indonesia, 2005). Further, it caused property damage of over US$4.5 billion in Aceh and North Sumatra (Leitmann, 2007). On March 11, 2011, a 9.0-magnitude earthquake off the coast of Tohoku (Japan) caused significant damage and triggered a tsunami. According to the National Police Agency of Japan (NPA, 2011), as of September 11, six months after the disaster, 15,782 individuals had died, 2,526 had gone missing, and 6,167 had been wounded. In addition, 16,9 Trillion Yen (approximately 220 Billion US $) is estimated to have been expended in total on damage caused by the tsunami, according to the Japan Cabinet Office (Thorkild et al., 2012). As a result of the tsunami, a total of 345 fires were recorded in 12 provinces (Mimura et al., 2011). Further, it should be mentioned that the tsunami's harmful impacts may be long-lasting, with the following being the most evident example. The Japanese government has stated that a former employee of the Fukushima nuclear plant destroyed by the tsunami died due to radiation exposure seven years after the disaster occurred. Suppasri et al. (2012) provided a list of tsunamis that caused loss of life between 1991 and 2011 and presented more than 20 earthquake-induced tsunamis in these 20 years. These tsunamis have caused more than 250,000 deaths (Table 1.1).

Table 1.1 Tsunamis that caused loss of life between 1991-2011 (Suppasri et al., 2012).

Year	Location	Deaths	Earthquake magnitude	Tsunami Index	Maximum tsunami height (m)	Tsunami Magnitude
1991	Costa Rica	2	7.6	5.14	3.0	1.58
1992	Nicaragua	170	7.7	5.30	9.9	3.31
1992	Flores Sea, Indonesia	1169	7.8	6.66	26.2	4.71
1993	Okushiri, Japan	208	7.7	7.01	32.0	5.00
1994	Java, Indonesia	250	7.8	7.04	13.9	3.80
1994	Halmahera, Indonesia	1	6.8	5.40	3.0	1.58
1994	Mindoro, Philippines	81	7.1	5.29	7.3	2.87
1995	Mexico	1	8.0	6.08	11.0	3.46
1996	Sulawesi, Indonesia	9	7.9	6.19	3.4	1.78
1996	North Peru	12	7.5	6.16	5.1	2.35
1996	Irian Jaya, Indonesia	110	8.2	6.90	7.7	2.94
1999	Vanuatu	5	7.5	5.68	6.6	2.72
2001	Southern Peru	26	8.4	6.23	7.0	2.81
2004	Sumatra, Indonesia	227 898	9.3	7.96	50.9	5.67
2005	Sumatra, Indonesia	10	8.7	5.89	3.0	1.58
2006	Seram, Indonesia	4	6.7	5.50	3.5	1.81
2006	Java, Indonesia	802	7.7	6.76	10.0	3.32
2007	Solomon Islands	52	8.1	7.05	12.1	3.60
2009	Samoa Islands	192	8	7.54	22.4	4.48
2010	Southern Chile	156	8.8	7.43	29.0	2.81
2010	Sumatra, Indonesia	431	7.7	6.97	7.0	4.86
2011	East Japan	19 294	9.0	7.61	40.5	5.34

There have been 20 tsunamis in the last 2000 years, causing more than 3000 deaths (Table 1.2). While most of these earthquakes occurred in the Pacific, some examples also happened in the Mediterranean.

Table 1.2 Historical tsunamis around the world causing more than 3000 loss of life (Suppasri et al., 2012).

Year	Earthquake location	Magnitude *M*	Focal depth (km)	Estimated death or missing
365	Crete, Greece	8.0		5700
1498	Enshunada Sea, Japan	8.6	1	31 000
1586	Ise Bay, Japan	8.2		8000
1605	Nankaido, Japan	7.9		5000
1611	Sanriku, Japan	8.1		5000
1687	Southern Peru	8.5	30	*5000
1703	Boso Peninsula, Japan	8.2	1	*5233
1707	Nankaido, Japan	8.4	1	30 000
1746	Central Peru	8.0	30	4800
1755	Lisbon, Portugal	8.5		60 000
1771	Ryukyu Islands, Japan	7.4	1	13 486
1854	Nankaido, Japan	8.4		3000
1896	Sanriku, Japan	8.5	1	*27 122
1933	Sanriku, Japan	8.4	25	3000
1941	Andaman Sea, India	7.6	55	5000
1945	Makran, Pakistan	8.0		4000
1952	Kamchatka, Russia	8.5	45	4000
1976	Moro Gulf, Philippines	8.1	33	4456
2004	Banda Aceh, Indonesia	9.2	30	*227 898
2011	East Japan	9.0	24	*19 296

Several mechanisms can lead to tsunamis, including submarine earthquakes, landslides, submarine volcanic eruptions, and or meteorite impacts in the ocean. Additionally, a disruption that replaces a big water body from its stability point might also result in a tsunami (Haugen et al., 2005., Tappin, 2017a). Abrupt displacement of the water body into the vertical position causes the stability of water surface to be disrupted. Because a bulge in water is not stable, the surface of water tends to return to its horizontal position. The higher the water level rises, the lower the water level falls, giving birth to a sequence of waves that spread in all directions from the earthquake's epicenter, known as a tsunami (Tappin, 2017a).

Earthquakes are the most prevalent cause of tsunamis. According to the research conducted by Papadopoulos (2016), 84% of the tsunamis that occurred in the past were tectonically-induced (Figure 1.1). During an earthquake, tension builds up on

both sides of the rock as the crust deforms up to a specific limit. The fault remains trapped until the strain in the rock on either side of the fault overcomes the friction. A rapid fracture happens when cumulative strain surpasses the strength of the rock. When an earthquake occurs, the rock snaps back into an unstrained state, releasing energy that causes seismic waves (Scholz, 2019). The abrupt release of energy caused by a submarine earthquake the potential to cause a large volume of water to be displaced, resulting in a tsunami. Earthquakes on all types of faults, including strike-slip faults, normal faults, and reversal faults, can generate tsunamis. While it is most widespread on reverse faults, tsunamis triggered by earthquakes on strike-slip faults are extremely rare. However, if the sea bottom morphology is highly rough (i.e., seamounts), strike-slip faults have potential to generate tsunami by displacing large body of water (Scott, 2021).

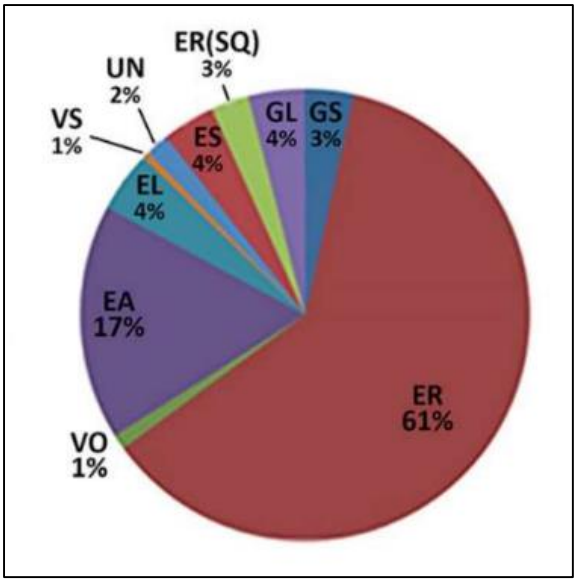

Figure 1.1 The proportion of causes of past tsunamis (Papadopoulos, 2016). ER: earthquake; EA: earthquake associated; EL: earthquake landslide; ES: earthquake marine slide; VO: volcanic activity; VS: volcanic marine slide; UN: unknown; GL: gravity landslide; GS: gravity marine slide; ER(SQ): Seaquake.

Landslides are another phenomenon that can trigger tsunamis. Both submarine and subaerial landslides occurring close to a body of water and causing massive water

body displacement also have potential to cause tsunamis (Tappin, 2017b). Submarine landslides can be caused by a variety of factors, including environmental and geological variations beneath the surface of the ocean. Predominantly caused by weak geological layers, overpressure resulting from rapid accumulation of sedimentary deposits, earthquakes and storm wave loading (including hurricanes), groundwater seepage and high pore water pressure, glacial loading, and overstepping (abrupt thinning of the earth's crust) (Locat and Lee, 2002; Masson et al., 2006; Mountjoy and Micallef, 2017). That is, earthquakes can generate both landslides and tsunamis. Even though undersea earthquakes may not directly create tsunamis always, they can indirectly induce one by triggering a landslide. The 7.9 magnitude earthquake on the Fairweather Fault on July 9, 1958, is one of the most well-known occurrences in history since it created a major landslide and rockslide, and therefore the landslide-generated tsunami with runup is around 525m (Miller, 1960., Ward and Day, 2010). The initial stage of a landslide is soil instability, often known as prefailure (Figure 1.2a). The degradation of stability then results in early failure and mass movement (Figure 1.2b). This mass movement also causes displacement of the water mass and the formation of a wave (Figure 1.2c). These waves radiate outward from their source (Figure 1.2d) (Tappin, 2017b).

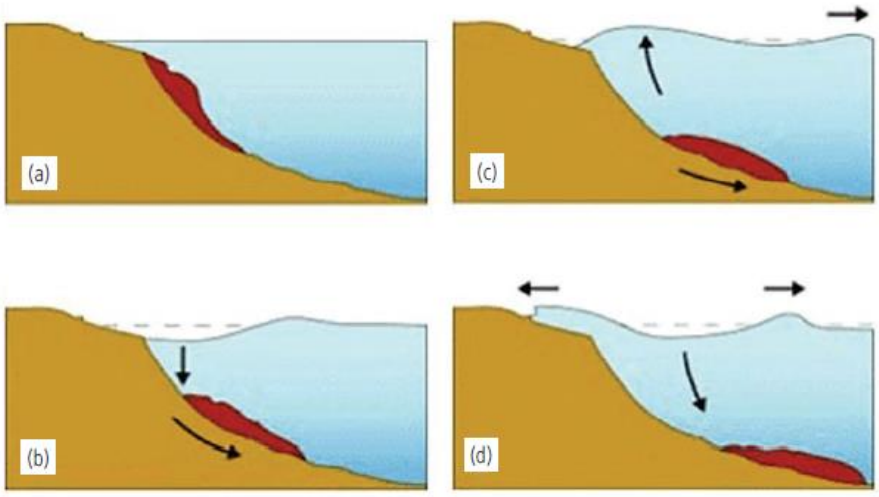

Figure 1.2 Tsunami formation triggered by a submarine landslide; a) prefailure, b) initial slip, c) wave generation, d) wave propagation (Tappin, 2017b).

Submarine volcanic eruptions are one of the mechanisms through which tsunamis are generated. According to the data from field studies, it has been determined that the stability of the water surface has deteriorated, resulting in the formation of wave motion, particularly in explosions occurring below 500 m in depth e.g. Myojinsho volcano in 1952 (Nakano et al., 1954; Morimoto and Osaka, 1955) Ritter Island in 1972 (Mastin and Witter, 2000). The Minoan eruption on the Aegean Island of Thera (also known as Santorini) in 1600 BCE was one of the most devastating eruptions in human history (Şahoğlu et al., 2021). It destroyed the Minoan settlement at Akrotiri and triggered a tsunami that caused severe damage to communities and agricultural areas on the nearby islands, including the island of Thera (Antonopoulos, 1992). Another well-known example is the tsunami that occurred in 1650 as a result of the eruption of the undersea volcano Columbo, which was located 10 kilometers east of Thera (Santorini) Island (Dominey-Howes et al., 2000a). In addition, the sedimentary traces of this tsunami are obviously visible in Karine Lagoon (W Turkey), according to the findings of the Avşar (2019b). Waves can be formed by the abrupt displacement of water triggered by a volcanic explosion, the collapse of a volcano's slope, or, more often, by a phreatomagmatic explosion and collapse of the volcanic magmatic chambers. In other words, even if the volcanic eruption does not directly result in a tsunami wave, seismic activity immediately preceding and during volcanic eruptions can produce landslides on the undersea volcano's flanks, resulting in a tsunami.

Since more than 70% of the surface of the earth is covered by water, if a meteorite hits the Earth, it will most likely end up in the ocean. A transient crater is formed in the water column depending on the impact energy and ocean depth. The ejecta splash and the collapse of the hole in the ocean produce large tsunami-like waves (Wünnemann and Weiss, 2015). When meteorites enter the atmosphere, the majority of them burn. However, incredibly giant meteorites have hit the earth in the past. The craters discovered across the planet prove this. Given the evidence of meteorites and asteroids hitting the earth and the fact that 3/4 of the earth is covered by water, it should not be underestimated that the probability of them colliding with the oceans

is high, with the potential of triggering a tsunami. However, they are rarely observed among the mechanisms that trigger tsunamis (Papadopoulos, 2016).

Looking at the factors that contribute to tsunamis, it becomes evident that the processes that caused the tsunami are interconnected and that various factors might have caused the tsunami. To elaborate, earthquakes can generate a tsunami either directly or indirectly by producing submarine or subaerial landslides, which can then cause a tsunami to occur. Tsunamis can also be caused by submarine volcanic eruptions or meteorites, which can generate them directly as well as initiate landslides and cause a tsunami. The fact that different triggering mechanisms are capable of interfering with one another is one of the reasons why tsunamis are common occurrences. From this, it is clear that the geological events that generated the tsunami are interrelated and that the tsunami could have occurred for several causes.

Since 2100 BCE, according to Gusiakov (2009), 2100 tsunami events have been marked according to their locations and have a validity index greater than one. While 1206 of these events took place in the pacific ocean, 545 took place in the Mediterranean region, which is a relatively small area, 263 in the Atlantic ocean, and 125 in the Indian Ocean (Figure 1.3). Tsunamigenic earthquakes are mostly located on the ring of fire, which means subduction zones (or converging plate boundaries) are highly potential tectonic settings to generate tsunamis. Except for limited circumstances of minor tsunamis originating along mid-ocean ridges and major transform faults, very few tsunamis have occurred in the deep ocean or central marginal seas. In other words, this illustration also might be thought of as a map of tsunamigenic earthquakes.

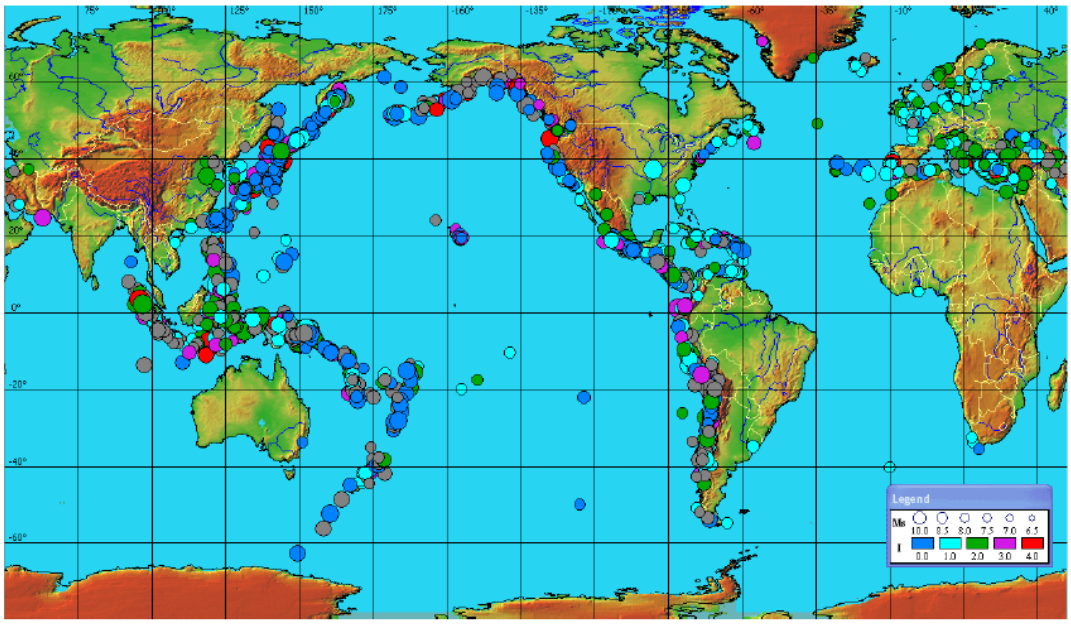

Figure 1.3 Map showing the locations and magnitudes of historical tsunamis (Gusiakov, 2009).

The most catastrophic tsunamis often occur in subduction zones near tectonic plate borders, where they may cause widespread devastation. Typically, large and shallow earthquakes occur in these zones, with the earthquake's epicenter being situated closer to the ocean's surface. A great displacement happens on the ocean floor as these plates slide over one another, resulting in destructive earthquakes. As a result of these rapid vertical displacements, the water surface becomes unstable, and sudden displacements occur within the water body, resulting in catastrophic tsunami waves. Furthermore, it should come as no surprise that more than three-quarters of all tsunamis occur in the Ring of Fire subduction zone, as seen in Figure 1.3. After formation, tsunamis radiate outward from their source across all dimensions. They have a remarkable amount of speed and energy. The speed of the tsunami is related to the ocean's depth, which means that as the depth grows, so will the speed of the wave. As the wave gets closer to the shore, the water depth drops, causing the wave to slow down and the wavelength to decrease. The total energy of the tsunami, which depends on both the wave velocity and the wave height, is conserved by increasing its height since its velocity drops as it reaches the shore due to the principle of

conservation of energy (Tan et al., 2012) (Figure 1.4). Thus seawater inundates land, where it starts to threaten our lives.

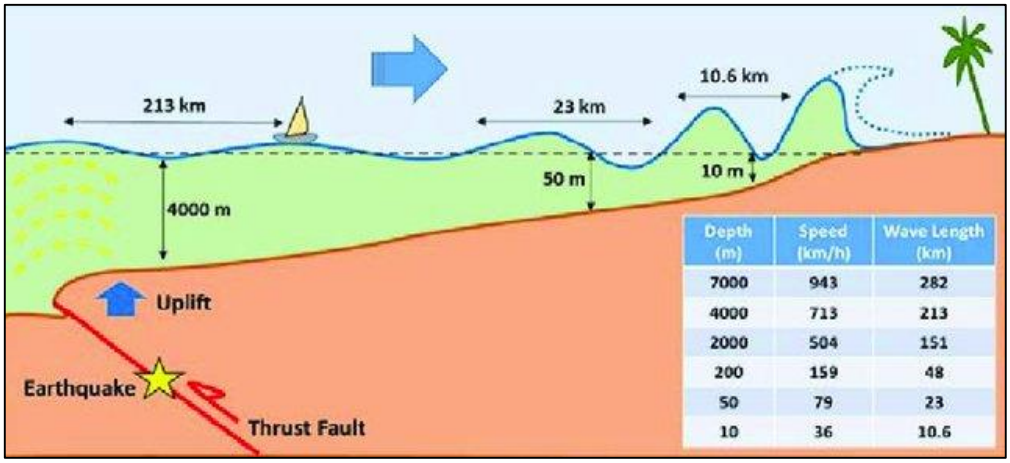

Figure 1.4 Tsunami generation model on subduction zone (Tongkul et al., 2020).

Tsunamis do not occur only in subduction zones but also at locations with normal and strike-slip faults, although they are not as common as reverse faults. Strike-slip faults, in particular, are frequently recognized as unfavorable mechanisms for tsunami genesis. However, because of the capacity for large strike-slip earthquakes to trigger landslides, particularly on a rough seafloor, they can also result in catastrophic tsunamis. Over history, several tsunamis have been triggered by strike-slip faults, including those that occurred in 1999 in Izmit, Turkey (Altinok et al., 2001), and 1994 in Mindoro, Philippines (Tanioka and Satake, 1996), and 1906 in San Francisco, California. (Geist and Zoback., 2002) Because strike-slip faults create horizontal displacement, the vertical displacements they potentially cause are frequently underestimated. On the other hand, when this type of faulting happens on steep slopes, it can also trigger tsunami waves by causing sizeable vertical displacement. Strike-slip faults on a flat and smooth sea surface can not create enough vertical displacement to cause tsunami waves (Elbanna et al., 2020). The 14 November strike-slip earthquake in Mindoro, Philippines, happened on a steep slope, which made the tsunami more powerful (Tanioka and Satake, 1996). Tsunamis were triggered by the 1999 Izmit earthquake in the Gulf of Izmit due to the strike-slip North Anatolian Fault. Small-scale normal fault components of the right-lateral

strike-slip main fault also increase the tsunami's impact. Furthermore, secondary processes produced by earthquake, such as landslides and coastline collapses, are probably due to the impacts of tsunami waves (Altinok et al., 2001). To summarize, while all faults have the potential to cause tsunamis, from highest to lowest tsunamigenic earthquakes occur due to reverse faults, normal faults, and strike-slip faults.

The African plate submerges under the Eurasian plate in the eastern Mediterranean region. This convergent boundary is characterized by the Aegean Arc in the west and the Cyprus Arc in the east (Papazachos and Papaioannou, 1999). There is a major transform fault to the east of this tectonically very active region (Dead Sea Transform Fault). Although the Pacific Ring of Fire, which is defined by subduction zones around the Pacific Ocean, has a high level of awareness of tsunami threat, paleotsunami research on tsunami hazards in the Mediterranean Sea is highly restricted. In addition, the historical tsunamis due to the extensional regime in the Aegean region have been barely studied. Tsunamis have occurred throughout history, but only a few studies have examined the geological evidence of past tsunamis and presented a paleotsunami chronology that may be employed in tsunami hazard assessments. Considering that tsunamis cause great material damage and life loss, it is necessary to clearly understand past tsunamis in order to take necessary precautions and to create possible scenarios for future tsunamis. Therefore, detailed tsunami studies are essential in the Eastern Mediterranean region.

1.1 Purpose and Scope

Finding the geological records of previous tsunamis, dating those records, and determining whether or not there is a typical recurrence interval of tsunamis are all highly significant parts of the tsunami hazard assessment process. Paleotsunami studies can be conducted in different depositional environments such as deep marine, coastal, and terrestrial environments. However, limited sedimentary records may be observed in the terrestrial environment, as deposits are open to surface conditions

and are subject to erosion. Sedimentological record is expected to be better preserved and continuous in stagnant water environments. In addition, it is more appropriate to investigate sedimentological records in coastal areas, where waves have greater influence as they approach the shore. According to Tsuji et al. (2002), while determining the study area, it is essential to choose environments with little human activity so that the interpretations in the sedimentological record are more accurate to determine. For instance, lakes with a high level of human activity, such as fishing, should not be prioritized. The regions where tsunami records can be seen in a complete form in depositional environments are coastal depositional environments, including tidal flats, enclosed water bodies, back-barrier wetlands, offshore shelves, and lagoons. (Figure 1.5). Aquatic environments, particularly coastal lakes and lagoons (Sugawara et al., 2008; Avşar, 2019a), are the ideal systems for maintaining depositional records of tsunami events. Compared to terrestrial environments, aquatic settings may be better protected from erosion and human activities. Moreover, lagoons are bodies of water, including some contact with the ocean, but which are sufficiently blocked off or sheltered to have unique environmental characteristics. Thus, it is more probable and convenient to detect the environmental changes that would interrupt the normal sedimentation, hence the tsunami traces.

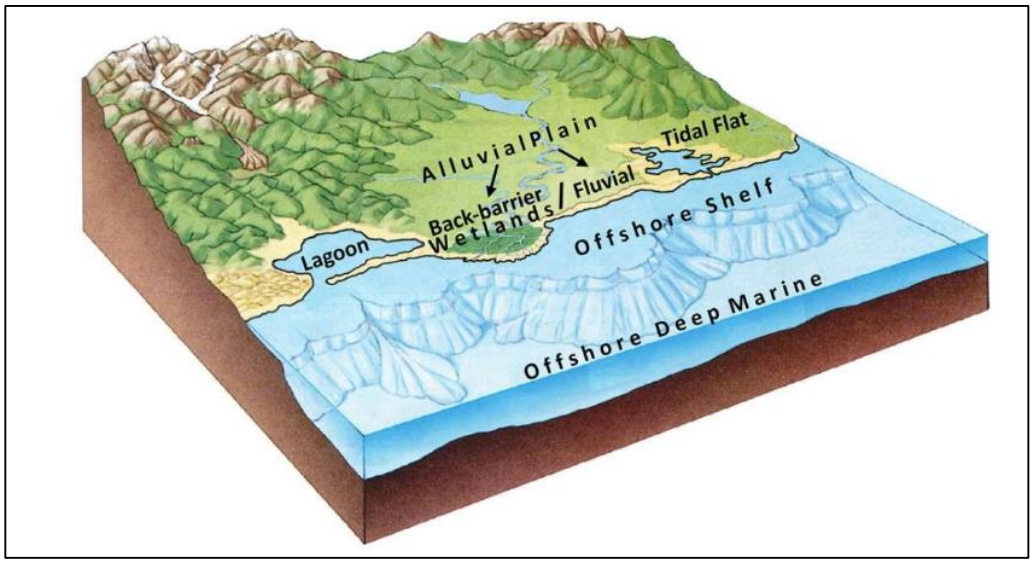

Figure 1.5 Coastal depositional environments (modified from Jones, 2001; Yeniçeri, 2020).

Tsunami waves that reach the beach have potential to transport considerable amount of material from shore to inland due to their enormous energy. Depending on the wave's energy level, the particle size of the sediment carried could differ from clay to 1 m rock fragments. While the volume of tsunami deposits is more along the shore, it is typically expected to diminish as one moves further the inland. As the wave retreats towards the sea, backwash can cause lowlands to be eroded and sediment to move toward the sea depending on its energy. These allochthon sediment depositions caused by this high-energy wave reaching the shore and retreating towards the sea cause a unique succession which gives us a clue to detect tsunami events. Identifying variations in sediment characteristics provide clues to determine tsunami-related levels. These deposits are usually investigated by using trench and coring methods. Coring applies to both terrestrial and marine settings, whereas trenching is only appropriate to the terrestrial environment. Tsunami investigations can be carried out by applying many different proxies; these can be geological evidence such as grain-size distribution, sediment composition, anisotropy of magnetic susceptibility of minerals, as well as palaeontological (e.g., shells, diatoms, foraminifera, pollen), geochemical, geomorphological, archaeological, anthropological, and paleo-

ecological demonstration (Burney, 2002., Morton et al., 2007., Goff et al., 2008a., Mamo et al., 2009 Ramírez-Herrera et al., 2009). Following the identification of paleotsunami events, the chronological record is a critical component of this research. The tsunami deposit, particularly in coastal studies, can cover vegetation, and these protected organic materials are frequently favorable for radiocarbon dating (within the margin of error). Apart from being a practical method of radiocarbon dating, it is sometimes misinterpreted. For instance, wood inside an event horizon has an intrinsic age that might vary significantly (species type, root, branch, trunk, outer bark). (Goff et al., 2012) As a result, chronology should not be determined solely on the basis of a single radiocarbon sample but rather should be complemented with additional chronology methods wherever practical, such as tephrochronology, biostratigraphy, dendrochronology, ^{137}Cs, and ^{210}Pb dating (e.g. De Martini et al., 2010).

Grain-size analysis is a frequently used proxy for detecting tsunami traces. Tsunami deposits directly reflect the origin of the sediments and the hydrodynamic conditions of the environment in which they were deposited. It frequently reveals normally graded sand due to the fluctuating hydrodynamic conditions during sedimentation. Most of the time, the deposits left by tsunamis are made up of sandy layers. Tsunami deposits are expected to be coarser than the upper and lower layers due to the potential for higher energy waves to carry coarser sediments.

Moreover, tsunami deposits are poorly sorted as a consequence of the wave's high energy and fining landward characteristics as a result of the wave's diminishing energy toward inland (Moore et al., 2007., Goff et al., 2012., Putra, 2018). Due to the decreasing hydrodynamic energy with the arrival of the tsunami wave, the order of precipitation of the particles can be seen as rock blocks, gravels, sand, silt, and clay. For this reason, it is possible to see larger grains at the bottom of the tsunami deposits, followed by a decrease in grain size. Particles such as silt and clay may settle later because they can stay suspended in water longer. Nanayama et al. (2007) used grain size and micropaleontological analyzes in a tsunami study in Kiritappu marsh along the southern Kuril Trench. In the significant tsunami levels, they found

that low-density mud and poorly-sorted marine sourced sand-rich layers were observed at these levels compared to the lower and upper layers. Kempf et al. (2017) also used the grain size method in their study examining tsunami records for 5500 years in coastal lake sediments in Southern Chile. They detected 16 tsunami levels and identified mud rip-up clasts in a sandy matrix at these levels. Additionally, massive sand, well to fairly well sand, is the most prevalent facies within the sandy layer facies association, and it includes a brown mud cap. De Martini et al. (2010) investigated tsunami records from 4,000 years of sedimentary deposit in eastern Sicily, using grain size analysis as one of their approaches. Two of the tsunami layers are relatively thin (about 10 cm), single massive, and during structureless bed, abrupt erosional lower contact. On the other hand, the remaining layers are irregular and heterogeneous beds.

Geochemical measurements is one of the most frequently used methods in tsunami investigations, especially in recent years. It is a convenient method for detecting invisible tsunamis, as it can be used to supplement other approaches when inadequate or incomplete. The main focus of these studies is the increase in the density of allochthonous material. Marine sourced materials reach the terrestrial environment during a tsunami. Then, allochthonous materials are transported from the land to the sea depending on the wave energy during the backwash (Figure 1.6). On land, geochemical changes are observed as traces of salinity or carbonate-rich sediments left by the tsunami inundation (Chagué-Goff et al., 2017). High concentrations of water-leachable ions such as K+, Na+, Ca^{2}+, Mg^{2}+, and Cl− are expected in tsunami deposits and sea level rises (Minoura and Nakaya., 1991). In the cores taken from offshore, tsunami traces are observed as catastrophic discharge deposits and contain terrestrial materials. In lagoons, however, the content of tsunami deposits within the sedimentary sequence varies according to the energy of the wave. In other words, if the wave energy is high enough to reach the land, terrestrial materials are transported during the backwash, so land-sourced materials can be observed at these levels. However, at lower energy small-wave inlets in the lagoon, the wave may not cross the lagoon and reach land. Furthermore, in this case, it is expected that there will be

a material entry into the lagoon only from the open sea. In other words, tsunami traces in the lagoon environment may give geochemical variations rich in terrestrial minerals and appear as levels rich in marine sourced minerals. Tsunami deposits may not always be observed within the inundation limits. In other words, the wave's energy may not be enough to carry the sediment up to the limit point. In such cases, using geochemical data will enable us to determine tsunami levels more precisely. Because regardless of the energy of the wave, geochemical traces of salt and marine sediments will leave traces even at the furthest point where seawater is carried.

Judd et al. (2017) analyzed Lyttelton Harbour (New Zealand) for tsunami records by using geochemistry, diatom, and sedimentological proxies. While peaks were observed in Ca, K, Si, and Sr concentrations in tsunami deposits, no change was observed in grain-size and diatom assemblages at the same levels. From this point of view, it can be said that geochemical data is a practical approach to detect low-energy tsunamis. Similarly, in the study of the south coast of Portugal records of the 1755 Lisbon tsunami, higher Si/Al and Ca/Ti values were observed compared to the lower and upper layers. In other words, a high bioclast rate was observed. In addition, as salinity indicators, Cl and Br were detected in coarse-grained tsunami sediments (Costa et al., 2012., Moreira et al., 2017). In contrast, Avşar (2019) studied the geochemical traces of tsunamis in Ölüdeniz Lagoon (South Turkey). The richness of terrestrial sediments is highlighted with low Ca and high K, Ti, Fe, and Zn contents in tsunami deposits. Schlicting and Peterson (2006) conducted paleotsunami research in back-barrier wetlands of the central Cascadia margin, USA. In this study, tsunami deposits are seen as prominent sand sheets. In the geochemical approach, Br was used to confirm marine surge origins for the anomalous sand sheets. All these studies have proven that geochemistry is an effective proxy in order to accurately determine tsunami deposits.

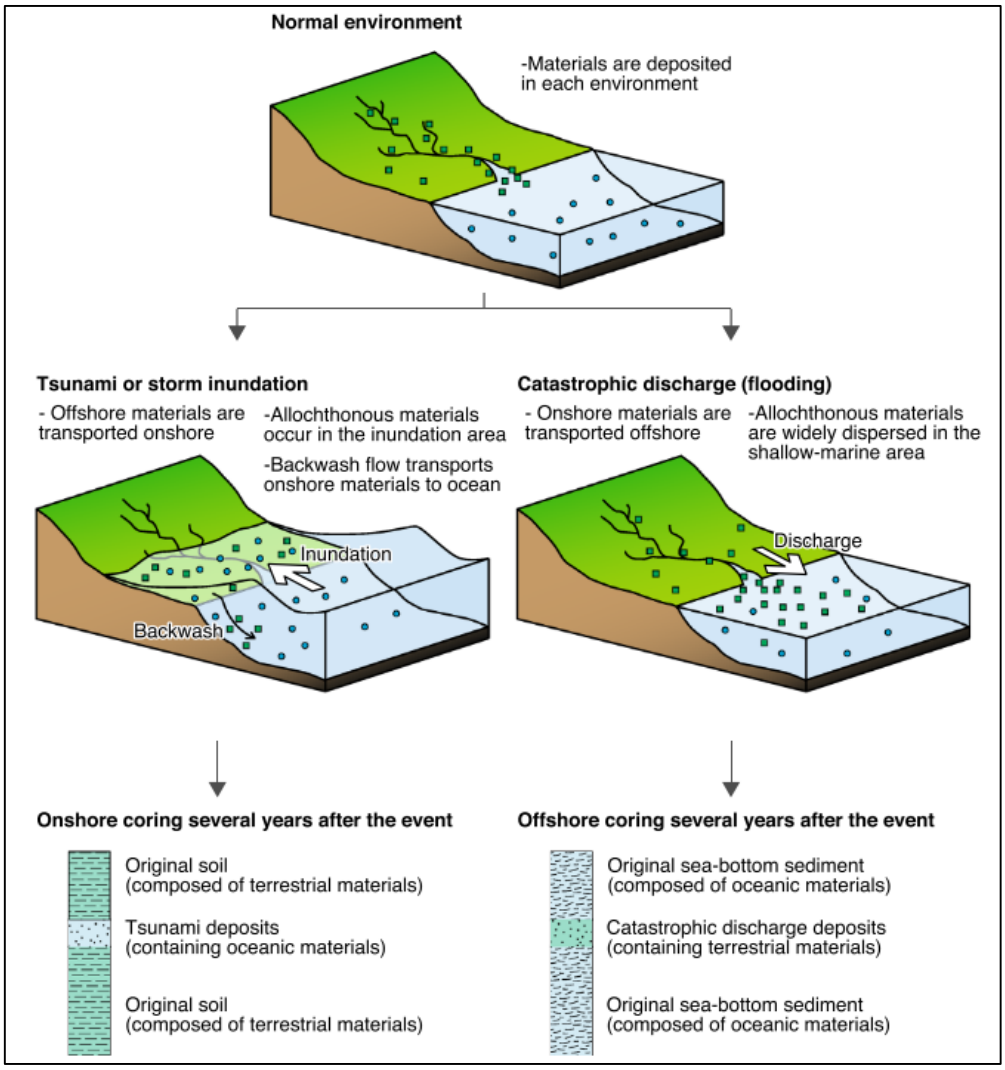

Figure 1.6 Transportation of allochthonous materials from sea to land and from land to sea and tsunami deposits preservation within a sedimentary sequence (Shinozaki, 2021).

The micro and macro paleontological approach can also be an effective method in searching for tsunami deposits. High-energy waves may bring many allochthonous marine species from the sea to the shoreline coastal system. There are many studies examining diatoms (Graehl et al., 2014), foraminifers (Pilarczyk and Reinhardt, 2012, Fischer et al., 2016), and ostracods (Ruiz et al., 2010) in sediments. Cundy et al. (2000) presented a taxonomic transition from marsh to shallow marine types that occurred abruptly. A significant foraminiferal rate at tsunami levels was found in the

Sri Lanka sediments of the 2004 Indian Ocean Tsunami, according to Dahanayake and Kulasena (2008), as well as a color difference between tsunami levels and nearshore levels. Also revealed was that the foraminifers discovered in tsunami deposits were carried from the shallow neritic zone.

This thesis aims to reveal traces of past Eastern Mediterranean tsunamis in the sedimets of Demre Lagoon. Due to the Aegean Arc, Cyprus Arc, Dead Sea Transform Fault, and the Nile Delta in the south, the Eastern Mediterranean is geodynamically active and prone to tsunami hazard. Demre Lagoon is an appropriate depositional environment for preserving the traces of past tsunamis in this region, thanks to its location and sedimentological environment. In this context, a detailed bathymetry map of the lagoon was obtained, and multi-location coring was performed. Then, ITRAX micro-XRF scanning and radiographic imaging have been applied to these cores. In addition, grain-size analysis was made, and the fraction >125 microns were photographed under a microscope. Then, varitions of abundance of foraminifera along the cores were determined from these photographs. Finally, radiocarbon dating was applied to reveal the sedimentation rate and the age of tsunami deposits in Demre Lagoon.

1.2 Study Area

Demre lagoon is located in the Eastern Mediterranean, southwest of Turkey (36.1553 N, 30.0313 E). The geology of the region is characterized by Lycian nappes, Neogene terrestrial and marine deposits, Antalya nappes, Antalya travertines, and Mesozoic carbonate platform (Figure 1.7a) The Lagoon's catchment area and its surroundings are mainly composed of the carbonates of Beydağları Formation, which consists of Jurassic-Cretaceous platform type limestones belonging to the Beydağları Autochthonous. (Günay et al., 1982; Dumont and Kerey, 1975; Poisson, 1977; Koçyiğit, 1981 and 1983; Ersoy, 1990). The Beydağları carbonate platform identified that sequences are defined by discontinuities in deposition and major facies fluctuations in both neritic and pelagic carbonates (Özgül, 1976; Poisson,

1977; Farinacci and Yeniay, 1986; Özkan and Köylüoğlu, 1988; Naz et al., 1992). The bottom of the carbonate sequence of the allochthonous unit is the Triassic dolomites. The Beydağları formation, which progressively overlays the dolomites and becomes a thick, monotonous sequence, extends from the Lower Jurassic to the Upper Cretaceous (Günay et al., 1982). Quaternary alluvial units carried by the Demre River unconformably overlie the platform carbonate units of the Upper Cretaceous Beydağları formation (Softa et al., 2018).

The study area is located in a tectonically active zone. In the southwestern portion of the area, the Kale and Kekova normal faults with a south-dipping left lateral component exist (Figure 1.7b). The Kale Fault is a normal fault along the N65E extension extending roughly 32 kilometers. This fault's eastern segment extends from the Kale towards the direction of the Kapaklı region. The western segment, on the other hand, begins at Boğazcık and extends into the sea along Stroggili Island's southwest coast (Emre et al., 2012). In Boğazcık, a transfer ramp links these two segments together (Softa et al., 2018). The Antalya normal fault is located in the northeast, while minor normal and thrust faults are dominated in the west and northwest of the region. MTA's active fault map is up to where the Demre lagoon begins. However, the site-specific study by Softa et al. (2018) presented the faults in the region in detail (Figure 1.8)

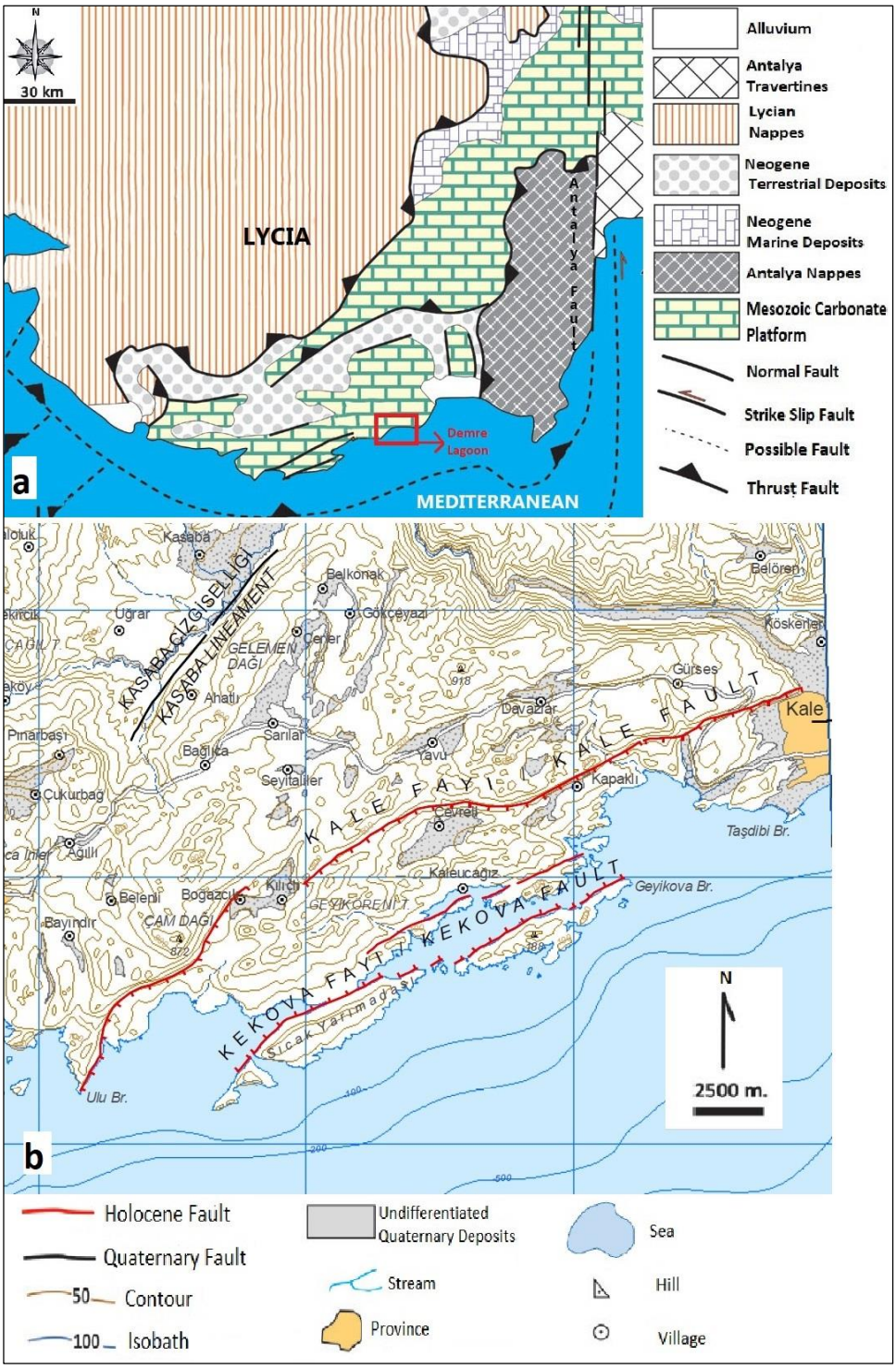

Figure 1.7 a) Geological units around Demre Lagoon (Softa et al., 2018). b) Active fault map around the study area (Emre et al., 2011).

The eastern segment of Kale Fault forms the boundary between the alluvium and the Mesozoic carbonate platform limestones (Fig. 1.8). The eastern segment of the fault starts from the Eseler region and continues through Egridere. Softa et al. (2018) made kinematic and structural measurements at two different locations on the observable 5 km part of the eastern segment of the Kale fault. Structural elements were detected on high-angle fault planes with slopes varying between 75°-82° in the two areas. When the collected data are evaluated, the paleo stress aspects that make up the fault are related to the extension in both locations. They stated that it extends approximately NW – SE. (Figure 1.8). In addition, there are many synthetic and antithetic fault sets in the south of the Kale fault, which are parallel to the fault and thought to be connected to the Kale Fault (Softa et al., 2018).

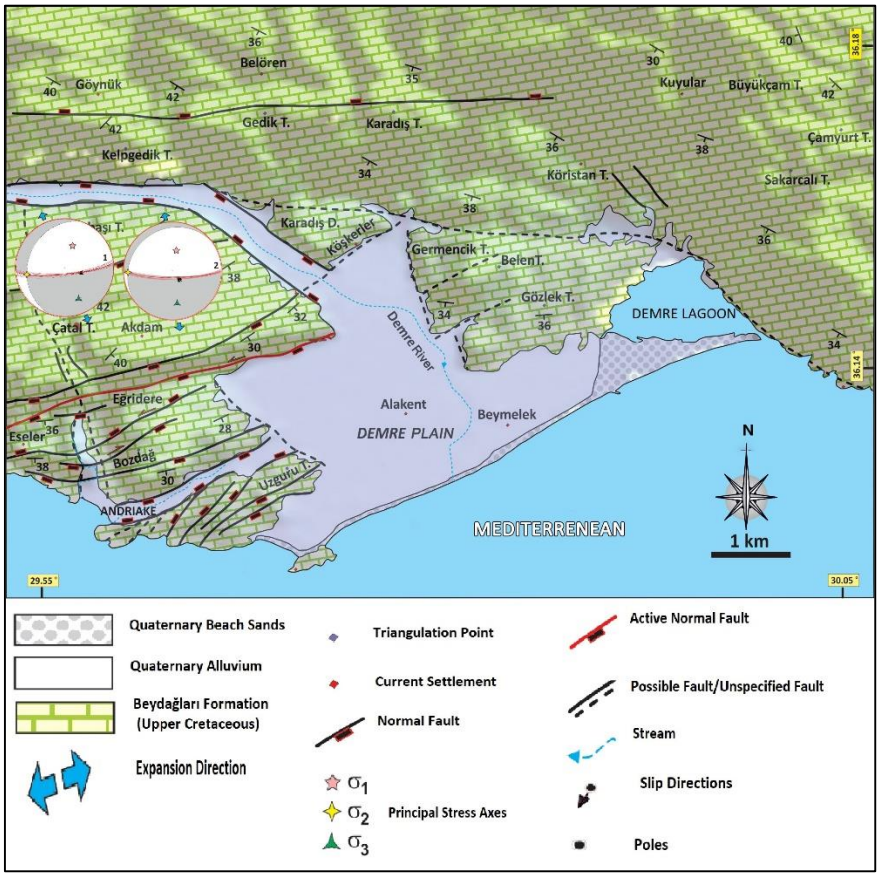

Figure 1.8 Geological map of Demre Lagoon and the surrounding area at a scale of 1/25000 (Taken from Softa et al., 2018).

On a broader scale, the geodynamically active eastern Mediterranean area is crucial because it has a number of subduction zones that can trigger tsunamigenic earthquakes. Subduction zones of great importance include the Cyrpus Arc and the Aegean Arc. The Aegean and Cyprus arcs, separated by 400 km, define the convergence of the African and Arabian plates with the Eurasian Plate and the Aegean-Anatolian Microplate, respectively (McKenzie, 1972; Dewey and Şengör, 1979; Le Pichon and Kreemer, 2010., Hall et al., 2014) Subduction Transform Edge Propagator ('STEP') fault zone that links the two. The Dead Sea Transform Fault is located southeast of the region (Figure 1.9).

Because the Eastern Mediterranean region has a diverse range of tsunamigenic sources, it is critical to conduct a thorough investigation of the region's historical tsunami records. Western Anatolia's current geological layout and recent evolution have been affected by two ongoing tectonic processes. The first is the convergence of the Arabian plate to the north and, as a result, the westward shift of the Anatolian plate along the northern and eastern Anatolian faults. The second is the and the progressive subduction of the African lithosphere northwards, which is partitioned and moving southward via the Aegean and Cyprian arcs (Şengör and Yilmaz, 1981., McKenzie, 1978; Le Pichon and Angelier, 1979; Biryol et al., 2011) Differential movement of these arcs resulted in the construction of a fault zone known as the Subduction Transform Edge Propagator ('STEP') fault zone that links these arcs. Activation of the lithospheric convergent plate causes high seismicity and volcanism. Again, since this active seismicity and volcanism can trigger subaerial and submarine landslides, landslides are also common in the region (Papadopoulos, 2016). The Nile Delta is located in the southernmost part of the Eastern Mediterranean and is the point at which the Nile River, the world's longest river, meets the sea. The sediments of this river which have high carrying capacity and energy are deposited in this area (Heidarzadeh et al.,2014; Yalciner et al., 2014). According to Ducassou et al. (2009) the area with sediment accumulation is 600kmx300km. Considering the high frequency of earthquakes in the area (El-Sayed et al.,2004) and the high sedimentation rate in the region, submarine landslides are likely to occur as also

tsunami generation (Yalciner et al., 2014). In the Eastern Mediterranean, the ground shaking is caused by a major remote earthquake (Ms>7.8), and even a modest local earthquake (Ms>6.5) would have been enough to trigger a failure Nile Delta (Garziglia et al., 2008). The Dead Sea Transform Fault is a large 1000km fracture between the Red Sea and the Taurus Mountains in the eastern Mediterranean. It is a left-lateral transform fault with an average motion of 5–7mm $year^{-1}$ (Ben-Avraham et al., 2008). This fault zone is also seismically active and has been the site of several disastrous earthquakes (Ben-Menahem 1979, Salamon et al. 1996). Based on tsunami generation probability, the eastern Aegean Arc is assigned a high rate, the Cyclades a medium rate, and the Dead Sea Transform Fault a low rate (Yolsal et al. 2007; Papadopoulos et al. 2014). Demre lagoon is completely prone to any tsunamis generated by these sources.

Historical resources also support the tsunami potential of these different sources. Papadopoulos et al. (2014) have presented a list of eastern Mediterranean past tsunamis with intensity 6 or greater (Table 1.3) and historical tsunamigenic earthquake locations. (Figure 1.9, stars) 44 major tsunami events have been identified in the last 2500 years. In this list, the events that take place incredibly close to the Demre lagoon are highlighted. Demre lagoon is a suitable area to investigate and determine the traces of tsunamis that took place in the Eastern Mediterranean since it is close to tsunamigenic sources.

Table 1.3 Historical Eastern Mediterranean tsunamis with an intensity of ≥6 (Papadopoulos et al., 2014). Tsunamis that could be recorded in Demre Lagoon are highlighted.

No	Year	Month	Day	Region	Area/*K*	*h* (cm)	ML
1	−426	Summer		Maliac Bay	8		
2	−373	Winter		W. Corinth Gulf	Helike 9		
3	148			Rhodes Isl.	Rhodes 7		
4	365	07	21	Crete Isl.	Alexandria 10		
5	447	01	26	Marmara Sea	8		
6	544			Bulgarian Black Sea	8–9		
7	551	07	09	Lebanon	8		
8	556			Cos Isl.	Cos 8		
9	749	01	18	Levantine coast	7		
10	1169	02	04	Messina Straits	8		
11	1202	05	20	Syrian cost & Cyprus	7		
12	1303	08	08	Crete Isl.	Heraklion 10		
13	1343	10	18	Marmara Sea	8	200	
14	1365	01	02	Algiers	8		
15	1389	03	20	Chios Isl.	6		
16	1402	06		Corinth Gulf	8		
17	1481	05	03	Rhodes Isl.	Rhodes 7		
18	1598	05		Turkish Black Sea	8–9		
19	1609	04		Rhodes Isl.	Rhodes 8		
20	1627	07	30	Gargano	6		−1.4
21	1650	10	11	Thera Isl.	Patmos 10	2000	+3.0
22	1693	01	11	Eastern Sicily	7		+2.3
23	1741	01	31	Rhodes Isl.	Rhodes 8		
24	1748	05	25	W. Corinth Gulf	Aeghion 9	1000	
25	1755	11	01	SW Iberia	Lisbon 10	1500	+3.8
26	1759	11	25	Levantine Sea	Akko 8		
27	1766	05	22	Marmara Sea	7		
28	1773	05	06	Tangiers	7	900	
29	1783	02	06	Calabria	9	900	−1.8
30	1817	08	23	W. Corinth Gulf	Aeghion 9	500	
31	1823	03	05	North Sicily	8		
32	1856	11	13	Chios Isl.	8		
33	1866	01	02	Albania	7		
34	1866	02	02	Kythira Isl.	Avlemonas 6	800	
35	1866	03	06	Albania	7		
36	1867	09	09	SE Peloponnese	Gythion 7		
37	1908	12	28	Messina Straits	10	1300	−0.4
38	1944	08	20	Stromboli Isl.	7		
39	1948	02	09	Karpathos Isl.	7		
40	1956	07	09	Cyclades	Astypalaea 9	1500	+3.0
41	1963	02	07	W. Corinth Gulf	7	500	−11.0
42	1979	04	15	Montenegro	8		
43	1999	08	17	Marmara Sea	6	250	
44	2002	12	30	Stromboli Isl.	Ficogrande 7	900	

The Eastern Mediterranean region's geological records of past tsunamis have been investigated, along with archival records of historical tsunamis. Although these studies are few, they will be discussed in further detail below (Figure 1.9, yellow diamonds).

Figure 1.9 Major tsunamigenic sources (Cyprus Arc, Aegean Arc, Pliny & Strabo Trenches, Dead Sea Transform Fault, Nile Delta, simplified from Barka and Reilinger, 1997), historical tsunami records (from Salamon et al., 2007 and Papadopoulos et al., 2014), and previous paleotsunami studies and geological records in Eastern Mediterranean (updated from Yeniçeri, 2020).

Salama et al. (2018) investigated the sedimentary traces caused by tsunamis in northwest Egypt, considering the historical earthquakes in the Eastern Mediterranean. Two different coastal lagoons were chosen as the study area. These lagoons, one at Kefr Saber and the other 10 km from El Alamein, are separated from the shoreline by sand dunes with a height of 2-20 meters. For paleotsunami surveys, 5 trenches of 1.5 meters were dug at Kefr Saber, and 12 cores of 1-2 meters were taken at El Alamein. These sediments were examined by X-ray, grain size analysis, total organic and inorganic material content analysis, mineralogy, and magnetic susceptibility to determine tsunami events. Then radiocarbon analysis was performed for dating. While the background sedimentation of the lagoon consists of low-energy alluvial deposits, it has been observed that the sediments associated with high-energy tsunami waves contain coarse-grained sand and broken shells together with fine sand. These levels, which they associate with high-energy waves, indicate 4 different tsunami events. According to radiocarbon dating, the dates of the events were found to be CE 365, CE 1303, and CE 1870 associated with historical earthquakes of 21 July 365 (Mw=8.4), 8 August 1303 (Mw=7.9), and 24 July 1870 (Mw=7.3) that occurred on the Egyptian coasts of the Mediterranean respectively.

Shah-Hosseini et al. (2016) investigated coastal boulder depositions on Egypt's northern shore and associated them with high-energy waves. 116 boulders of various sizes were examined in Alexandria and Marsa Matrouh. They were deposited in four distinct regions. Their weight limit reaches 23 metric tons, and their distance from the coast ranges between 6 and 40 meters. They examined geomorphological characteristics, morphometric properties, and the remains of marine animals to prove that these rock fragments were deposited by large waves. To further comprehend this probable transport scenario, they used hydrodynamic computations to establish the maximum tsunami and storm weight that might move with the stones. They conclude that the massive rocks may have reached the coast as a result of tsunami waves of 2.6 meters or storm waves reaching around 10 meters. For dating procedures, radiocarbon analysis was used to identify two distinct gastropod species buried in the rocks. According to historical accounts, the 1303 CE tsunami affected the final

orientation of the rocks, although a similar effect may have occurred due to the storm cycle. They stated that it might have been triggered by other earthquakes that took place in the Aegean Arc or other tsunamigenic faults in the Mediterranean, as well as during the Little Ice Age, during multiple high-energy storm surges. As a result, it was stated that more research is necessary on the age and source of the rocks, but regardless, Mediterranean coasts are at risk of extreme wave action.

Stanley and Bernasconi (2006) studied Holocene sedimentary deposits in the East Harbor of Alexandria. For this purpose, 7 different cores varying between 2.7 and 6.5 meters were investigated. This research was handled in terms of lithostratigraphic and chronostratigraphic, photographing, visual interpretation, and X-ray radiography applications. Marine calcareous sand, muddy sand, and muddy Holocene sediments were determined in order to interpret the sedimentation pattern of the port before and after the expansion. According to the radiocarbon data, it was stated that the carbonate-rich sand-rich sediments reached the coast by the transgression that took place in 6000 BCE. However, no direct relationship was proposed between the tsunami and the high-energy wave reaching the shore. They state that the variation in the stratigraphy may have been caused by storms, tsunamis, and human influence. It does not provide sufficient information for the Tsunami records, except for the finding that sediment degradation indicates the period 5700-5600 BCE.

Hoffmann et al. (2018) examined the sediments determined to be of anthropogenic and natural origin in coastal areas in Ashkelon, Israel. These deposits have recorded many environmental changes throughout history. Although they state that this city is essential as it has been associated with many tsunami events in the historical record, it has not yet been archaeologically proven. In this study, they examined the sedimentary sequence in the archaeological waterway exposed to erosion. Muddy strata, marine sediments rich in foraminifera, and sherds of BCE 4-5 century were observed in the sequence. In the observations made 100 m inland from the shore, the event elevation was determined to be 2.0-2.4 m above sea level. According to current observations, they claim that storms above 75 meters cannot have an effect, but this may have come with a tsunami that took place sometime after BCE 4-5 century.

From this point of view, this study emphasizes the importance of this type of sedimentological study to better understand and interpret tsunamigenic deposits.

One of the major volcanic eruptions in human history occurred on Santorini during the Late Bronze Age (ca. 1630–1550 BCE) (Friedrichet et al., 2006; Manning et al., 2006; McCoy and Heiken, 2000; Sigurdsson et al., 2006). The effect of this eruption caused tsunami-induced depositions on the coasts of Greece and Turkey. Goodman-Tchernov et al. (2009) investigated sedimentary deposits that were deposited off Caesarea Maritima, Israel due to this tsunami event. They performed coring ranging from 10 to 20 meters in length from 4 different locations. Next, they applied multiproxy methods to identify tsunami deposits from the lateral extension of previous tsunamis. The main purpose of these analyzes is to determine sediment characteristics (such as micropaleontology, and granulometry) and to separate them from large storm cycles. In this context, grain size distribution, bedding, shells of taphoecoensis, archaeological remains (pottery), visual interpretation, and radiocarbon analysis were used. A 40 cm thick sheet-like deposit was observed in one of the cores. They determined a minimum of 1 and a maximum of 3 different events. They made inferences from characterizations such as grain-size to determine whether these events were tsunami or storm-related events, with reference to previous studies (Bruins et al., 2008; Dawson and Stewart, 2007; Dominey-Howes et al., 2006; Donato et al. al., 2008; Morton et al., 2007; Reinhardt et al., 2006). Many features such as fining upward grain distribution, change or distinctive fossil assemblages (e.g, foraminifera, mollusks), well-rounded beach zone pebbles in deeper contexts can be given as examples. Moreover, tsunami deposits have very poor sorting and are capable of carrying sediments of very different sizes compared to storm-generated waves. After the analysis, 3 tsunami layers were determined in 4 different cores. They suggested that one of these layers was related to the tsunami that occurred just after the Santorini eruption. Furthermore, although the deposits of the other two events contain residues of the anthropogenic remnants of this port city, there is no similar evidence in the tsunami deposit of the Santorini eruption, owing to the city's development after the Santorini eruption. Optical evaluation (OSL) and

radiocarbon analysis of anthropogenic remains were used for dating. As a result of these analyzes, the first two events point to 1.5 ka and 2 ka years ago, respectively, while the Santorini tsunami corresponds to 1613 BC.

Morhange et al. (2006) studied coastal blocks in northern Lebanon on Tripoli islands and Byblos. It is estimated that the reason why these blocks can reach 50-100 meters inland from the shore is due to high-energy waves. In addition, the position of the blocks confirms that they may have been oriented by the waves that may come from the west. On the other hand, it is known that 3 main uplift events took place in the Region. Their dates are approximately 3000 BP in the 6th century and possibly during the 10-11th centuries (Pirazzoli, 2005). Radiocarbon analysis was applied to Dendropoma and calcareous algae contained in the blocks. They assigned 5155 ± 40 ^{14}C BP years to the blocks on Ile du Palmier, 525 ± 40 BP to the blocks on adjacent Senani, 855 ± 30 BP to the blocks at Byblos, and 710 ± 30 BP to the conglomerate block. The radiocarbon dates of the blocks do not correspond to the dates of the uplift occurrences. Consequently, they concluded that the origin of these blocks was related to tsunami events.

Whelan and Kelletat (2002) investigated geomorphological tsunami traces on two different coasts of Cyprus. Areas of study are along the coasts of Paphos in west Cyprus and Cape Greco in the east. They detected blocks 3 to 3.5 meters above sea level and spread over an area of up to 250 meters wide. They claim that these blocks were transported by tsunami waves, as they are well above the limit that storm waves can reach. In addition, there is an area stripped of vegetation and soil in the western Akamas peninsula, and they similarly indicate that these could be considered traces of a possible tsunami. As a result of the ^{14}C dating applied to the calcareous algae contained in the rocks, they conclude that these traces were formed by tsunamigenic processes that took place between 1530 and 1821 CE.

Öğretmen et al. (2015) conducted a study examining coastal boulders in Silifke on the south coast of Turkey. These boulders range in weight from 1 ton to 3.3 tons and have been associated with high-energy waves as their position extends along a

coastline. They also stated that the storms created by the coastal regions of Turkey are well above the limit they can carry. In addition, the boulders are located in a sheltered area inaccessible to the storm. Therefore, tsunamigenic processes are the most likely explanations for the rocks to reach their region. One of the blocks includes vertices, indicating an intertidal marine environment, and related samples were also discovered in the Narıkuyu area, proving this. C14 analyses were used to determine the age of vermetids. According to the results of the analysis, the blocks may have settled in the area about 1950 CE. They claim that this tsunami is historically identical to the Paphos earthquake in 1953, which occurred in the Cyprus subduction zone, but that this earthquake (M=6.2) could not have caused a tsunami of that magnitude. As a result, their opinion is that the Ecemiş Fault generated a landslide and that the landslide may have triggered a tsunami.

Bruins et al. (2008) investigated tsunami-related geoarchaeological deposits in Palaikastro (Northern Crete). The study area has a variety of geological materials, including Santorini ash and remnants from archaeological sites. The following is the evidence they offered as a tsunami path. To begin, there is erosional contact with the strata under the tsunami deposits. Second, an assemblage of marine-micro fan species was identified. Another indicator is the reworked building stone at the layer's base. Additionally, rounded beach pebbles are seen in these levels. Also, It has a diverse array of grain polarities, implying that high-energy waves validate this thesis as well. In the lowest portions of the tsunami deposit, volcanic ash mixtures were discovered indicating that it reached before the tsunami. They concluded that tsunami deposits are coeval with the Minoan Santorini eruption according to all of the geological, archaeological, and radiocarbon dating criteria.

Pirrazzoli et al. (1992) investigated sea-level changes over three geoarchaeological trenches at the archaeological site on the western coast of Crete. Considering the previous sea-level studies in the region, the trenches were discussed from a geological point of view. While previous studies have revealed six sea-level changes over a few thousand years, this study investigated the causes of these level changes. Two of them were associated with historical tsunamis. While traces of tsunami were

observed in two trenches (A and B), it was not found in C. They associated the lower level tsunami with 66 CE. They associated this level with backwash because of the increase in siliciclastics and decreased carbonates. They stated that the second event was stronger than the first event. It was emphasized that this younger and stronger tsunami corresponds to 341-439 CE, ie, the 365 CE historical tsunami.

Werner et al. (2018) carried out a multiproxy study to detect tsunami traces on the west coast of Crete. In their studies, Sougia and Palaiochora used sedimentological, geochemical, geochronological, and microfaunal approaches on coastal plains. First of all, they took 10 cores from the area and correlated them with geophysical data. They then examined the microfauna in order to identify allochthonous units. They also made a chronological order by radiocarbon analysis. Allochthonous marine fauna, the fining upward sequence, and Ca/Fe peaks indicated the introduction of marine material into the environment. They also stated that magnetic susceptibility decreased at these levels. The second event deposits in their cores are made up of poorly sorted sediments that have a bimodal grain size distribution. This is consistent with the type of high-energy inundation that is often caused by tsunamis (Scheffers and Kelletat, 2004; Scheffers and Scheffers, 2007), on the other hand, considered the second event deposits as the subsequent stage of exceptionally high-energy event deposits linked with turbulent flow conditions. According to radiocarbon analysis, event 1 was associated with the 365 CE tsunami.

Tyuleneva et al. (2018) determined the presence of tsunami deposits from Jisr al-Zarka (Caeserea, Israel) multisite with cores 15 meters below sea level. Granulometry, mineralogical studies, x-ray diffraction (XRD), x-ray fluorescence (XRF), and Fourier transform infrared spectroscopy (FT-IR) methods were used to detect the presence of backwash deposits and geochemical anomalies. ^{14}C dating was applied to determine the dates of these events. They indicated that heavy metals (Zr, Ti, and Fe) are abundant in the tsunami-related backwash deposits. Similarly, these deposits are porous and include a large proportion of bivalve shells. They determined that the tsunami traces they discovered were from the Santorini tsunamis of CE 746,

CE 115, and BCE 1613. When this analysis and the work of Goodman-Tchernov et al. (2009) are combined, more improved results for the Caesara region are obtained.

Minoura et al. (2000) studied the Aegean coast for traces of the Santorini tsunami (1613 BCE). In this context, researchers investigated these traces sequentially by digging trenches on the Didim and Fethiye coasts (western Turkey). The collapse of the Thera caldera had a maximum wave amplitude of 5m, according to the simulation approach they used. The study area's overall stratigraphy is composed of fine-medium sand grains and non-marineal layers intercalated with marine fossils. Inward thinning sand layers were observed. This layer is located just above the sand layer. The absence of an erosional contact between them indicates that they occurred as two consecutive events. The tephra thickness in the Fethiye trench approaches 10 cm. The layer underneath the tephra contains siliciclastic grains. The siliciclastic layer is found on the thick layer of plant remains and gastropods. The dating of these tephras has indicated a temporal gap of 600 years between the occurrences in Didim and Fethiye. They interpreted this as affecting the data due to mixing older crustal fragments with the sand. As a result, they emphasized that the marine deposits they examined were deposited due to the tsunami triggered by the Santorini eruption.

Alpar et al. (2012) conducted a study investigating sedimentary traces of past tsunamis in the Dalaman delta (western Turkey). This area was chosen for his research because it was considered to be an appropriate location for the recording of tsunamis caused by earthquakes, particularly in the Pliny and Strabo trenches. In order to detect these traces, they used geochemical and many different biological markers in addition to examining the sedimentological features. Some of these are zooplankton, phytoplankton, dinoflagellates, and bacteria. They collected samples from the trench walls to discover significant biomarkers. They demonstrated that the predictable ratios of these biomarkers may be utilized as evidence to demonstrate tsunami origins. Even in non-fossil units, there may be remnants of biomarkers, which might provide crucial insights. According to biochemical analyses, the age of the marine-derived deposit was determined to be around 1481 CE.

Papadapoulos et al. (2012) used the trench method to discover sedimentological traces of past tsunamis in Dalaman (western Turkey). The trench location was chosen because it is sheltered from the marine by a sandspit. They started the trench 240 meters from the beach. They discovered three distinct levels, distinguishable from the background sedimentation, consisting of silty mud and mollusk fossils (Helicostyla, Sucinea, Pormatias, and Pseudotaches). These levels are 0.30, 0.55, and 0.90 cm deep, with all of them diminishing onshore. Due to the lack of organic content, only the 0.55 cm layer was dated by ^{14}C dating. CE 1473 ±46 corresponds to this date. The first layer was identified as CE 1303 and the second as CE 1741 based on the predicted sedimentation rate (0.13 mm/year).

Avşar (2019) investigated the geochemical traces of tsunamis in the Eastern Mediterranean in the last 700 years in the sediments of Ölüdeniz lagoon. Within the scope of this research, 3 different cores of 7.5 meters in diameter, 84 cm, 99 cm, and 102 cm, were collected from the lagoon. Geochemical analyses and radiographic images were obtained using ITRAX micro-X-ray fluorescence (ɬXRF) scanning. The age-depth model was established using 137Cs and 210Pb dating. Tsunami-related levels and dates of events were determined from the graphics obtained according to the relative change of the age-depth model and element ratios. Tsunami levels were seen to be reddish-brown in color, whereas background sedimentation was observed to be yellowish-brown in color. Additionally, these levels include K and Ti; while it was abundant in Fe and Zn, it had a low rate of Ca. Three tsunami levels have been detected, and their dates correlate to CE 1303, 1609, and 1741 when related to previously known tsunamis. A link between the thickness of tsunami deposits and the magnitude of tsunamis has been found. Thus, the 1609 tsunami had a larger impact. Yeniçeri (2020) also studied on 3.5 m cores in Ölüdeniz Lagoon. In this study, ITRAX micro-XRF scanner was used to obtain high-resolution optical photographs of the cores and to determine the element change. The age-depth model was developed using radiocarbon dating. On the basis of the data collected, eight distinct sedimentary events were identified. Similarly, terrestrial minerals (Ti, Fe, and Zn) were found to be more abundant than background sediment in similar

occurrences, whereas the Ca ratio was found to be lower. Three of the events corresponded to 1609 CE, 1303 CE, and 265 CE, while the other 4 events were correlated with less known earthquakes of 746 CE, 148 CE, 142 CE, and 143 CE in the literature.

CHAPTER 2

MATERIALS AND METHODS

2.1 Bathymetric Survey and Coring

Bathymetric investigations, are the initial stage of the research conducted in aquatic environments. The goal of this step is to understand the basin geometry and to determine the core locations from the most appropriate points where sedimentation is continuous. JEOLODTÜ, a 5.5x4.5 m platform with a towing capability of 2500 kg, of the Middle East Technical University's geological engineering department, was used for this purpose (Figure 2.1a) This platform is fitted with a sonar-mounted Global Positioning System (GPS) instrument (Garmin GPS map 421s). Bathymetry research was carried out by following the survey lines in Figure 2.1b. By using the Kriging interpolation technique, the bathymetry map in Figure 2.1c was obtained. The lagoon's deepest point has been calculated to be approximately 2 meters. This bathymetry map was used to assist in determining core sites. Bathymetric survey revealed the northern boundary of the sand spit. Some of the cores were taken as close as possible to the northern edge of the sand spit. Core #5 was collected from the inner parts of the lagoon.

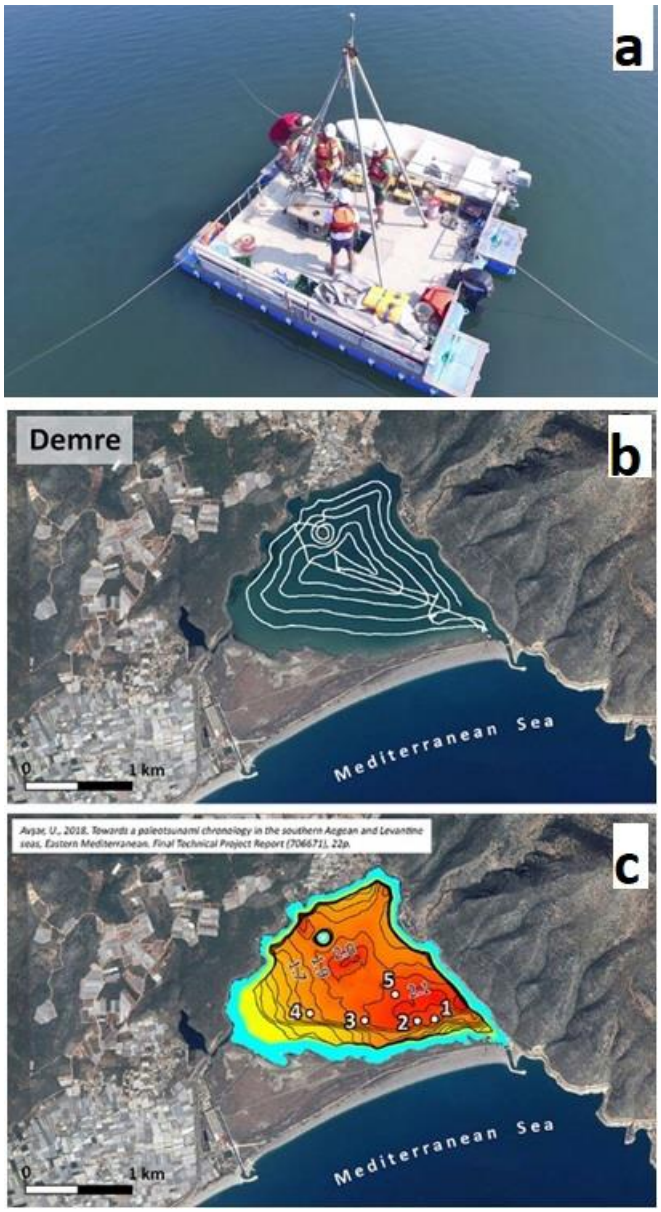

Figure 2.1 a) JEOLODTÜ coring platform used for coring in this study b) Routes followed to obtain the bathymetric map c) Bathymetric map. The white dots numbered 1 to 5 show the locations where the cores were taken.

After obtaining the bathymetry map, core locations were determined from both the part of the lagoon close to the sandpit and the inner parts of the lagoon. These points were determined from the flat and deep part of the bottom of the lagoon to maintain a consistent sedimentary succession.

Numerous techniques for coring can be selected to conduct research in sedimentary environments. Some of these methods include the gouge auger, the Russian peat corer, the piston corer, and the Mackereth corer. Each of them has a number of advantages and disadvantages that vary according to the area in which they are applied. In this study, the piston coring technique was used. This method enables the easy and efficient collecting of undisturbed sedimentary cores in aquatic environments. The piston corer's six basic components and operation order are represented in Figure 2.2: (a) core catcher, (b) piston, (c) PVC liner, (d) anvil, (e) donut hammer, and (f) guiding rod (Avşar, 2013). The core catcher is made up of spiral-shaped steel fingers that point towards the inside of the core in order to keep the sample inside the core while taking the sample and to minimize sample loss. Friction occurs between the sediment and the pipe during penetration. A piston is used to prevent the sediments from being pushed down by friction and to create a suitable vacuum. A tight attachment is made between the PVC pipe and the anvil, which is where the hammer strikes during operation. Before starting the operation, it is required to accurately determine the water depth. This is performed by anchoring the platform in three dimensions, which fixes the core in position. The hammer and piston ropes should always remain loose throughout this process; otherwise, the track will be forced upward within the pipe before hammering begins. In other words, a core is taken that is less than the length of the pipe.

After reaching the bottom, the main rope is stretched and the piston rope is locked. Thus, the system maintains its vertical position. Each time the hammer strikes, the system continues to drop. (Figure 2.2-2). The critical issue is that the piston rope must remain tight for the duration of the hammering. As a result of its looseness, it generates a vacuum decrease, which results in discontinuous sediment sequences and artificial sediment deformations. To avoid this, the ideal conditions for coring operations are stagnant water. In unsteady conditions, waves move the platform, causing the piston cable's tension to alter frequently. This has a direct effect on the sediment quality in the core. When the piston lines and main lines reach the target depth (Figure 2.2-4), they are strongly pulled. As a result, the system is separated

from the sediments (Figure 2.2-5). The core trap will be closed, preventing sediment loss while retreating. Finally, the complete system is uploaded to the platform.

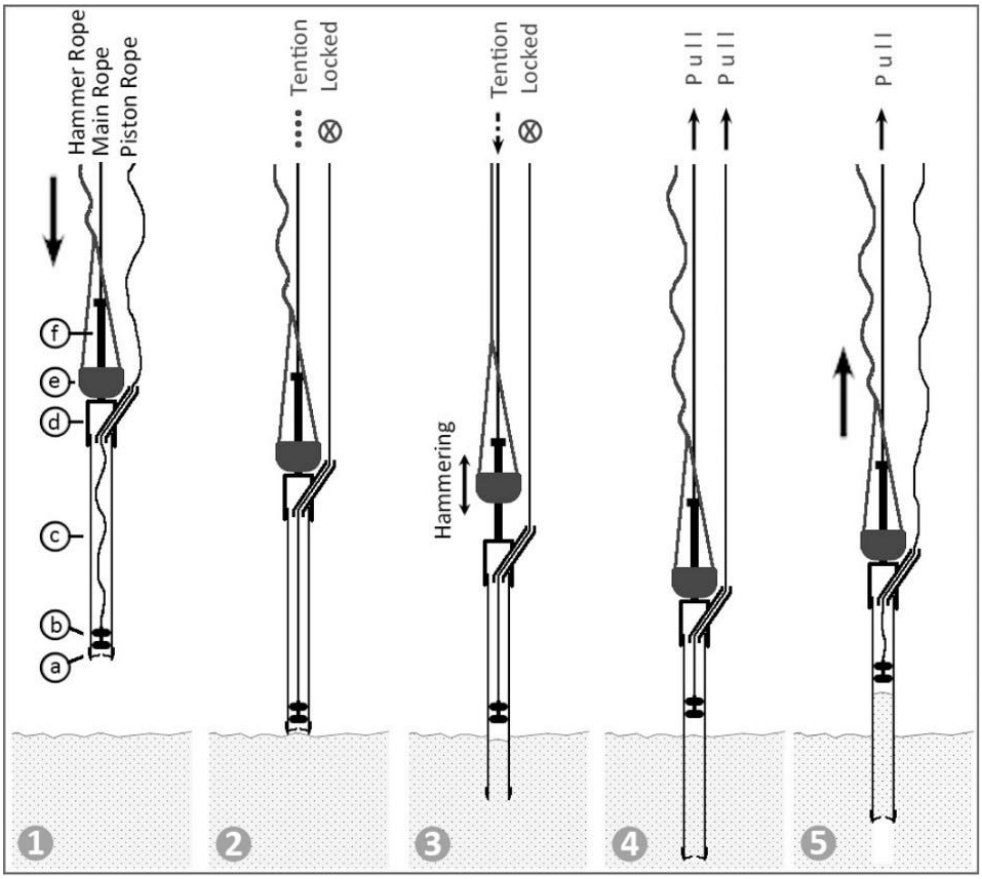

Figure 2.2 Steps of the piston coring process (Avşar, 2013).

The core locations determined by the bathymetric map are shown in Table 2.1. These points were selected from the locations where the lagoon bottom is the flattest. One of the most significant reasons for this is to avoid conditions like occasional slope failure that might disturb the continuity of the sedimentary record. Cores 5 was taken from the inner part. Other cores (1, 2, 3 and 4) were collected from the northern section of the lagoon, near the sandspit. Immediately after the coring operation, the cores were transported to the cooling room in the geological engineering department of METU and stored in the cooling room of the sediment coring and analysis lab.

Table 2.1: Data of coring locations.

Core ID	X Coordinate	Y Coordinate	Length (cm)	Water Depth (m)
DEM-1	236060	4017095	165	2.2
DEM-2	235899	4017087	365	2
DEM-3	235413	4017109	352	1.9
DEM-4	234900	4017197	354	1.7
DEM-5	235705	4017340	362	2

2.2 Core Splitting and U-Channel Extraction

The sediments are enclosed in pipelines with a length of about 2 meters. These cores are separated into two equal halves for analysis and practical shipment. When splitting a core, first the central point of the core is found, and a circular cutting line is drawn around it to ensure equal halves. Then the core is separated using a rotary blade and numbered. The cut ends of the core are tightly closed to prevent sediment dispersion.

The next step is to split the approximately one-meter core sections horizontally into two halves for further investigation of the sediments. At this point, a core cutting machine was used. The core is put horizontally on the machine and tightly fastened in place with the machine. In the parts of the machine that correspond to the right and left lateral parts of the core, there are spinning blades. To avoid disturbing the sediment and core, these blades move slowly and steadily and cut the PVC pipe outside the core equally. After cutting the PVC pipe, the core is taken from the machine and put on a flat surface. The sediment surface is separated by sliding the fishing line through the cut sides of the PVC pipe. As a result, the sediment and cores are separated into two halves horizontally. The surface is cleaned and smoothed by scraping 1-2 mm of sediment from the core. In this way, the fresh surface of the core is exposed by getting rid of oxidized sediment and irregularity. They are now suitable for u-channel extraction and further examination.

Radiographic imaging should be performed on as thin a slice of sediment as possible to show the sedimentary structures and macro-sediment components in better detail

throughout the sequence. For this reason, radiographic imaging was preferred along u-channels with a width of 2.5 cm and a thickness of 1.5 cm. The PVC channel is put in the center of the surface of the half core initially during the U-channel extraction procedure. It is then pushed into the sediment gently. Sediment is stripped from both sides of the U-side channel's walls and the u-bottom channel's surface is then sliced with the fishing line (Figure 2.3b). Then, the sediment-filled u-channel is then turned. As a result, a u-channel for radiographic imaging and micro-XRF scanning is obtained.

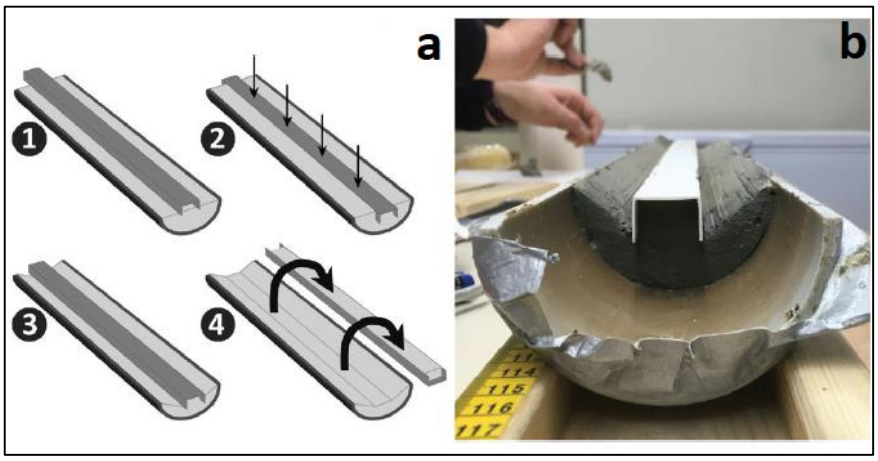

Figure 2.3 a) A diagram showing the u-channel extraction procedure. b) Side view of the core after the side sediments have been stripped during the extraction process (Avşar, 2019b).

2.3 ITRAX micro-XRF core scanning

High-resolution X-ray Fluorescence (XRF) scanning methods are effective for obtaining geochemical data in sediments along with cores from different environments, including terrestrial, marine, and lacustrine environments. The most significant reason why this method is more efficient than typical XRF analyses is that parameters such as particle size, organic matter content, mineralogy, and sediment density have minimal influence on the findings of XRF scanning (Avşar,

2013). Apart from that, standard XRF techniques need a sample preparation process that takes around two weeks, including drying and grounding samples taken from a sediment sample of around one meter in length. A sample can only be prepared every few cm in a 1 m core. However, when using XRF scanners, the core can be scanned in 1-2 hours (Croudace and Rothwell, 2015; Croudace et al., 2006). For the same sediment core segment, it was designed to collect radiographic images, as well as elemental profiles via micro-X-ray fluorescence spectrometry. The radiographic image provides precise and high-resolution optical images of cores. It is feasible to identify the bulk-sediment density, homogeneity, and macrofossil composition of the core by analyzing these images. The higher the density, the darker the image seems, whereas the lower the density, the lighter the image appears (Avşar, 2013; Yeniçeri, 2020). In order to quantitatively evaluate the results from the radiographic images, first, the images were transferred to Matlab, where these images are transferred to matrices with each cell value representing the grayscale (0 represents black, whereas 255 indicates white color) of an image pixel. Then, this matrix is transferred to Excel, and the mean, as well as standard deviation values of each matrix row, were calculated. Afterward, the mean and standard deviation values of each matrix row were multiplied and plotted against core depth to indicate the variation of the sediment heterogeneity along the core. The greater the value, the greater the degree of heterogeneity.

XRF analysis determines the elemental concentration throughout the core. It is possible to detect the elemental changes throughout the core using this approach, and it is also a valuable method for studying and interpreting the environment. This is advantageous for most research conducted in sedimentary settings. This approach allows the distinguishing of tsunami deposits from background sedimentation. The optical, radiographic, and elemental differences from split sediment cores are obtained by using the ITRAX micro-XRF core scanner used in this study.

The functional components of the ITRAX micro-XRF core scanner are shown in Figure 2.4. The following are listed in alphabetical order: optical line camera, laser triangulation system, motorized XRF detector, X-ray tub, X-ray waveguide, and X-

ray line camera. The system's operation is divided into four distinct stages. To begin, the RGB image is taken. The optical line scanning camera (Figure 2.4a) is used to obtain a radiographic image, and the X-rays released from the source reach the 0.1 mm thick and 2 cm wide flat floor folder. An X-ray camera records the number of X-rays that are emitted by the sediments after it has passed through the platform. The exact topography of the core surface along the measurement line is detected with a triangle laser system, allowing the distance between the XRF detector and the surface to be perfectly fitted. Following that, an XRF scan is conducted. The user determines the number of scan shots. It is possible to get shots as minimal as 0.2 mm.

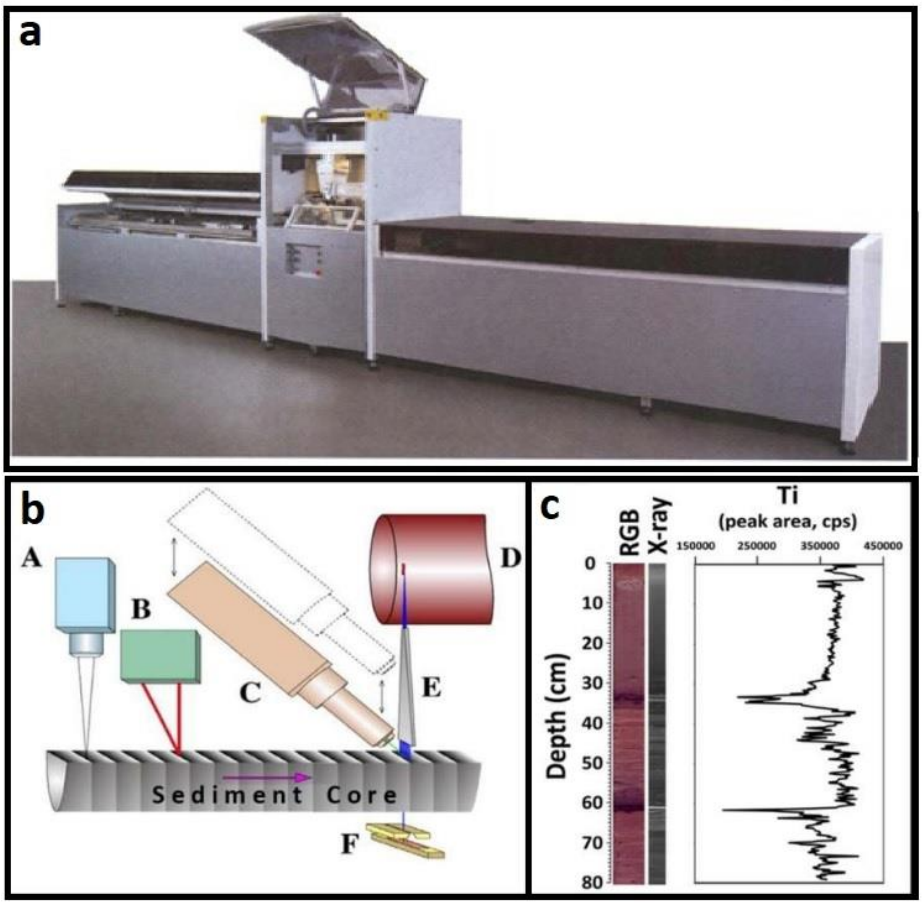

Figure 2.4 a) ITRAX micro-XRF core scanning device (Croudace et al., 2006). b) Operational components of the ITRAX micro-XRF core scanner (Croudace et al., 2006). C) An ITRAX result showing RGB monitoring, Ti element fluctuation, and radiographic image (from Boraboy Lake data of Avşar et al., 2015).

In this study, the extracted u-channels were sent to the GEOPOLAR Laboratory at Bremen University, Germany, for ITRAX micro-XRF core scanning analysis. Radiographic scanning was performed along the u-channel at a resolution of 0.2 mm. For XRF scans, this ratio has a resolution of 1 mm. There are two types of X-ray source tubes that are frequently utilized in this investigation. Molybdenum (Mo) is the first of them, and it is more appropriate for heavier elements. The second is Chromium (Cr), which is more suitable for the use of lighter elements (Croudace et al., 2006). For the purposes of this study, a molybdenum tube induced at 30 kV and 40 mA was used as the X-ray source. Every 1 mm, measurements were taken for 5 seconds. Even though using an XRF scanner for sediment cores is more advantageous than using the traditional XRF methods, factors such as water content, organic matter content, grain size variation, and surface roughness can all have an impact on XRF measurements (Croudace et al. 2006; Böning et al. 2007; Tjallingii et al. 2007; Chawchai et al. 2016). This is why all cores were scanned on the same day and using the same techniques, in order to ensure that any differences in results were not due to artifactual factors. Nonetheless, the element's ITRAX data were not directly utilised, as cores may have signs of grain size, water content, and organic matter content. Because using absolute values directly in paleoenvironmental studies gets results with a wide margin of error, comparing element ratios after standardization allows a more accurate interpretation (Croudace et al., 2006; Rothwell et al., 2006; Avşar, 2013). ITRAX data is in counts per second, which is semi-quantitative. By assuming the ITRAX dataset is normally distributed, the elemental data was standardized based on Eq. (1), in order to obtain comparable units and amplitudes for each element profile. To begin, the mean (μ) and standard deviation (σ) values were obtained for each element along the sequence. The standard value (z) was then calculated for each measurement by multiplying the difference between the measurement value at that moment and the mean by the standard deviation. When this is performed on all items along the core, the resulting data is standardized, allowing for comparison of the elements.

$$z=(x-\mu)/\sigma \qquad \text{Eq. (1)}$$

Where,

z: Standardized value, x: Data value, μ: Mean value, σ: Standart deviation

2.4 Grain-Size Analysis

Grain-size analysis is a widely used method in paleotsunami research. Although not sufficient alone, it is an important parameter for tsunami deposit identification. It gives crucial information about the origin of the transported material and the hydrodynamic conditions during deposition. In stagnant water conditions, that is, in the normal state of the lagoon, finer grains are expected to deposit. However, tsunami waves are high-energy and can carry coarser grains into the lagoon. Therefore, mean grain-size in tsunami deposits along the core is expected to be larger than the background sedimentation.

Grain-size analysis was conducted on cores 2, 3 and 5 (Figure 2.1c). The cores were subsampled at 4 cm intervals. (Figure 2.5a.) Half of these 4 cm-thick samples were saved as a backup in case further examination was needed (Figure 2.5b). The other half of the sediment was placed in labeled and pre-weighed beakers. Then, the beaker + subsampled sediment was weighed and wet sediment weights were calculated by subtracting the weight of the beaker. The top of the sediment was filled with distilled water until the beakers were filled. The water and sediment mixing process is divided into four steps: 1) 10 minutes with a magnetic stirrer (Figure 2.5c), 2) 5 minutes in an ultrasonic bath, 3) 5 minutes with a magnetic stirrer, and 4) 5 minutes in an ultrasonic bath, for a total of 25 minutes mixing with water and sediment The sediment can be totally homogenized as a result of this process. Then, the clay was poured by washing with a setup in which 1400 and 125 micron sieves were stacked on top of each other. For 10 minutes, the whole sediment was gently cleaned under the tap. The material below 125 microns was drained and removed from the sample at the end of this step. The material collected is particles larger than 1400 microns

and particles larger than 125 microns. Above 1400 microns, samples consist of very coarse-grained shells. Two different material groups taken from the same sample were placed in separate beakers and labeled. After passing distilled water over them, they were kept in the oven at 70° C for 24 hours to be dried. Again, after subtracting the beaker weights, dry sediment weights were computed. Between 125 and 1400 microns in size, there is both carbonate and clastic material. To dissolve the carbonate in this material, which extends above 125 microns, a 0.1 M HCl solution was used. The materials were stirred in 50 ml of HCl solution using a magnetic stirrer. They were then washed with distilled water and dried for 24 hours at 70° C degrees. The weight of the clastic sediment was determined by weighing this dried mater

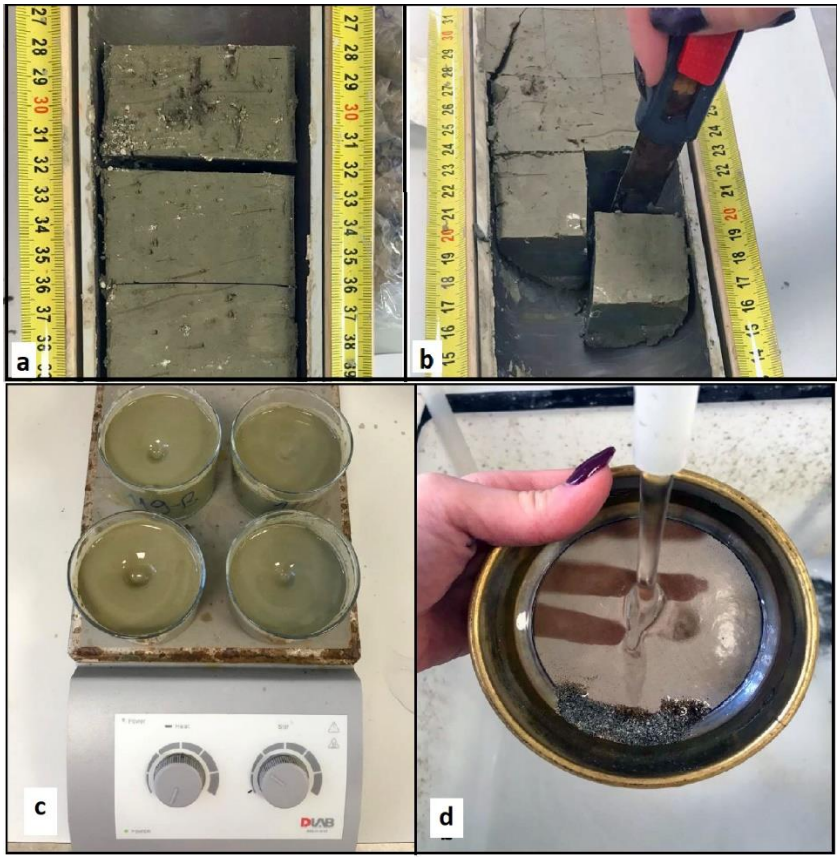

Figure 2.5 Some stages of grain size analysis; a) Marking and subsampling of half cores at 4 cm intervals b) Allocation of backup samples c) Mixing sediment and water in a magnetic stirrer d) Washed sediment remaining on 125 micron sieve.

2.5 Abundance of Foraminifera in Sediments

There is a stream feeding the lagoon in the northwest of the study area. Due to this stream, there are also flood deposits in the lagoon. Flood deposits are sediments carried from a running water source and can range in particle size from clay to gravel, depending on hydrodynamic energy (Kovács, 2013). The material transported with the flood is expected to be of terrestrial origin. In order to determine whether these geological event deposits in the sequence were caused by a tsunami or flood, the abundance of foraminifera in the lagoon sediments was determined. The foraminifera detected in the lagoon are ammonia which is a genus of sheltered and shallow marine intertidal environments (Walton and Sloan, 1990). While foraminifera is expected to be observed in background sedimentation or tsunami deposits, it is not expected to be found in flood deposits.

For this purpose, four random photographs were taken under a stereomicroscope at a magnification of x2.0 for each sample that had been subsampled, washed, and dried at 4 cm intervals. The foraminifera was marked with a blue dot on the photographs by using Adobe Photoshop 2021. Four photographs were analyzed for each sediment sample sampled at every 4 cm along the cores (2, 3 and 5). The number of foraminifera counted at each photograph per sample was noted, and an average number detected at 4 photographs was calculated for each level. Finally, the number of foraminifera along the depth of each core was plotted.

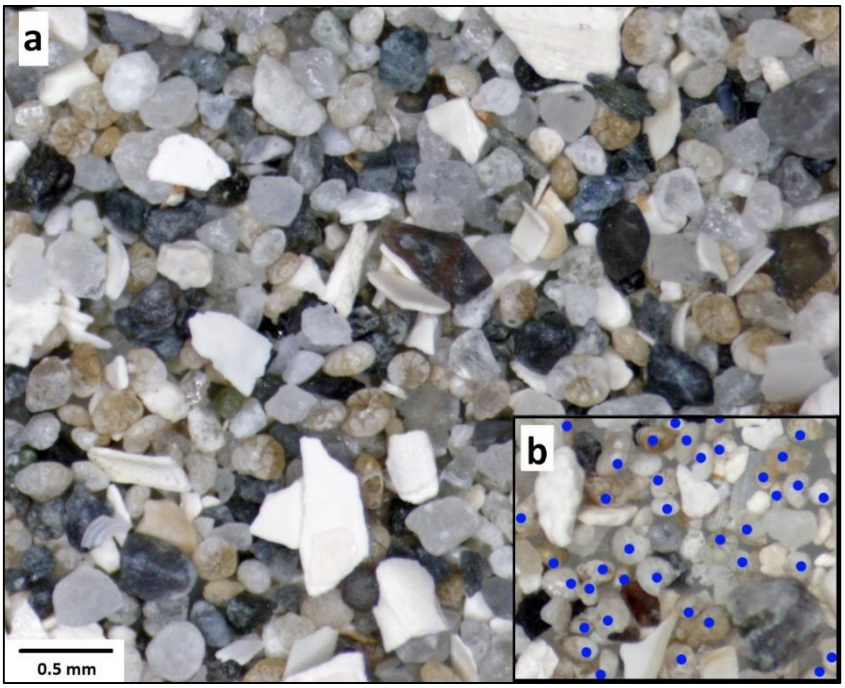

Figure 2.6 a) Sediment sample with grain size between 125 to 1400 microns. Taken with a stereo microscope after washing with distilled water. b) Marking stage to determine the abundance of foraminifera.

2.6 Radiocarbon Dating

The dating of the sediments is one of the most important steps in paleotsunami studies. It is necessary to create an age-depth model with a low margin of error to be able to accurately determine the age of tsunami deposits. In this context, different methods can be preferred. Some of the commonly used ones are cosmogenic isotope dating, uranium-series dating, and radiocarbon dating. In this study, the radiocarbon dating method was preferred because there were different organic material residues along the core.

Radiocarbon dating is based on measuring radioactive ^{14}C decay in organic tissues (Björck and Wohlfarth, 2002). Nitrogen (^{14}N) atoms and proton atoms are constantly exchanged in the top layers of the atmosphere, resulting in sustained ^{14}C production. ^{14}C atoms are quickly oxidized in the atmosphere and converted to $^{14}CO_2$. Then it

begins to be absorbed by living organisms' tissues. Until a living organism dies, the carbon in the environment is in isotopic balance with the carbon it consumes. This equilibrium, however, is disrupted after death. Although there is no $^{14}CO_2$ absorption from the atmosphere, ^{14}C decay is ongoing (Björck and Wohlfarth, 2002). The measurements of this decay are used to determine the age of tissues.

Although it is an effective and widely used approach, errors may arise owing to instrumental factors, hard water/reservoir impact, and/or contamination of young and old materials (reworking and deposition of older organic deposits, humic acid infiltration, root penetration, bioturbation, etc) Björck and Wohlfarth (2002). If allochthonous organic matter is carried into the environment, the measured age will be older than the actual age of sedimentation. The reason is that the organic material being carried may be from older species. Reaching the lower levels of plant roots growing from higher layers of the sediment, on the other hand, can be deceptive. In this situation, the age determined by tissue will be younger than the age of sedimentation (Olsson, 1991). In aquatic paleoenvironmental investigations, $CaCO_3$-containing organisms (e.g. bivalve shells) and/or organic materials carried from land (e.g. tree leaves) can be utilized for radiocarbon dating. Nonetheless, hard/reservoir water may impact aquatic organisms. For instance, the $CaCO_3$ that organisms absorb from the water may originate from limestone in the reservoir that is millions of years old, and the outcomes may be far older than the actual organism's age. Likewise, errors may occur owing to the action of glacial meltwater. In this case, the ^{14}C date may be underestimated. On the other hand, there will be no effect of hard water on the biological tissues in the terrestrial environment. There will be no such distinction between the carbon in the atmosphere and the carbon in a live organism's tissue. In paleoenvironmental research, if terrestrial organic matter remnants are detected along the core, they should be favored (Björck and Wohlfarth, 2002).

In this study, terrestrial organic matter (e.g., charcoal, burnt seed) that was detected along the core was gently removed in order to conduct radiocarbon dating (Figure 2.7). After that, distilled water was used to wipe away the sediment that had stuck on it. To assess whether it was appropriate for analysis, it was examined through a

stereomicroscope next. Finally, it was washed again with distilled water in an ultrasonic bath. Afterward, it was placed into numbered packets and prepared for analysis. The OxCal software (Bronk Ramsey, 2017) was used to calibrate primary radiocarbon dates in this investigation, which used the IntCal13 atmospheric curve developed by Reimer et al. (2013).

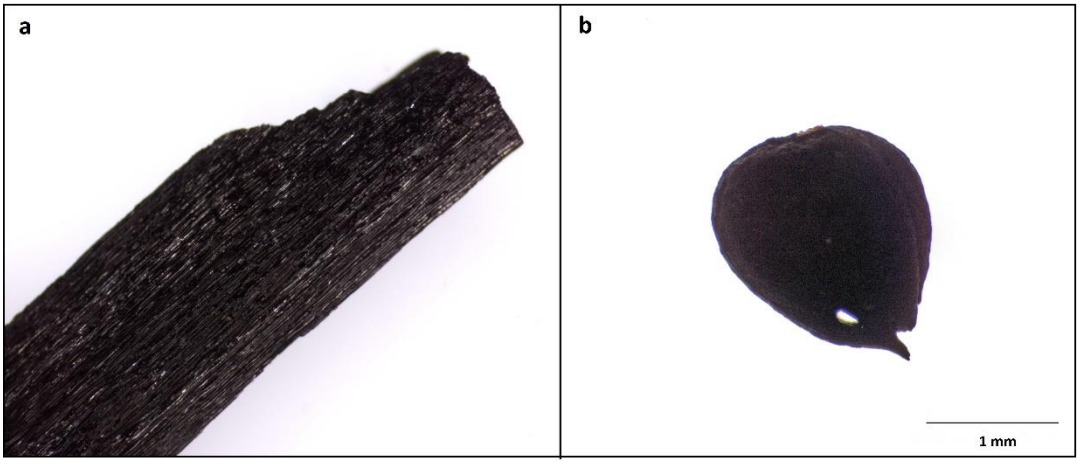

Figure 2.7 Example of extracted organic materials for radiocarbon analysis; a) Burnt twig, b) Burnt seed.

CHAPTER 3

RESULTS

3.1 Radiographic Images

Initially, the variation of sedimentary structures and characteristics along the cores were visually inspected using radiographic images. Color, density, homogeneity, grain-size variations, abundance of macrofossils, lamination, and bioturbation can be identified throughout the sequence using radiographic images. Figure 3.1 illustrates close-up views of some sample levels from the first 140 cm of DEM-4 to show different characteristics of deposits along the cores. Figure 3.1a corresponds to a core section between 3 and 8 cm. In general, this section is characterized by a heterogeneous appearance, which has a combination of dark and light tones. Gastropod fossils with oval-elliptic form and black borders have been discovered in the upper part of Figure 3.1a (G). In the bottom part, the side and the top views of the bivalve shells were observed (B). Figure 3.1b is a close-up view of sediments between 19 to 22 cm of the core. Bivalve shells are observed in the upper and lower parts, while in the middle parts, there are dispursed darker spots, which are coarse sand. These levels reflect the background sedimentation of the lagoon, which is characterized by its low sediment density, heterogeneous structure, and high biological content.

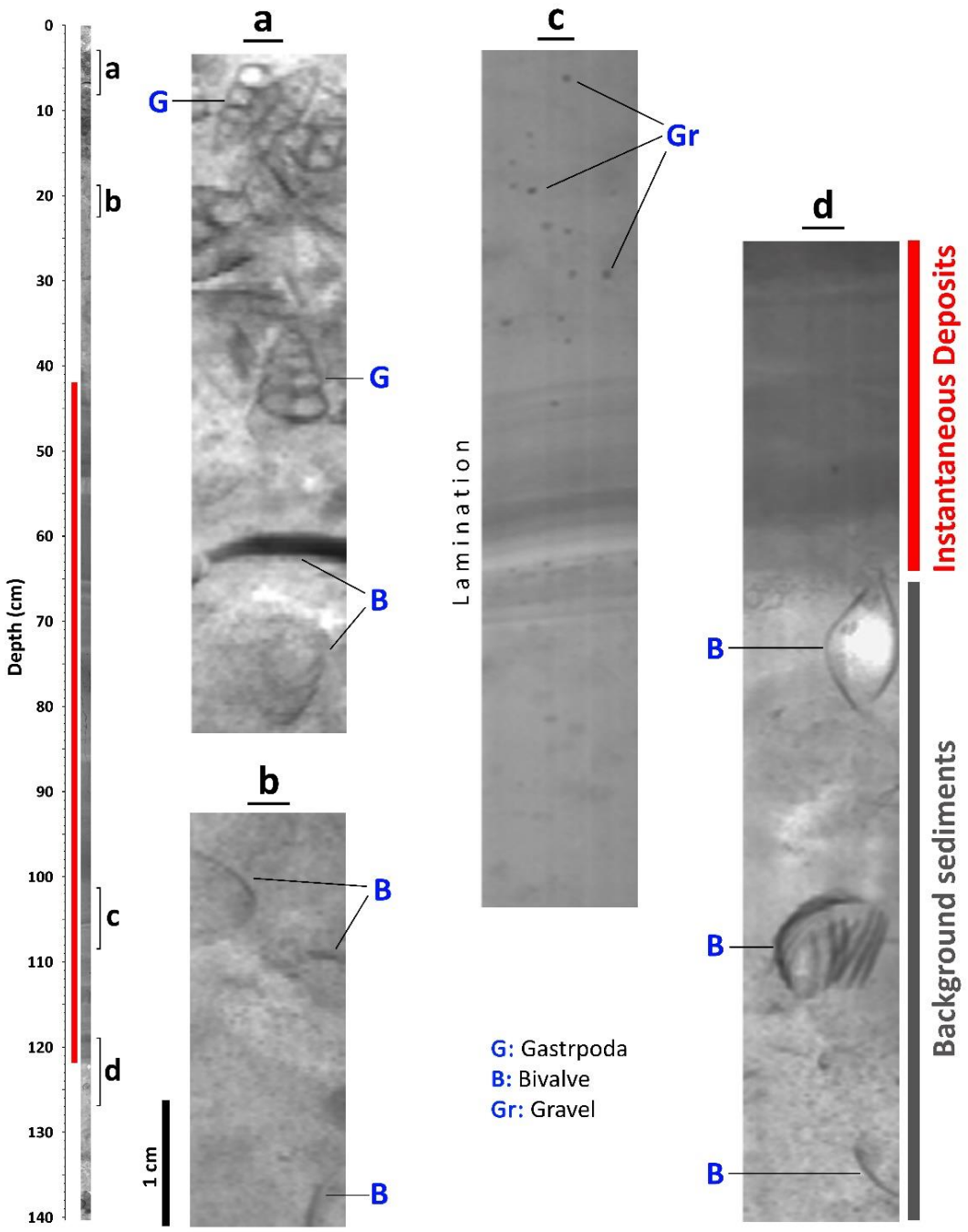

Figure 3.1 Close-up views of DEM-4, as examples of appearances of background and instantaneous deposits.

At the level between 101 cm and 108 cm of the core (Figure 3.1c) gravels (Gr), which are represented by dispersed dark spots, are observed within the homogeneous background. In the middle of part c, lamination of darker and lighter colored sediments is observed. At the section between 119 and 127 cm of the core (Figure 3.1d) the transition between two levels of sedimentation with different characteristics is seen. In the upper part, there is a laminated darker deposit with high homogeneity and high sediment density. Just below this dark-colored part, heterogeneous, lighter-colored levels are observed, with high biological content and mixed sediment distribution. Figure 3.1c and the upper part of Figure 3.1d are examples of rapid deposition along the cores, while the a, b and lower part of the d exemplifies the characterization of background sedimentation. In the radiographic image of DEM-4, sedimentary characteristics are clear and distinguishable. Therefore, images of sample levels selected from the DEM-4 core (Figure 3.1) became the basis for the differentiation of background sediments and instantaneous deposits. Accordingly, along the radiographic images of the other cores, the instantaneous deposits were separated from the background sedimentation and marked with red lines. Sedimentary events identified as instantaneous deposits are dark-colored and homogeneous, indicating significantly denser sediments. It has also been noticed that the events have less biological content than background sedimentation. In addition, somewhat lighter-colored laminations are noticed from time to time in instantaneous deposits. From this point of view, there are five sedimentary events in DEM-4, and DEM-3, three events in DEM-2, and one in DEM-5. In particular, the transition between background sedimentation and instantaneous deposits is more evident at the base of the event, while it is gradual at the upper border. The thickness of the sedimentary events varies from 2 cm (DEM-2) to 80 cm (DEM-4) throughout the lagoon.

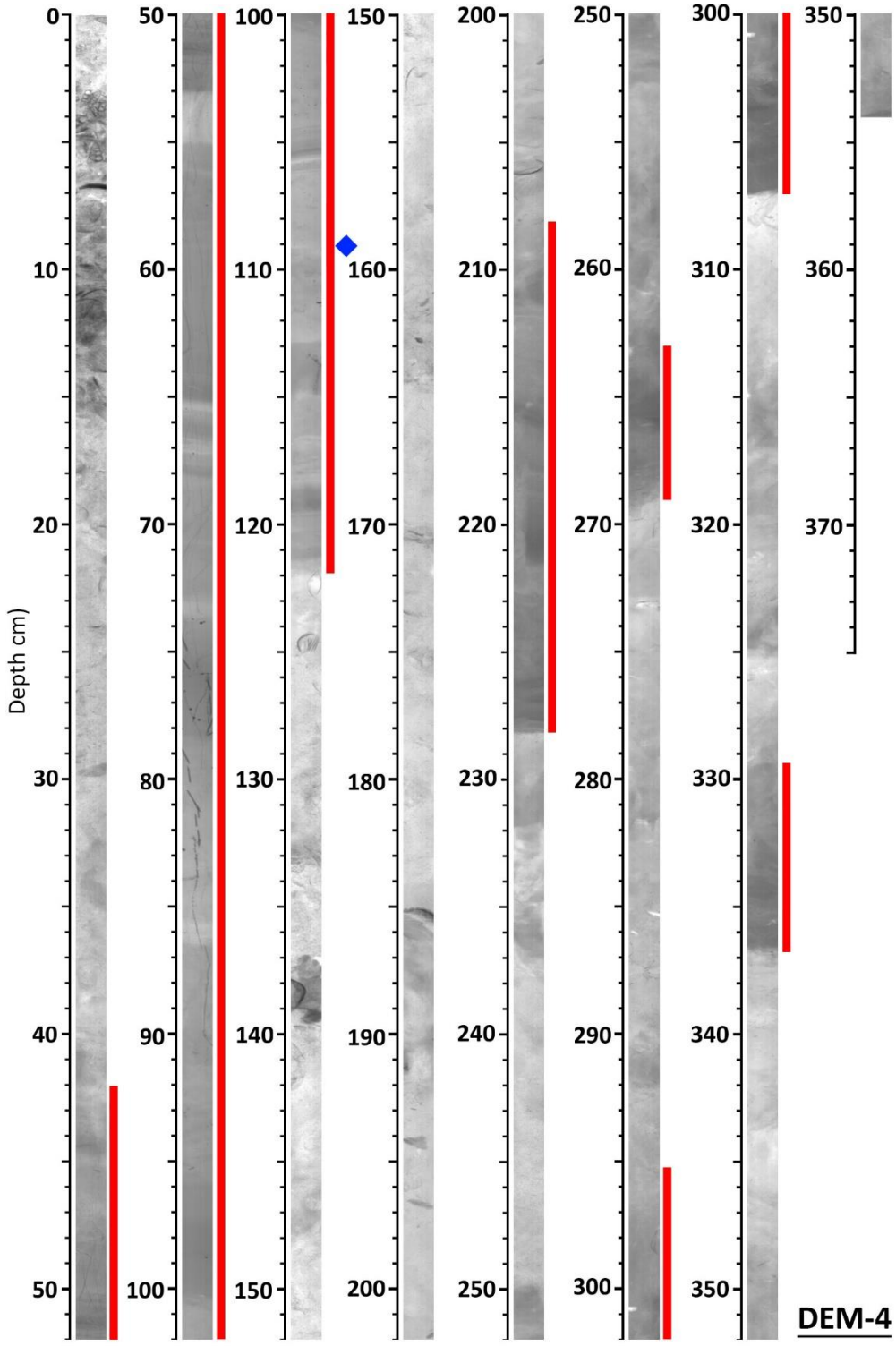

Figure 3.2 Radiographic image along DEM-4. Red lines are instantaneous deposits, and blue diamond stands for the radiocarbon sample.

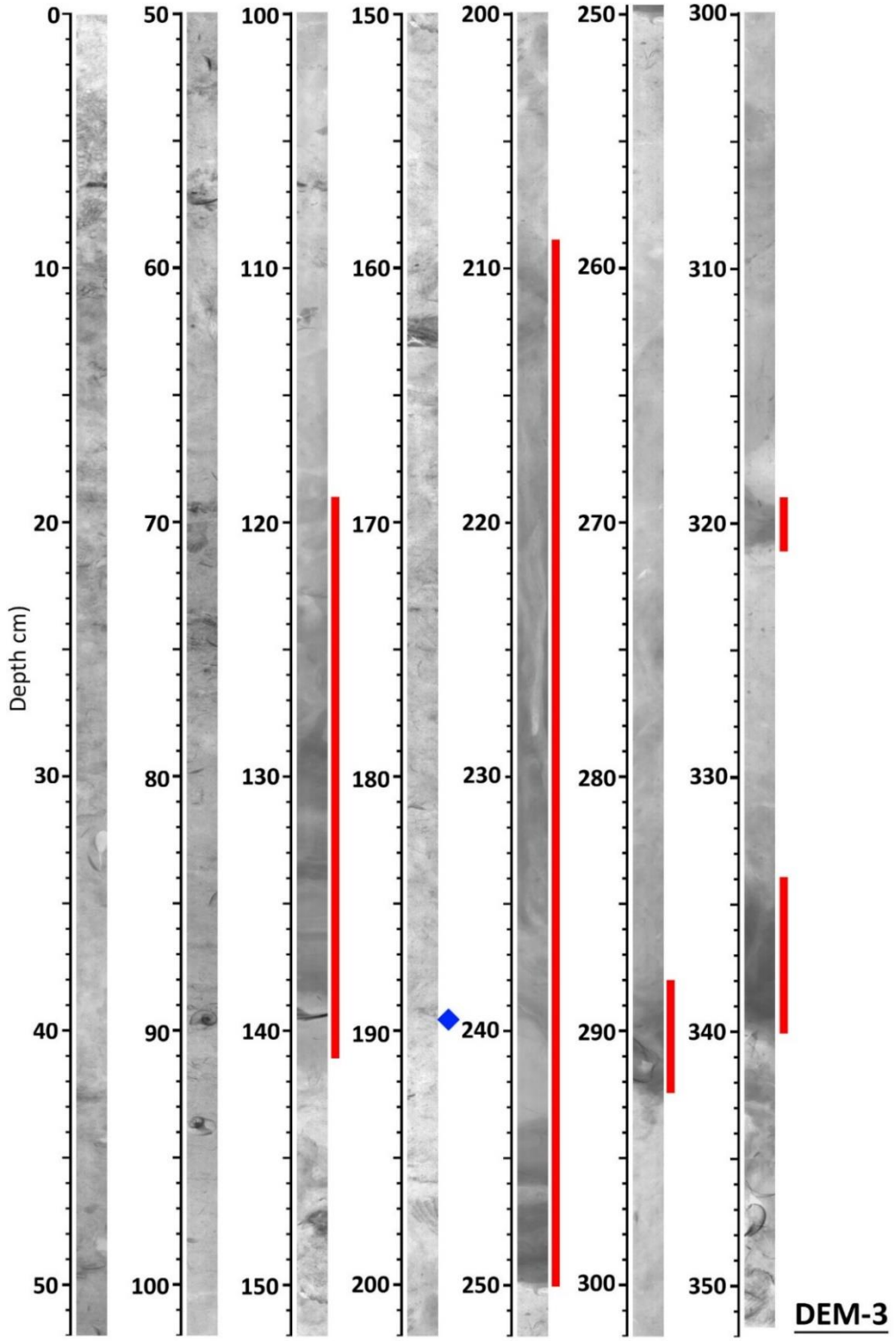

Figure 3.3 Radiographic image along DEM-3. Red lines are instantaneous deposits, and blue diamond stands for the radiocarbon sample.

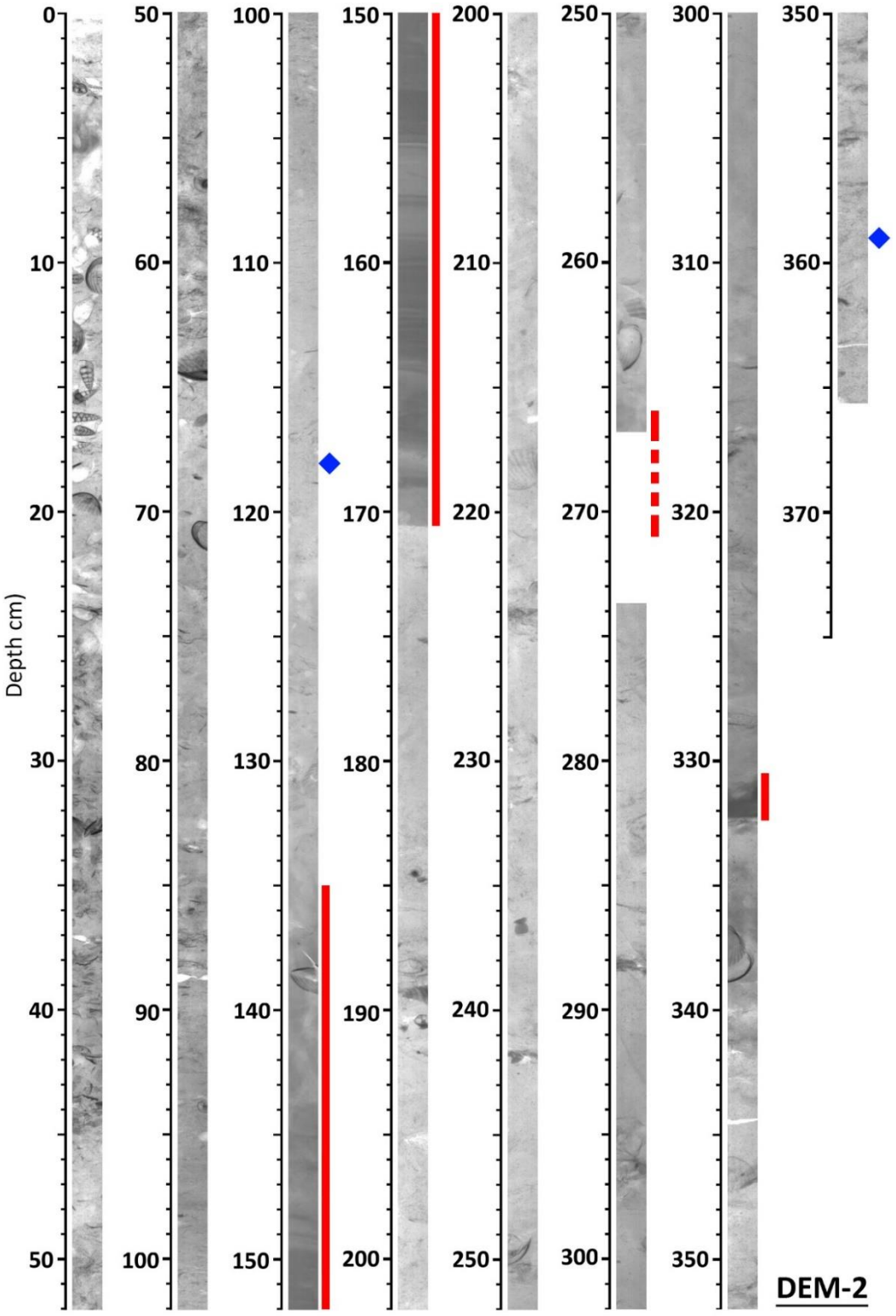

Figure 3.4 Radiographic image along DEM-2. Red lines are instantaneous deposits, and blue diamonds stand for the radiocarbon samples.

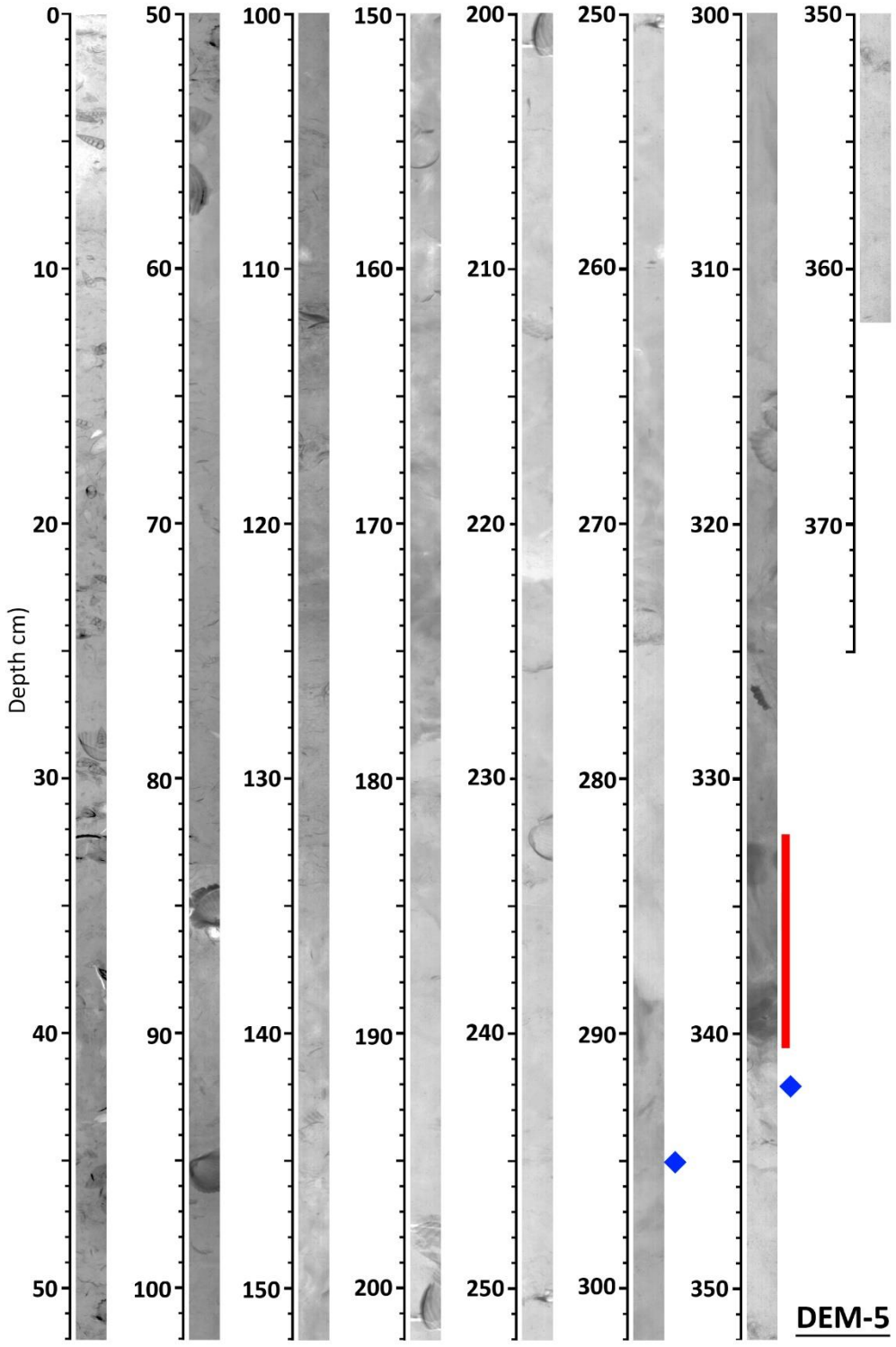

Figure 3.5 Radiographic image along DEM-5. Red lines are instantaneous deposits, and blue diamonds stand for the radiocarbon samples.

The visual variations along the cores detected in radiographic images are plotted as graphs so that they can be presented more clearly and distinctly. To do this, darkness and homogeneity are considered as two main parameters. First, the photos were imported into Matlab, where the images are represented by matrices with a certain grayscale value for each image pixel. In grayscale values, white is represented by 255, and black is defined by 0. Then, this matrix was exported to excel, where the mean and standard deviation of grayscale values for each row of the image matrix was calculated. Afterwards, the heterogeneity index is calculated for each matrix row by multiplying the grayscale mean and the standard deviation values. Lower values indicate more homogeneous levels, while higher values represent heterogeneous levels. The levels that were once determined to be events in radiographic images are marked in figure 3.6 by red. Grayscale (GS) and standard deviation of grayscale (STDEV) values are low in sedimentary event levels, which we considered to be instantaneous deposits. In other words, the graphs indicate lower mean and standard deviation values, for event deposits, which correspond to more homogeneous levels. In addition to the sedimentary event levels, individual sharp decreases in mean grayscale value are noted while analyzing the graphs. However, biological materials, such as bivalve shells, were detected at these levels, which differs from instantaneous deposits.

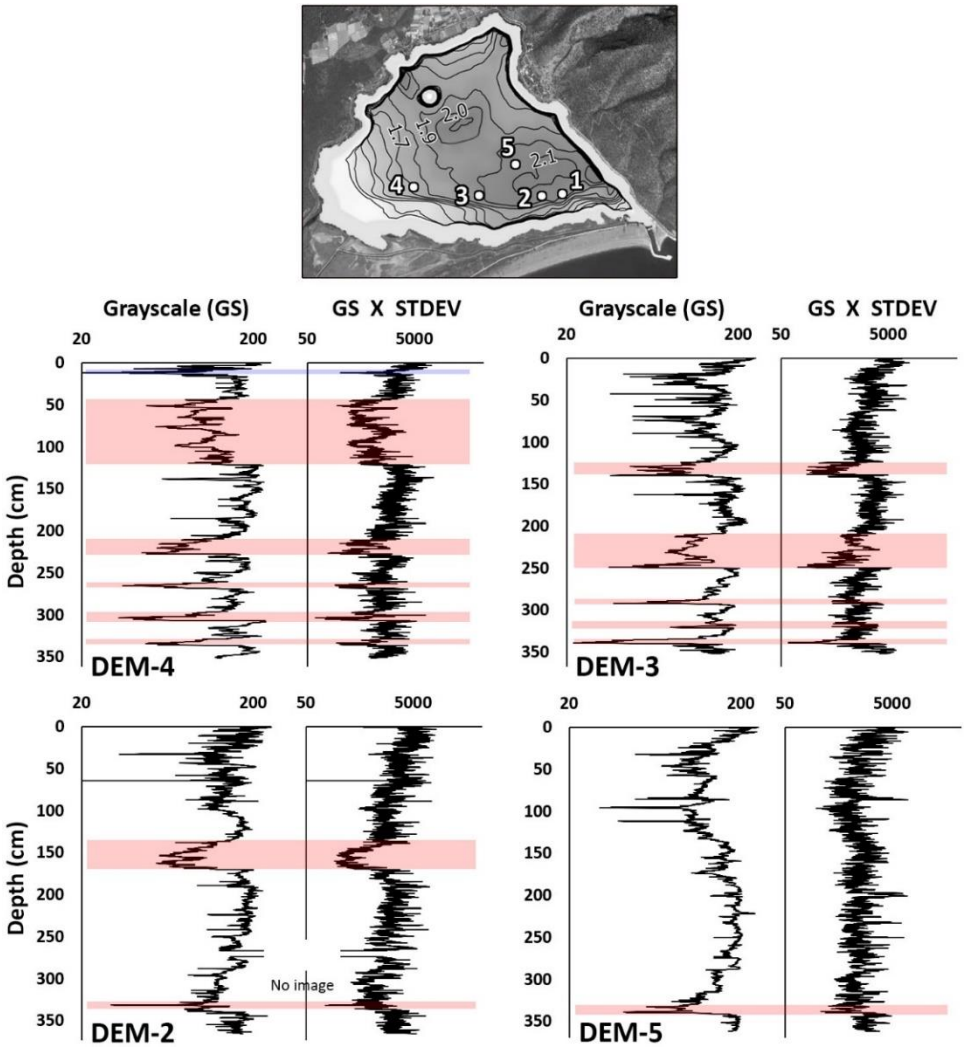

Figure 3.6 Grayscale and heterogeneity index along the cores.

3.2 Micro-XRF Data

In Figure 3.7, XRF data showing the elemental changes along each core is presented. The levels determined as sedimentary events on these graphs are marked with red bars. In DEM-4 and DEM-3, it was observed that Ca and K were enriched while Cl and Br were depleted at sedimentary event levels. Fe, Ti, Si, Rb, and Sr, on the other hand, do not show any significant change along with the event deposits of these two cores. In DEM-2 and DEM-5 cores, while Cl and Br were depleted, Ca, K, Si, and Ti values were enriched at event levels. No significant changes were observed in the

Fe, Rb, and Sr graphs at these levels. As a result, the behaviour of Cl, Br, and Ca were consistent at event levels in all cores, hence these elements were accepted as reliable indicators of tsunami deposits. These unitless elemental values (counts per second) can be affected by water content in the core, organic matter content, and grain size. Therefore, they should not be used as an individual proxy but rather normalized relative to another element. Additionally, it should be emphasized that elemental changes also occur in the rest of the sediments, and thus a single elemental shift should not be considered as an indicator of a paleoseismological event.

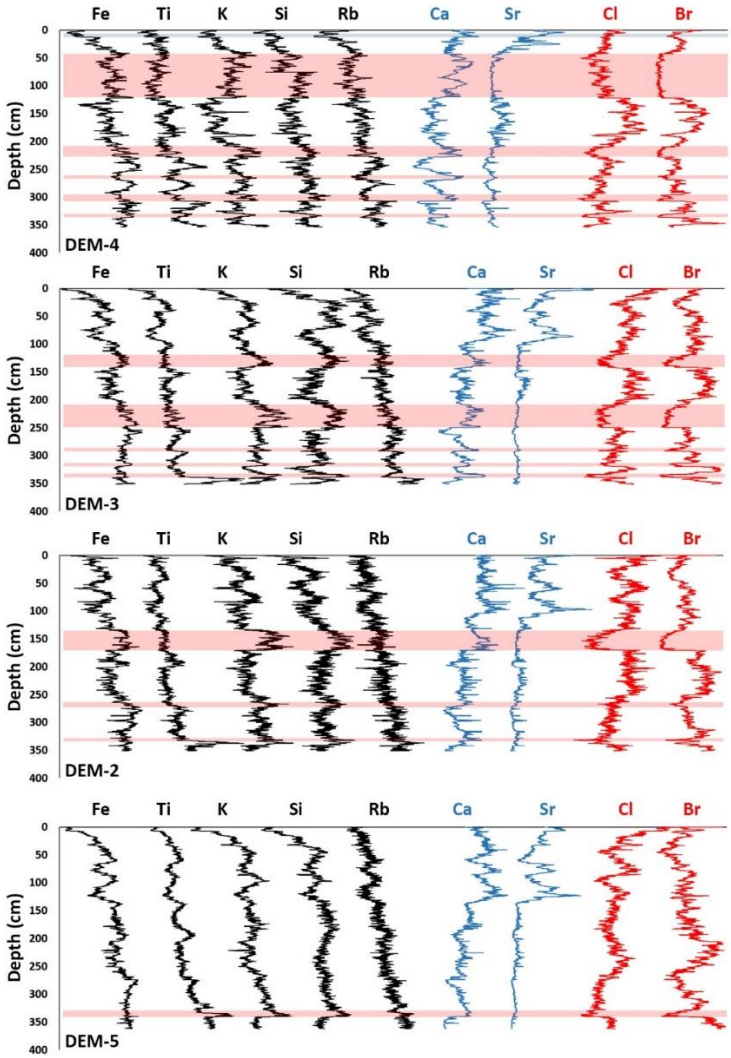

Figure 3.7 XRF data for DEM-2, DEM,3 DEM-4, and DEM-5 showing the variation of each element along with the cores.

3.3 Grain-Size Distribution and Abundance of Foraminifera

The graphs of carbonate-free material >125 μm and the variation of the foraminifera number along the core were obtained for DEM-3, DEM-2, and DEM-5, and the event deposits are marked in red. In general, it was observed that the grain size decreased at the event levels, and the number of foraminifers increased towards the upper parts of the events (Figure 3.8). Small grain size and the low number of foraminifera at event levels in DEM-3 are noticeable. However, in DEM-2 and DEM-5, apart from the event levels there are also levels with significant small grain size and event levels with no significant decrease in grain size.

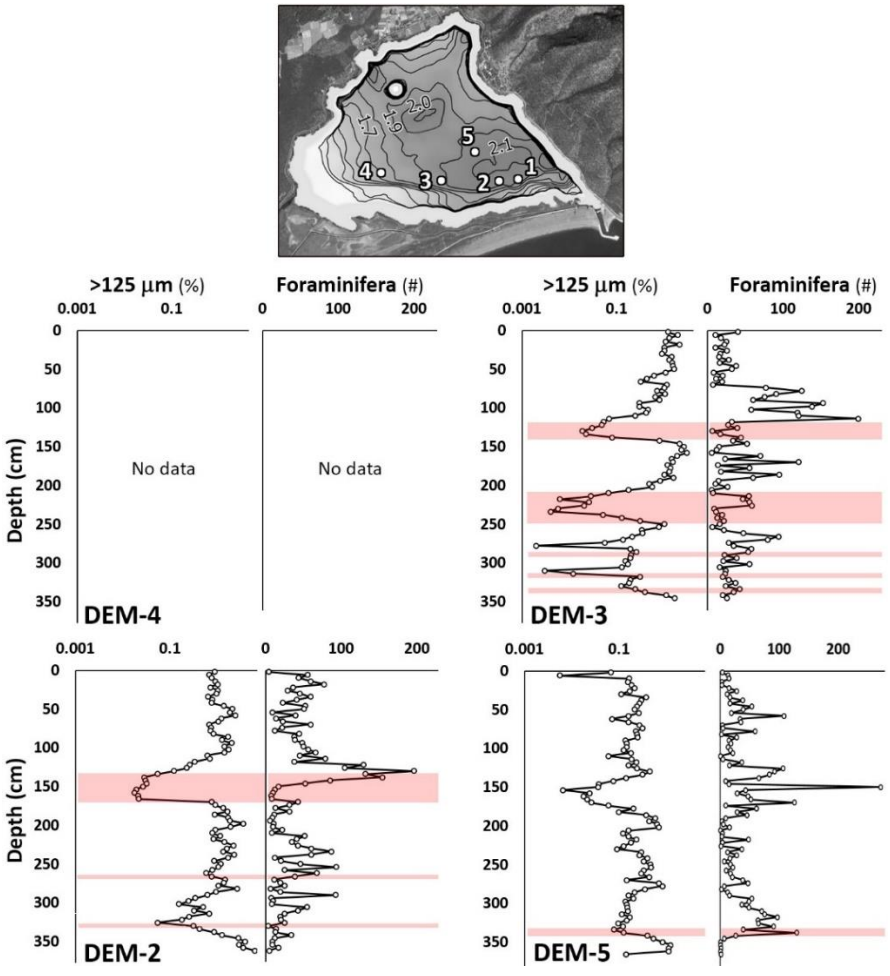

Figure 3.8 Grain-size percentage (>125 microns) and number of foraminifera graphs along with the cores for DEM-4, DEM-3, DEM-2, and DEM-5.

It is generally accepted knowledge that tsunami deposits should be interpreted as following a fining-upward sequence. According to the results, there were no obvious grain-size and foraminifer indications in the minor events in the radiographic images. They demonstrated a distinct observation for events that have higher thicknesses. Due to the sampling resolution of 4 cm, it was not possible to provide precise results for minor events. For this reason, grain size and foraminifer data are used as supporting data rather than as an indicator alone.

3.4 Radiocarbon Data

Radiocarbon dating was performed on the extracted organic materials in order to reveal the sedimentation rate throughout the core and date the tsunami events. For this purpose, while subsampling was carried out along the half core, the appropriate organic materials were separated, and the burned, delicate, terrestrial organic materials of different levels were extracted from all samples for analysis. The findings of the radiocarbon analysis are reported in Table 3.1. Since appropriate material for radiocarbon dating cannot be detected at all levels, the best-suited radiocarbon samples that are chosen, belong to separate cores. Therefore, significant consideration should be given to the correlation of the cores. Taking numerous cores from the lagoon allowed for diversity in selecting radiocarbon samples, resulting in a more precise age-depth model.

Table 3.1 Details of radiocarbon dating samples and the results of the dating.

ID	Core	Depth in Core (cm)	Age (BP)	Calibrated Date (BC/AD)
R1	DEM-4	109	770 ± 30	1252 ± 30 AD
R2	DEM-2	118	1050 ± 30	965 ± 70 AD
R3	DEM-3	190	1200 ± 30	825 ± 120 AD
R4	DEM-5	295	1715 ± 30	332 ± 82 AD
R5	DEM-2	359	7560 ± 40	-6370 ± 105 BC
R6	DEM-5	342	8160 ± 50	-7190 ± 140 BC

Since the amount of ^{14}C in the atmosphere fluctuates over time, laboratory analysis findings must be calibrated before being utilized. In this work, the Oxcal program

was used for calibration, and the Intcal20 version of the calibration curve was employed. Each sample's calibration is shown on a separate graph. The calibration curve is indicated by the blue line in Figure 3.9. The red regions on the y-axis represent the distribution of the laboratory's raw data, whereas the gray areas on the x-axis represent its calibrated projection (Figure 3.9).

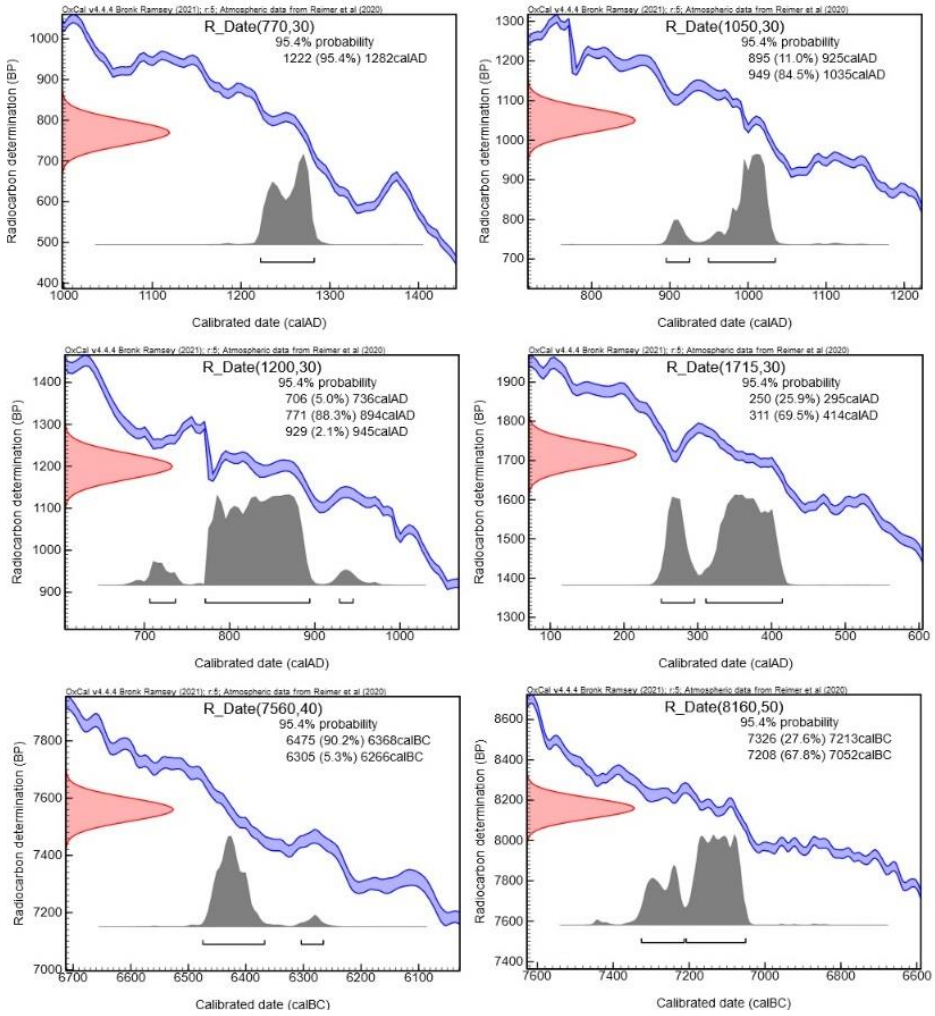

Figure 3.9 The results of radiocarbon calibration performed using the Oxcal software with the Intcal20 calibration curve.

CHAPTER 4

DISCUSSION

In the sediments of the Demre Lagoon, sedimentary events having sedimentary characteristics different from the background sedimentation have been identified. These event deposits may result from earthquakes, storms, floods, or tsunamis. All proxies were analyzed together to identify tsunami event deposits. ITRAX micro-XRF scanning was used to detect elemental changes along the cores in terms of counts per second (cps). However, since ITRAX measurements result in semi-quantitative data (cps), utilizing element ratio profiles rather than single element profiles would result in a more accurate assessment of the relative changes in elements (Avşar, 2019). All elemental variations were normalized by dividing them to Ca to reduce the margin of error. The sediment ratio of Ti/Ca is an extensively used indicator in the literature. Typically, the origin of Ti is a terrestrially derived minerogenic clastic material. Both minerogenic clastic debris from the land and biogenic and chemical carbonates formed in the water column can be the source of Ca. Therefore, the Ti/Ca ratio is regarded as the change of clastic material relative to biogenic and chemical carbonates. The increase in this value can be interpreted as the entry of terrestrial material into the lagoon. In contrast, decreases in the rate can be an indicator of a decrease in terrestrial material or an increase in bio/chemical carbonates. In addition to Ca, organisms with carbonate shells also contain the element Sr. (Croudace and Rothwell, 2015). Therefore, Sr variation is also utilized as an indicator throughout the core by normalizing it with Ca. The Sr/Ca ratio demonstrates the variance between biogenic carbonates and terrestrial carbonates throughout the lagoon. Cl and Br elements showed a consistent decrease in sedimentary events in XRF data. These elements are not primarily found in nature as pure elements, but rather as salts that have interacted with metals. Therefore,

Cl/Ca and Br/Ca graphs were utilized as an indicator of the variation of chemical salts precipitating naturally in the lagoon.

In addition to the Ca-normalized XRF data for each core, the grain size percentage graph, the number of foraminifera graph, and the standard deviation graph were also interpreted together. The characterization of these levels was first done using the DEM-4 because the sedimentary events are more prominent in the radiographic image of this core compared to the other cores. At these levels, it was found that the standard deviation is lower, the percentage of clastic material coarser than 125 microns is lower, and foraminifera content increases close to the top of the sedimentary events (Figure 4.1). In addition, Ti/Ca, Sr/Ca, Cl/Ca, and Br/Ca ratios are much lower in the event deposits compared to the background sediments. All of the potential tsunami events are highlighted as red bars with the help of the integrated data (Figure 4.1).

The sedimentary event levels determined by radiographic images are indicated in Figure 3.7. Accordingly, six distinct sedimentary event levels were detected in DEM-4. After combining all of the data, three more events were detected between 125 and 200 cm (Figure 4.1). These added levels are not detectable on the radiographic image of DEM-4. Although there were no apparent decline in the HI index for these events, each chemical indicator show consistent drop. The tsunami level may not be visually observed where the tsunami cannot carry enough sediment. Therefore geochemical proxies may play an important role in these cases. These three levels that were added with integrated data are typical examples of this. Although there is a significant decrease in Br/Ca and Cl/Ca around 135 cm, it is not classified as a potential tsunami event. Since Ti/Ca ratio increases at this level, which indicates increase in terrestrial minerogenic material, this event is most likely a flood.

Using radiographic images, five sedimentary occurrences were identified in DEM-3 (Figure 3.7). After analyzing the integrated data, an event was added that shows a consistent trend in the indicators assessed at a depth of around 25 cm. Similarly, values for HI, Ti/Ca, Sr/Ca, Cl/Ca, and Br/Ca decreased at this level. Even if the

grain size percentage of event deposits is lower compared to background sedimentation, it is not observed at this level because the event is so thin. In other words, despite the millimeter resolution of ITRAX micro-XRF core scanning, grain size analysis was done at 4-centimeter intervals; therefore, grain size and foraminifer data alone may be deceptive in tiny event deposits. At 97 cm, HI, Ti/Ca, Cl/Ca, Br/Ca, and grain size percentage followed a similar trend as events, however, Sr/Ca data followed an entirely different trend and was enriched. This level was not considered an event deposit because it was completely atypical of tsunami event deposits. The rise in Sr/Ca data can be correlated with an increase in biogenic marine carbonate in the water, which can be attributed to a shift in climatic conditions.

Even though three events were observed visually in radiographic images of DEM-2, the integrated data at a depth of 300 cm suggested the possibility of a very thin event deposit. DEM-5 is the innermost core among the cores. Therefore, almost no distinct event records were seen in its radiographic images. A homogeneous dark level was noticed at just 345 cm. When the tsunami waves reached this location, the majority of the sediments had likely accumulated in the outermost parts of the lagoon. As a result, the event deposit could not be determined from visual inspection. At 260 and 153 cm depths, two more subtle potential event deposits are identified when all available data is included. All three event deposits in DEM-5 are thin. It indicates that relatively limited sediment was transported to this point.

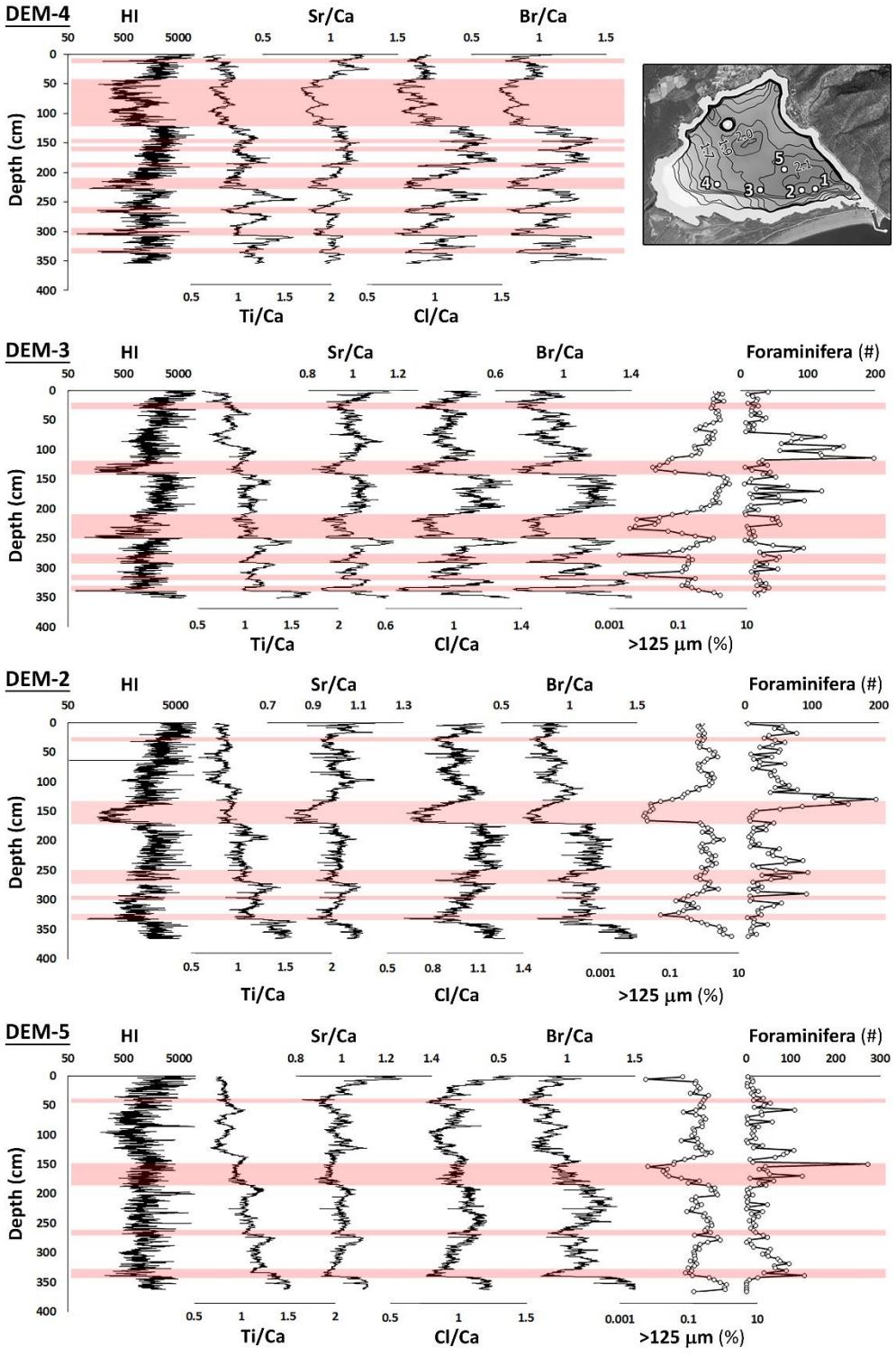

Figure 4.1 Integrated data which include heterogeneity index, Ca-normalized XRF data (Ti, Sr, Cl, Br), grain-size (%), and foraminifera number for DEM-4, DEM-3, DEM-2 and DEM-5.

After identifying events at each core based on integrated data, a stratigraphic correlation should be made to assess the extent of events in the lagoon. In this study, stratigraphic correlation was done based on Cl/Ca profiles of the cores (Figure 4.2). Events have been extracted from these graphs, and correlation has been made according to background sedimentation. Most of the nine events seen in DEM-4 diminish towards DEM-5, the inner part of the lagoon. Due to geochemical anomalies that are not evident in radiographic images, event 1 (E1) is identified as a potential event. In the case of a potential tsunami, however, it is typically assumed that the thickness of the event deposit will decrease toward the interior parts, although this has not been observed here. E2 is 80 cm thick and is the most notable tsunami record in the lagoon, which reaches the inner part of the lagoon (DEM-5). The subsequent events 3, 4, and 5 have limited impact and are not immediately apparent except for EM-4. Event 6 is the second most notable occurrence in the lagoon. E7-E8 and E9 are events that are observable in other cores, but their impact is diminished in DEM-5.

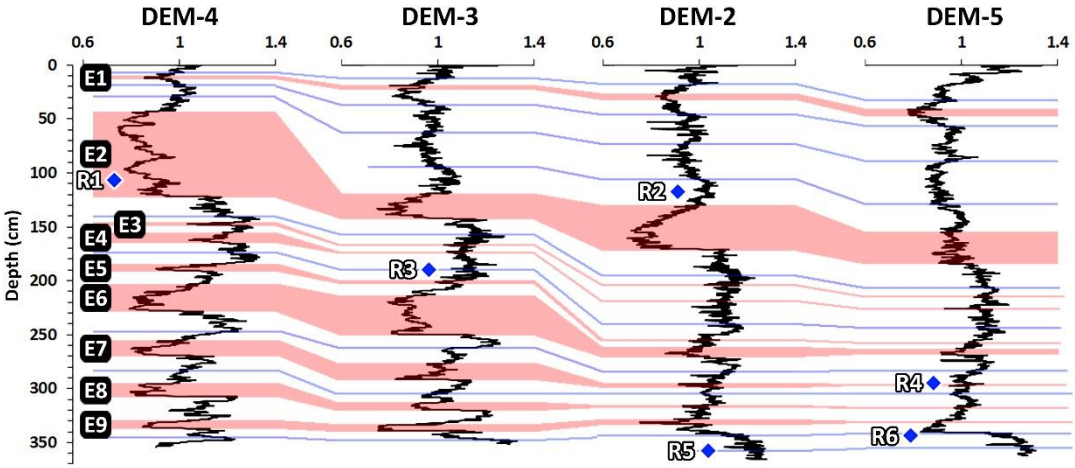

Figure 4.2 Stratigraphic correlation of the cores based on Cl/Ca profiles. The red areas show the events (E1 to E9). The blue diamonds (R1 to R6) indicate the radiocarbon dating levels.

DEM-2 provides the most extended stratigraphic record. Because of this, the age-depth model was established over DEM-2. Based on the correlation, the DEM-2 levels at which all events and the measured radiocarbon levels in other cores correspond were determined. Since event deposits are instantaneous depositions, they are deposited in a short period and are thus excluded from the sequence when developing the age-depth model. After removing sedimentary event deposits, a composite sequence was formed. The ages obtained from the radiocarbon analysis and the corresponding levels on the DEM-2 are plotted. R2, R5, and R6 are reworked samples and are very scattered and inconsistent on the graph. A parabolic best fit was created over the three radiocarbons (R1, R3, and R4) that gave consistent results and the 0 cm point corresponding to the date of cores taken in 2017 (Figure 4.3). When all nine events were reflected on the age-depth model, the approximate ages of all events were determined and shown on the graph.

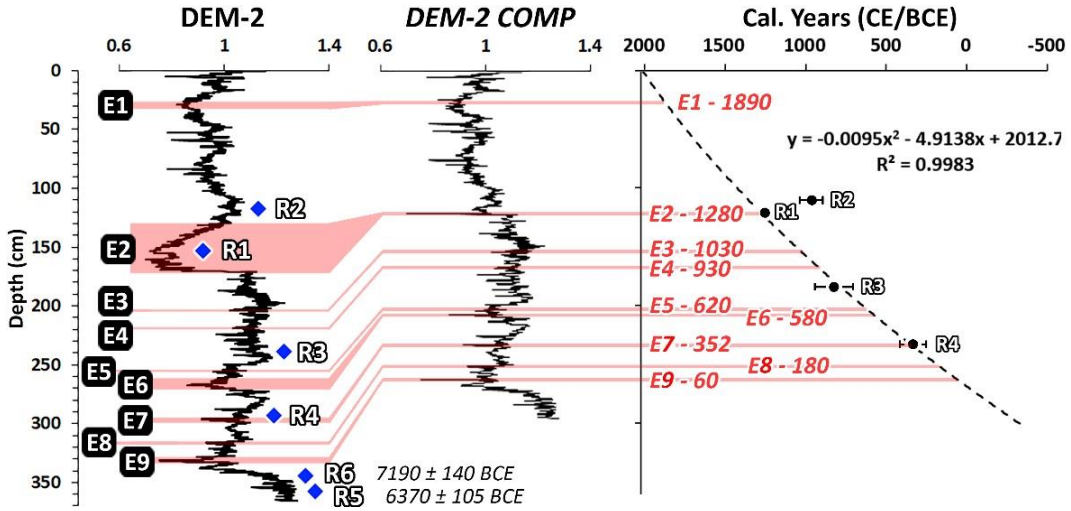

Figure 4.3 Age-depth model constructed on DEM-2 according to the radiocarbon data (Blue diamonds, R1-R6). Levels highlighted in red are event deposits (E1 to E9).

Figure 4.4 illustrates the sites of tsunamis with geological evidence and historical records in the Eastern Mediterranean region. The corresponding ages of these past

tsunamis are schematized in Figure 4.4 b. Levels marked with yellow dots are tsunami records identified in previous studies. Black marks are tsunamis documented in historical records. The red rectangles are the possible tsunami events detected in this study. According to age-depth (Fig 4.3), the youngest event, E1, corresponds to 1890 CE. On June 24, 1870, an earthquake of magnitude 7.5 occurred in the Eastern Mediterranean, triggering a tsunami. In Kefr Saber and Marsa-Matrouh, traces of this Tsunami were identified (Shah-Hosseini et al., 2016; Salama et al., 2018). Considering the error margin of radiocarbon analyses, E1 may be associated with the Tsunami of 1870. A similar historical record was seen on the shores of Samandag as the 1872 tsunami (Salamon et al., 2017). On the coasts of Samandag, a similar historical record has been found as the 1872 tsunami (Salamon et al., 2017). On the other hand, if a tsunami of this magnitude occurred so recently, it would be predicted to be more prominently reported in historical documents.

According to historical sources, two earthquakes at the northeast of Pliny Trench in the Eastern Mediterranean triggered tsunamis in 1609 and 1741 (Papadopoulos et al., 2014). In addition, the records of these two tsunamis have been found in Ölüdeniz, a lagoon located near Demre Lagoon (Avşar 2019a, Yeniçeri 2020). However, no event deposits have been detected in the Demre Lagoon between the 19th and 13th centuries.

According to geochemical, physical, sedimentological, physical, and foraminiferal analyses, E2 is the most prominent event throughout all cores in this study. Based on the developed age-depth model, its age corresponds to 1280. In 1303, a tsunami-generating earthquake happened the eastern portion of Crete. In the examined lagoons of Kefr Saber and El Alamein, traces of the 1303 tsunami were also detected (Salama et al., 2018). In addition, this tsunami has been recorded in Dalaman and Ölüdeniz (Alpar et al., 2012; Papadopoulos et al., 2012). In particular, two studies done in Ölüdeniz discovered distinct geochemical proxies (Avşar, 2019a; Yeniceri, 2020). Even in the Karine lagoon, which is situated inland of the Aegean Sea, evidence of the tsunami that occurred in 1303 has been found. Therefore considering

that this tsunami had an observable effect in the eastern Mediterranean, it is quite likely that the E2 event at Demre Lagoon is connected to this large 1303 tsunami.

Event 3 (E3) is a minor deposit that only reveals geochemical traces in the DEM-4 core. It is also one of the lagoon's least traceable events. Probably, it did not reach other core locations, nor could not transport a significant amount of allochthonous material in DEM-4. According to the age-depth model, its age corresponds to 1030. According to historical sources, near Tel Aviv (Ashkelon and Caesarea), tsunamis happened in 1068 and 1033 (Salamon et al.,2007). Although E3 does not have a significant trace in the lagoon, it can be said that this possible tsunami event is related to the historical Tsunami of 1033 or 1068.

Event 4 (E4) is minor detected in the lagoon-like as E3. Only DEM-4 contains signs of its occurrence. The age-depth model indicates that this event occurred around 930. (Fig. 4.3). However, no historical tsunami events are known to have taken place during this era, and no geological remnants have been discovered in earlier research. It is possible to claim that a tiny tsunami affected a small region.

It has been discovered that the measured values for events 5 (E5) and 6 (E6) are chronologically proximate. The age-depth model indicates that E5 corresponds to 620 years and E6 corresponds to 580 years. E5 is a thin event deposit that is not evident in DEM-2 or DEM-5. According to historical sources, there was a tsunami in 551 near Beirut (Salamon et al., 2007). Considering the error margin in the data, it is logical to argue that E6 is associated with the 551 tsunami. In addition, the fact that the geological record of the tsunami of 551 was not observed in any of the stated earlier research emphasizes the significance of this finding.

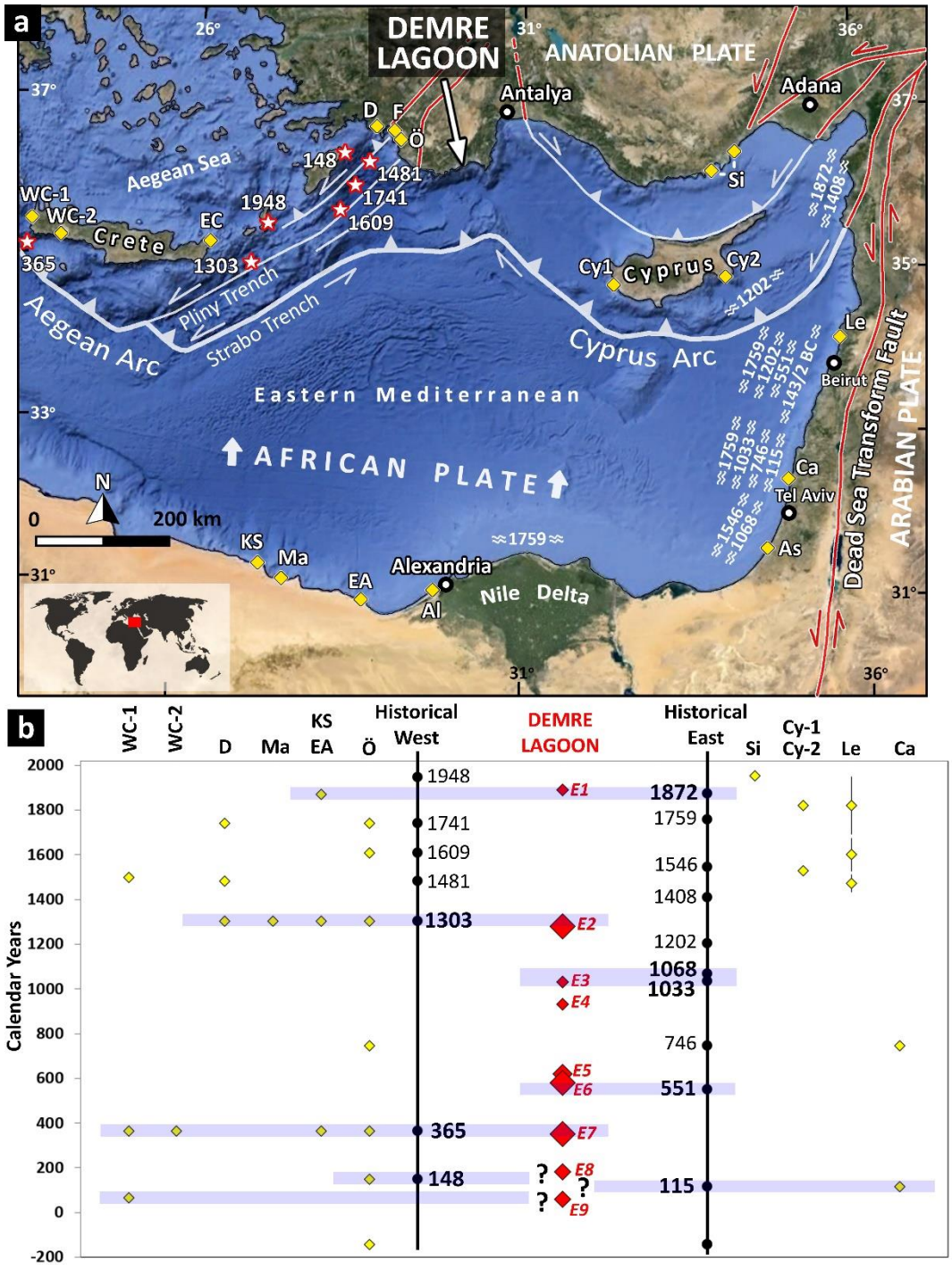

Figure 4.4 Schematic summary of past tsunamis in the eastern Mediterranean. The black dots are historical tsunamis. The yellow diamonds are geological records of past tsunamis available in the literature. The red diamonds are the events detected in this study.

Event 7 (E7) is significant in three cores except for DEM-5. The age-depth model indicates that it relates to the year 352. It is known that a tsunamigenic earthquake occurred in the west of Crete in 365, and the traces of this tsunami were primarily recorded in Crete, as well as in the north of Egypt and Ölüdeniz (Pirrazzoli et al., 1992; Scheffers and Scheffers 2007; Wernet et al., 2018; Shah- Hosseini et al., 2016; Salama et al., 2018; Avşar, 2019a). Since the date of this tsunami, of which traces are widespread in the region, and the age we determined are extremely near, it is feasible to infer that the E7 belongs to the traces of 365 tsunamis.

Events 8 and 9 (E8 and E9) did not obviously approach DEM-5. The age-depth model indicates that E8 corresponds to 180 years and E9 to 60 years. In 148, a tsunamigenic earthquake is reported to have occurred in the Aegean Sea (Papadopoulos et al., 2014). Additionally, its geological remnants have been found in Ölüdeniz (Yeniceri, 2020). On the other hand, historical sources indicate a tsunami near Tel Aviv in 115, and its geological remnants were identified in the same region. (Salamon et al., 2007; Goodman-Tchernov et al., 2009; Tyuleneva et al., 2018). E8 is likely related to one of the 148 or 155 tsunami occurrences. In addition, at the west of Crete, a tsunami record from the 1st century was discovered. Although E9 is probably connected to this, it is impossible to establish a definitive connection because there are no clear incident regions. In light of these observations, the instantaneous sedimentary event deposits we discovered in the Demre lagoon demonstrate temporal consistency with past tsunamis. Therefore, it is reasonable to claim that these events are tsunami deposits and the Demre lagoon has geological evidence of previous tsunami records.

Under normal conditions, 3 main materials are deposited in the lagoon and the sea. These materials are detrital, geochemical, and biological. Siliciclastics and carbonates enter both the sea and the lagoon from the land, and these contain the elements Ti, Fe, K, Si, Rb, and Ca. Sr can be found together with Ca in the structure of crustaceans, it is also associated with salts because it can combine with the hydroxyl group (-OH) to form a salt (Ropp, 2013). Cl and Br are included in the halogen group in the periodic table and are among the elements with the highest potential to react with metals and produce salts (House and House, 2016). Therefore, the variations in Cl, Br, and Sr in the environment are attributed to salts. As the

tsunami wave enters the lagoon from the sea, it suspends sediment from the near shore and sand barrier and disperses it into the lagoon. Meanwhile, it transports a tiny quantity of siliciclastic material from the sandspit and sea.

Unfortunately, there is no hydrochemical data on the Demre lagoon. However, it is known that there is no stream inflow into the lagoon. In addition, because the water depth does not exceed 2 meters and it is a lagoon with a size of around 1.5 km x 2.0 km, the evaporation rate can be expected to be high, and the lagoon is hypersaline compared to the sea. In other words, we estimate that the background sedimentation in the Demre lagoon consists of higher salt than in the sea under normal conditions. During the tsunami, there is a sudden inflow of water and material into the lagoon, and rapid deposition happens. There is insufficient time for the salt to precipitate from the water column during this deposition, and Cl, Br, and Sr are depleted from tsunami deposits. In addition, the biological organisms inhabiting the lagoon require a specific amount of time to finish their life cycles and precipitate. However, since there is instantaneous deposition during the tsunami, a life period cannot fit it, and biological creatures living in the lagoon environment are not observed in these deposits. Ca have both terrestrial and marine origins, whereas Ti and Fe are minerogenic elements of terrestrial origin. Because of this, it is assumed that terrestrial material will have a greater Ti/Ca ratio than marine material. For instance, we would expect a high Ti/Ca ratio if these events were instantaneous deposits caused by floods rather than tsunamis. Due to the low Ti/Ca ratio identified in the events of this study, these deposits can be attributed to marine-derived material.

Despite the common expectation that the grain size in these deposits is increased because of the high energy of tsunami waves, this study discovered finer grain sizes in tsunami deposits. The lowest part of the sand barrier is about 200 meters and extends up to 1 km. According to the findings of this study, once the tsunami wave crossed the barrier and mixed with the lagoon water, its energy was substantially diminished, and coarse-grained sediments were deposited at the entry to the lagoon. Suspendable fine-grained sediment can reach core locations and form tsunami deposits.

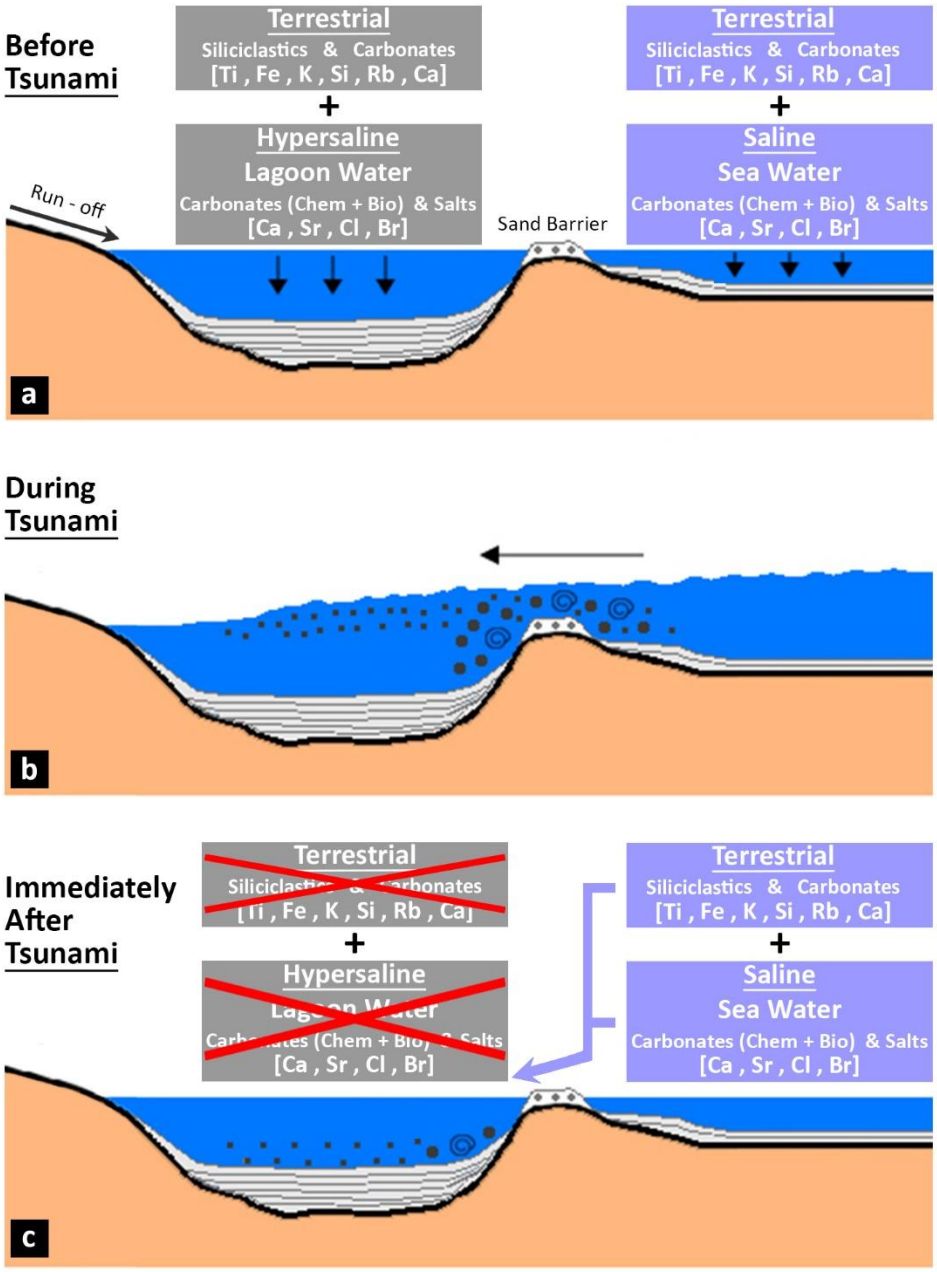

Figure 4.5 Possible mechanism explaining the characterization of tsunami deposits in Demre Lagoon.

The instantaneous event deposits in Demre Lagoon might be related to earthquakes, storms, floods, or tsunamis. If the events identified were deposits from floods, we would expect to observe Ti/Ca peaks because floods would bring significant amounts of terrestrial siliciclastics to the lagoon that would result in Ti-enriched deposits. On

the contrary, the events in Demre Lagoon have lower Ti/Ca ratios, which rules out floods to be the source of these events. Similarly, the events detected in this study are not expected to be earthquake-induced increases in the erosion rates in the catchment of Demre Lagoon. If the events were earthquake-induced, they would consist of terrestrial sediments from the catchment, and the Ti/Ca ratio would be higher. However, this is not the case for the event deposits in Demre Lagoon; they have lower Ti/Ca ratios. Hence, floods and earthquakes are not likely to be the source of the events detected in Demre sedimentary sequence.

Extreme wave occurrences can also be caused by storms (EWE). Vött et al. (2018) indicate that between 73 and 98 percent of all EWEs in the Mediterranean Sea between 1902 and 2017 were tsunamis. According to these statistics, it is reasonable to conclude that the probability of storm surges in the Mediterranean producing geological traces comparable to those created by tsunamis is extremely low (Avşar, 2019a). Therefore, it can be claimed that the sedimentary events detected in Demre Lagoon are most probably not related to storms. Considering that; (i) earthquakes, floods and storms are not likely the sources of the events in Demre, and (ii) the events temporally correlate with the historical tsunamis in the Eastern Mediterranean, one can confidently claim that nine sedimentary events detected in Demre Lagoon (E1 to E9) are tsunami deposits.

Thicknesses and extents of tsunami deposits in the lagoon is controlled by several parameters and conditions during tsunamis. Obviously, tsunamis having higher intensities can be expected to transport more material into the lagoon and leave thicker tsunami deposits. However, wave direction and morphology of the sand barrier at the time of tsunami would also significantly determine how much sediment would be transported into the lagoon. Unfortunately, we do not have any information on wave directivity and its possible consequences in terms of sedimentation for Demre Lagoon. Morphology, geometry and location of sand barriers of this kind of lagoons can quickly be modified in their history, even in several decades. For example, deposits of a tsunami when the sand barrier is low, narrow and close to the coring location would be much thicker than the deposits of another tsunami having

the same intensity but at a time when the sand barrier is high, wide and far from the coring location. In addition to the uncertainties regarding the tsunami directivity and morphological changes of the sand barrier through time, we also do not know what kind of turbulence and hydrodynamic conditions are induced during sea water inundation into the lagoon. Turbulence in the lagoon during inundation may easily result in sediment focusing, where we could observe highly different thicknesses for the same tsunami. Considering these uncertainties, discussions and efforts on linking the thicknesses of tsunami deposits in Demre cores to the intensity of tsunamis are deliberatively avoided in this study.

CHAPTER 5

CONCLUSION

From this study, the following findings could be drawn:

- Along 4 undisturbed sediment cores, nine instantaneously deposited sedimentary events were identified in Demre Lagoon.
- These deposits are characterized by more homogeneous, denser, and finer-grained sediments and have low elemental ratios of Ti/Ca, Sr/Ca, Cl/Ca, and Br/Ca compared to the background sedimentation.
- Since the lagoon has hypersaline water, bio/chemical carbonate and detrital siliciclastic deposition in the lagoon is also accompanied by salt deposition, which is the main source of Cl and Br in the sediments. Since there is no time for salt deposition during the sudden deposition of tsunami deposits, they are depleted in Cl, Br, and Sr. In addition, Ti/Ca ratio in tsunami deposits is lower due to instantaneous influx of marine sediments into the lagoon.
- According to the age-depth model based on the six radiocarbon dates (three of which were reworked), these instantaneous deposits temporally correlate with historically reported tsunamis in the Eastern Mediterranean.
- Events from the youngest to the oldest (E1 to E9), the age determination is as follows; E1 corresponds to late 19^{th} century and is associated to the tsunami of 1870. E2 corresponds to the end of the 13^{th} century and is associated to the 1303 tsunami. E3 occurred in the 11^{th} century and is probably due to one of the 1033 or 1068 tsunamis. E4 and E5 correspond to the 10^{th} and 7^{th} centuries, respectively, but no historical or geological records are known around these years. E6 corresponds to the middle of the 6^{th} century and is associated to the 551 tsunami. E7 marks the middle of the 4^{th} century and is associated with the traces of the 365 tsunamis. E8 and E9 correspond

to the 2nd and 1st centuries, respectively. E8 can be associated to either 148 tsunami in the west or 115 tsunami in the east. There is no known historical tsunami for E9 in the 1st century.

- This study was conducted using cores with a maximum length of 3,7 meters, which covers the last ca. 2000 years. Further research with longer cores would considerably contribute to the efforts to reveal recurrence behavoir of tsunamis in the Eastern Mediterranean.

REFERENCES

Altinok, Y., Tinti, S., Alpar, B., Yalçiner, A. C., Ersoy, Ş., Bortolucci, E., & Armigliato, A. (2001). The Tsunami of August 17, 1999 in Izmit Bay, Turkey. Natural Hazards, 24(2), 133–146. https://doi.org/10.1023/a:1011863610289

Antonopoulos, J. (1992). The great minoan eruption of Thera volcano and the ensuing tsunami in the Greek Archipelago. Natural Hazards, 5(2), 153–168. https://doi.org/10.1007/bf00127003

Avşar, U. (2013). Lacustrine paleoseismic records from the North Anatolian Fault, Turkey (Doctoral dissertation, Ghent University).

Avşar, U. (2019a). Sedimentary geochemical evidence of historical tsunamis in the eastern Mediterranean from ölüdeniz lagoon, SW turkey. Journal of Paleolimnology, 61(3), 373–385. https://doi.org/10.1007/s10933-018-00065-x

Avşar, U. (2019b). Ege denizi'Nde Son 1500 Yılda Meydana gelmiş Tsunamilerin Karine lagünü'ndeki Sedimanter izleri. Türkiye Jeoloji Bülteni / Geological Bulletin of Turkey, 1–1. https://doi.org/10.25288/tjb.545990

Ben-Menahem A. 1979. Earthquake catalogue for the Middle East (92 B.C. –1800 A.D.). Boll. Geofis. Teor. Appl. 21:245–310

Biryol, C.B., Beck, S.L., Zandt, G., ¨Ozacar, A.A., 2011. Segmented African lithosphere beneath the Anatolian region inferred from teleseismic P-wave tomography. Geophys. J. Int. 184 (3), 1037–1057.

Björck, S., & Wohlfarth, B. (2002). 14C chronostratigraphic techniques in paleolimnology. In Tracking environmental change using lake sediments (pp. 205-245). Springer, Dordrecht.

Böning P, Bard E, Rose J (2007) Toward direct, micron-scale XRF elemental maps and quantitative profiles of wet marine sediments. Geochem Geo- phys Geosyst 8:Q05004. https ://doi.org/10.1029/2006GC001480

Bronk Ramsey, C. (2017). Oxcal Program V. 4.3.2". University of Oxford, Radiocarbon Accelerator Unit.

Bruins, H., MacGillivray, J.A., Synolakis, C., Benjamini, C., Hanan, J.K., Kisch, J., Klügel, A., and van der Plicht, J., 2008, Geoarchaeological tsunami deposits at Palaikastro (Crete) and the Late Minoan IA eruption of Santorini: Journal of Archaeological Science, v. 35, p. 191–212, doi: 10.1016/j.jas.2007.08.017

Chagué-Goff, C., Szczuciński, W., & Shinozaki, T. (2017). Applications of geochemistry in tsunami research: A Review. Earth-Science Reviews, 165, 203–244. https://doi.org/10.1016/j.earscirev.2016.12.003

Chawchai S, Kylander ME, Chabangborn A, Löwemark L, Wohlfarth B (2016) Testing commonly used X-ray fluorescence core scanning-based proxies for organic-rich lake sediments and peat. Boreas 45:180–189

Chlieh, M., Avouac, J.-P., Hjorleifsdottir, V., Song, T.-R. A., Ji, C., Sieh, K., Sladen, A., Hebert, H., Prawirodirdjo, L., Bock, Y., & Galetzka, J. (2007). Coseismic slip and Afterslip of the great MW 9.15 Sumatra-andaman earthquake of 2004. Bulletin of the Seismological Society of America, 97(1A), 152–173. https://doi.org/10.1785/0120050631

Cundy, A.B., et al., 2000. Coastal wetlands as recorders of earthquake subsidence in the Aegean: a case study of the 1894 Gulf of Atalanti earthquakes, central Greece. Marine Geology 170 (1–2), 3–26.

Croudace, I. W., and Rothwell, R. G. (Eds.). (2015). Micro-XRF studies of sediment cores: Applications of a non-destructive tool for the environmental sciences (Vol. 17). Dordrecht, Netherlands: Springer.

Croudace, I.W. ve Rothwell, R.G., 2015. Twenty Years of XRF Core Scanning Marine Sediments: What Do Geochemical Proxies Tell Us?, I.W. Croudace ve R.G. Rothwell (Eds.). Micro-XRF Studies of Sediment Cores, Developments in Paleoenvironmental Research 17 (25-102), Springer, Dordrecht.

Croudace, I. W., Rindby, A., and Rothwell, R. G. (2006). ITRAX: description and evaluation of a new multi-function X-ray core scanner. Geological Society, London, Special Publications, 267(1), 51–63.

Dahanayake, K., & Kulasena, N. (2008). Recognition of diagnostic criteria for recent- and Paleo-tsunami sediments from Sri Lanka. Marine Geology, 254(3-4), 180–186. https://doi.org/10.1016/j.margeo.2008.06.005

Dawson, A.G., and Stewart, I., 2007, Tsunami deposits in the geological record: Sedimentary Geology, v. 200, p. 166, doi: 10.1016/j.sedgeo .2007.01.002

De Martini, P. M., Barbano, M. S., Smedile, A., Gerardi, F., Pantosti, D., Del Carlo, P., & Pirrotta, C. (2010). A unique 4000 year long geological record of multiple tsunami inundations in the Augusta Bay (Eastern Sicily, Italy). Marine Geology, 276(1-4), 42–57. https://doi.org/10.1016/j.margeo.2010.07.005

Dewey, J. F., & Şengör, A. C. (1979). Aegean and surrounding regions: complex multiplate and continuum tectonics in a convergent zone. Geological Society of America Bulletin, 90(1), 84-92.

Dominey-Howes, D.T.M., Papadopoulos, G.A. ve Dawson, A.G., 2000a. Geological and Historical Investigation of the 1650 Mt. Columbo Eruption and Tsunami, Aegean Sea, Greece. Natural Hazards, 21, 83–96.

Dominey-Howes, D.T.M., Humphreys, G.S., and Hesse, P.P., 2006, Tsunami and palaeotsunami depositional signatures and their potential value in understanding the late-Holocene tsunami record: The Holocene, v. 16, p. 1095, doi: 10.1177/0959683606069400.

Donato, S.V., Reinhardt, E.G., Boyce, J.I., Rothaus, R., and Vosmer, T., 2008, Identifying tsunami deposits using bivalve shell taphonomy: Geology, v. 36, p. 199–202, doi: 10.1130/G24554A.1.

Dumont, J.F. ve Kerey, E,. 1975. Eğirdir Gölü Güneyi'nin Temel Jeolojik Etüdü: Türkiye Jeol. Kur. Bült., 18/2, 169-174.

Elbanna, A., Abdelmeguid, M., Ma, X., Amlani, F., Bhat, H., Synolakis, C., & Rosakis, A. (2020). Anatomy of strike slip fault tsunami-genesis. https://doi.org/10.31223/x57g72

El-Sayed, A., I. Korrat, and H.M. Hussein. 2004. Seismicity and seismic hazard in Alexandria (Egypt) and its surroundings. Pure and Applied Geophysics 161:1,003–1,019, http://dx.doi.org/ 10.1007/s00024-003-2488-8.

Emre, Ö., Doğan, A., & Özalp, S. (2011). 1:250.000 Ölçekli Türkiye Diri Fay Haritaları Serisi. Maden Tetkik ve Arama Genel Müdürlüğü, Ankara- Türkiye.

Ersoy, S., 1990. Batı Toros (Likya) Napları'nın Yapısal Öğelerinin ve Evriminin Analizi. Jeoloji Mühendisliği Dergisi, 37, 5 - 16.

Farınaccı, A. & Yeniay, G. 1986. Biostratigraphy and event-analysis of the Cenomanian-Maastrichtian carbonates of the Bey Dağları (western Taurus, Turkey). Geologica Romana 25, 257-284

Friedrich, W.L., Kromer, B., Friedrich, M., Heinemeier, J., Pfeiffer, T., and Talamo, S., 2006, Santorini eruption radiocarbon dated to 1627–1600 B.C.: Science, v. 312, p. 548, doi: 10.1126/science.1125087.

Garziglia, S., Migeon, S., Ducassou, E., Loncke, L., & Mascle, J. (2008). Mass-transport deposits on the Rosetta Province (NW Nile deep-sea turbidite system, Egyptian margin): Characteristics, distribution, and potential causal processes. Marine Geology, 250(3-4), 180–198. https://doi.org/10.1016/j.margeo.2008.01.016

Geist, E. L. & Zoback, M. L. 2002. Examination of the tsunami generated by the 1906 San Francisco Mw ¼ 7.8 earthquake, using new interpretations of the offshore San Andreas fault. In: PARSONS, T. (ed.) Crustal Structure of the Coastal and Marine San Francisco Bay Region. US Geological Survey Professional Papers, 1658, 29–42

Goff, J., Chagué-Goff, C., Nichol, S., Jaffe, B., & Dominey-Howes, D. (2012). Progress in Palaeotsunami research. Sedimentary Geology, 243-244, 70–88. https://doi.org/10.1016/j.sedgeo.2011.11.002

Goodman-Tchernov, B. N., Dey, H. W., Reinhardt, E. G., McCoy, F., & Mart, Y. (2009). Tsunami waves generated by the Santorini eruption reached Eastern Mediterranean shores. Geology, 37(10), 943-946.

Gusiakov, V.K. (2009). Tsunami history: recorded. The Sea 15, 23-53.

Günay, Y. Bölükbaşı, S. & Yoldemir, o. 1982. Beydağlarının Stratigrafisi ve Yapısı. Abstracts of the 6th Petroleum Congress of Turkey 91-101.

Hall, J., Aksu, A. E., Elitez, I., Yaltırak, C., & Çifçi, G. (2014). The Fethiye– Burdur Fault Zone: a component of upper plate extension of the subduction transform edge propagator fault linking Hellenic and Cyprus Arcs, Eastern Mediterranean. Tectonophysics, 635, 80-99

Haugen, K. B., Løvholt, F., & Harbitz, C. B. (2005). Fundamental mechanisms for tsunami generation by submarine mass flows in idealised geometries. Marine and Petroleum Geology, 22(1-2), 209–217. https://doi.org/10.1016/j.marpetgeo.2004.10.016

Heidarzadeh, M., S. Krastel, and A.C. Yalciner. 2014. The state-of-the-art numerical tools for modeling landslide tsunamis: A short review. Pp. 483–495 in Submarine Mass Movements and Their Consequences. Advances in Natural and Technological Hazards Research, vol. 37, http://dx.doi.org/10.1007/978-3-319-00972-8_43.

Hoffmann, N., Master, D., & Goodman-Tchernov, B. (2018). Possible tsunami inundation identified amongst 4–5th century BCE archaeological deposits at Tel Ashkelon, Israel. Marine Geology 396, 150-159.

House, J. E., & House, K. A. (2016). Halogens. Descriptive Inorganic Chemistry, 269–286. https://doi.org/10.1016/b978-0-12-804697-5.00017-8

Judd, K., Chagué-Goff, C., Goff, J., Gadd, P., Zawadzki, A., & Fierro, D. (2017). Multi-proxy evidence for small historical tsunamis leaving little or no sedimentary record. Marine Geology, 385, 204–215. https://doi.org/10.1016/j.margeo.2017.01.002

Kempf P, Moemaut J, Daele M V, Vandoorne W, Pino M, Urrutia R and De Batist M. (2017). Coastal lake sediments reveal 5500 years of tsunami history in south central Chile Quaternary Sci. Rev. 161 pp 99-116

Koçyiğit, A., 1981. Hoyran Gölü Yöresinin (Afyon- Isparta) Stratigrafik ve Tektonik Özellikleri: Ankara Üniv. Fen Fak., 1-30.

Koçyiğit, A. 1983. Hoyran gölü (Isparta büklümü) dolayının tektoniği. TJK. Bült., 26(1), 1-10.

Kovács, J. (2013). Flood deposits. Encyclopedia of Natural Hazards, 325–325. https://doi.org/10.1007/978-1-4020-4399-4_137

Lavigne, F., Paris, R., Leone, F., Gaillard, J. C., & Morin, J. (2013). Indian Ocean tsunami, 2004. Encyclopedia of Natural Hazards, 529–535. https://doi.org/10.1007/978-1-4020-4399-4_192

Leitmann, J. (2007). Cities and calamities: Learning from post-disaster response in Indonesia. Journal of Urban Health, 84(S1), 144–153. https://doi.org/10.1007/s11524-007-9182-6

Le Pichon, X., Angelier, J., (1979). The Hellenic arc and trench system: a key to the neotectonic evolution of the eastern Mediterranean area. Tectonophysics 60 (1), 1–42.

Le Pichon, X., & Kreemer, C. (2010). The Miocene-to-present kinematic evolution of the Eastern Mediterranean and Middle East and its implications for dynamics. Annual Review of Earth and Planetary Sciences, 38, 323-351.

Locat, J., & Lee, H. J. (2002). Submarine landslides: Advances and challenges. Canadian Geotechnical Journal, 39(1), 193–212. https://doi.org/10.1139/t01-089

Manning, S.W., Ramsey, C.B., Kutschera, W., Higham, T., Kromer, B., Steier, P., and Wild, E.M., 2006, Chronology for the Aegean Late Bronze Age 1700–1400 B.C.: Science, v. 312, p. 565–569, doi: 10.1126/science.1125682.

Masson, D. G., Harbitz, C. B., Wynn, R. B., Pedersen, G., & Løvholt, F. (2006). Submarine landslides: Processes, triggers and hazard prediction. Philosophical Transactions of the Royal Society A: Mathematical, Physical and Engineering Sciences, 364(1845), 2009–2039. https://doi.org/10.1098/rsta.2006.1810

Mastin, L., & Witter, J. (2000). The hazards of eruptions through lakes and seawater. Journal of Volcanology and Geothermal Research, 97(1–4), 195–214. https://doi.org/10.1016/S0377-0273(99)00174-2.

McCoy, F., and Heiken, G., 2000, Tsunami generated by the Late Bronze Age eruption of Thera (Santorini), Greece: Pure and Applied Geophysics, v. 157, p. 1227–1256, doi: 10.1007/s000240050024.

McKenzie, D., 1978. Active tectonics of the alpine—himalayan belt: the Aegean Sea and surrounding regions. Geophys. J. Int. 55 (1), 217–254.

McKenzie, D. (1972). Plate tectonics in the Mediterranean region. Nature, 226, 239-243.

Meltzner, A. J., Sieh, K., Abrams, M., Agnew, D. C., Hudnut, K. W., Avouac, J.-P., & Natawidjaja, D. H. (2006). Uplift and subsidence associated with the great aceh-andaman earthquake of 2004. Journal of Geophysical Research: Solid Earth, 111(B2). https://doi.org/10.1029/2005jb003891

Miller, D. J. [1960] Giant waves in Lituya Bay, Alaska, U. S. Geol. Survey, Prof. Paper354-C, 51–86.

Mimura, N., Yasuhara, K., Kawagoe, S., Yokoki, H., & Kazama, S. (2011). Damage from the Great East Japan earthquake and tsunami - A quick report. Mitigation and Adaptation Strategies for Global Change, 16(7), 803–818. https://doi.org/10.1007/s11027-011-9297-7

Minoura, K., Imamura, F., Kuran, U., Nakamura, T., Papadopoulos, G.A., Takahashi, T. & Yalciner, A.C. (2000). Discovery of Minoan tsunami deposits. Geology 28(1), 59-62.

Minoura K, Nakaya S (1991) Traces of tsunami preserved in inter-tidal lacustrine and marsh deposits: some examples from Northeast Japan. J Geol 99(2):265–287

Morimoto, R., & Osaka, J. (1955). The 1952–1953 submarine eruption of the Myojin Reef near the Bayonnaise Rocks, Japan. Bulletin of the Earthquake Research Institute, Tokyo University, 33(2), 221–250

Morton, R.A., Gelfenbaum, G., and Jaffe, B.E., 2007, Physical criteria for distinguishing sandy tsunami and storm deposits using modern examples: Sedimentary Geology, v. 200, p. 184, doi: 10.1016/j.sedgeo.2007.01.003.

Moore, A. L., McAdoo, B. G., & Ruffman, A. (2007). Landward fining from multiple sources in a sand sheet deposited by the 1929 Grand Banks Tsunami, Newfoundland. Sedimentary Geology, 200(3-4), 336–346. https://doi.org/10.1016/j.sedgeo.2007.01.012

Morhange, C., Marriner, N. & Pirazzoli, P.A. (2006). Evidence of Late-Holocene tsunami events in Lebanon. Zeitschrift fur Geomorphologie NF 146, 81-95.

Morton, R. A., Gelfenbaum, G., & Jaffe, B. E. (2007). Physical criteria for distinguishing Sandy Tsunami and storm deposits using modern examples. Sedimentary Geology, 200(3-4), 184–207. https://doi.org/10.1016/j.sedgeo.2007.01.003

Mountjoy, J., & Micallef, A. (2017). Submarine landslides. Submarine Geomorphology, 235–250. https://doi.org/10.1007/978-3-319-57852-1_13

Nakano, M., Unoki, S., Hanzawa, M., Marumo, R., & Fukuoka, J.(1954). Oceanographic features of a submarine eruption that destroyed the Kaiyo-Maru No. 5. Journal of Marine Research, 13(1), 48–66.

Nanayama, F., Furukawa, R., Shigeno, K., Makino, A., Soeda, Y., & Igarashi, Y. (2007). Nine unusually large tsunami deposits from the past 4000 years at Kiritappu Marsh along the Southern Kuril Trench. Sedimentary Geology, 200(3-4), 275–294. https://doi.org/10.1016/j.sedgeo.2007.01.008

National PoliceAgency,2011.The 2011off the Pacific coast of Tohoku Earthquake Damage Status and Measures by the Police, Public Information Document /http://www.npa.go.jp/archive/keibi/biki/ higaijokyo.pdf. (in Japanese).

Naz, H., Alkan, H., Erk, S., 1992. Facies and sequence characteristics of the Late Cretaceous-Paleocene drowning on the West Taurus Carbonate Platform, S.W. Türkiye. Proceedings of the 9th Petroleum Congress of Turkey, Ankara, 121–134.

Olsson, I. (1991). Accuracy and Precision in Sediment Chronology. Hydrobiologia 214, 25-34.

Öğretmen, N., Cosentino, D., Gliozzi, E., Cipollari, P., Iadanza, A. & Yildirim, C. (2015). Tsunami hazard in the Eastern Mediterranean: geological evidence from the Anatolian coastal area (Silifke, southern Turkey). Natural Hazards 79(3), 1569-1589.

Özgül, N. 1976. Torosların Bazı Temel jeoloji Özellikleri. Geological Society of Turkey Bulletin 14, 75-87 [in Turkish with English abstract].

Özkan S., & Köylüoğlu, M. 1988. Campanian-Maastrichtian planktonic foraminiferal biostratigraphy of the BeydaÛlarÝ Autochtonous Unit, Western Taurids, Turkey. Middle East Technical University, Journal of Pure and Applied Sciences 21, 377-388.

Papadopoulos GA, Gra`cia E, Urgeles R, Sallares V, De Martini PM, Pantosti D, Gonza´lez M, Yalciner AC, Mascle J, Sakellariou D, Salamon A, Tinti S, Karastathis V, Fokaefs A, Camerlenghi A, Novikova T, Papageorgiou A (2014) Historical and pre-historical tsunamis in the Mediterranean and its connected seas: geological signatures, generation mechanisms and coastal impacts.

Papadopoulos, G. (2016). Tsunamis in the Global Ocean. In: Papadopoulos, G. (ed), Tsunamis in the European-Mediterranean Region, Elsevier, 2016, Pages 1-37

Papazachos, B. C., & Papaioannou, C. A. (1999). Lithospheric boundaries and plate motions in the cyprus area. Tectonophysics, 308(1-2), 193–204. https://doi.org/10.1016/s0040-1951(99)00075-x

Pilarczyk, J. E., & Reinhardt, E. G. (2012). Testing foraminiferal taphonomy as a tsunami indicator in a shallow arid system lagoon: Sur, sultanate of Oman. Marine Geology, 295-298, 128–136. https://doi.org/10.1016/j.margeo.2011.12.002

Pirazzoli, P.A., Ausseil-Badie, J., Giresse, P., Hadjidaki, E., & Arnold, M. (1992). Historical environmental changes at Phalasarna harbor, West Crete. Geoarchaeology 7(4), 371-392.

Pirazzoli, P.A. (2005). A review of possible eustatic, isostatic and tectonic contributions in eight late-Holocene relative sea-level histories from the Mediterranean area. Quaternary Science Reviews 24(18-19), 1989-2001.

Poisson, A. 1977. Recherches geologiques dans les Taurides occidentals. These Doct. D'Etat, Universitie de Paris-Sud, Orsay, 795 p.

Putra, P. S. (2018). Tsunami sediments and their grain size characteristics. IOP Conference Series: Earth and Environmental Science, 118, 012035. https://doi.org/10.1088/1755-1315/118/1/012035

Ramirez-Herrera, M. T., Cundy, A., Kostoglodov, V., Carranza-Edwards, A., Morales, E., & Metcalfe, S. (2007). Sedimentary record of late-holocene relative sea-level change and tectonic deformation from the Guerrero Seismic Gap, Mexican Pacific Coast. The Holocene, 17(8), 1211–1220. https://doi.org/10.1177/0959683607085127

Reimer, P.J. (2013). Intcal13 and Marine13 Radiocarbon Age Calibration Curves, 0-50,000 Years Cal BP. Radiocarbon 55 (4), 1869-1887.

Reinhardt, E.G., Goodman, B.N., Boyce, J.I., Lopez, G., van Hengstum, P., Rink, W.J., Mart, Y., and Raban, A., 2006, The tsunami of 13 December A.D. 115 and the destruction of Herod the Great's harbor at Caesarea Maritima, Israel: Geology, v. 34, p. 1061–1064, doi: 10.1130/G22780A.1.

Republic of Indonesia, 2005. Main book of rehabilitation and reconstruction. In Master Plan for Rehabilitation and reconstruction for the Regions and People of the Province of Nanggroe Aceh Darussalam and Nias Islands of the Province of North Sumatra, Badan Rehabilitasi dan Rekonstruksi, Banda Aceh, Vol. 1 (13 Vol).

Ropp, R. C. (2013). Group 16 (O, S, Se, te) alkaline earth compounds. Encyclopedia of the Alkaline Earth Compounds, 105–197. https://doi.org/10.1016/b978-0-444-59550-8.00003-x

Rothwell, R.G., Hoogakker, B., Thomson, J., Croudace, I.W., Frenz, M., 2006. Turbidite emplacement on the southern Balearic Abyssal Plain (western Mediterranean Sea) during Marine Isotope Stages 1-3: an application of ITRAX XRF scanning of sediment cores to lithostratigraphic analysis. In: Rothwell, R.G. (Ed.), New techniques in sediment core analysis. Geological Society London Special Publication, London 267, pp. 79–98.

Ruiz, F., Abad, M., Cáceres, L. M., Rodríguez Vidal, J., Carretero, M. I., Pozo, M., & González-Regalado, M. L. (2010). Ostracods as tsunami tracers in Holocene sequences. Quaternary Research, 73(1), 130–135. https://doi.org/10.1016/j.yqres.2009.08.005

Salama, A., Meghraoui, M., Gabry, M. E., Maouche, S., Hussein, M. H., & Korrat, I. (2018). Paleotsunami deposits along the coast of Egypt correlate with historical earthquake records of eastern Mediterranean. Natural Hazards and Earth System Sciences, 18(8), 2203-2219.

Salamon, A., Hofsteter A, Garfunkel Z, Ron H. 1996. Seismicity of the Eastern Mediterranean region: Perspective from the Sinai subplate. Tectonophysics 263, 295–305.

Salamon, A., Rockwell, T., Ward, S. N., Guidoboni, E., & Comastri, A. (2007). Tsunami hazard evaluation of the eastern Mediterranean: historical analysis and selected modeling. Bulletin of the Seismological Society of America, 97(3), 705-724.

Scheffers, A., & Kelletat, D. (2004). Bimodal tsunami deposits–a neglected feature in paleo-tsunami research. Coastline Reports, 1, 67-75.

Scheffers, A., & Scheffers, S. (2007). Tsunami deposits on the coastline of west Crete (Greece). Earth and Planetary Science Letters 259(3-4), 613-624.

Schlichting, R., Peterson, C., 2006. Mapped overland distance of paleotsunami: high- velocity inundation in back-barrier wetlands of the central Cascadia margin, U.S.A. J. Geol. 114, 577–592

Scholz, C. H. (2019). The mechanics of earthquakes and faulting. Cambridge University Press.

Scott, E. (2021). Strike-slip tsunamis. Nature Reviews Earth & Environment, 2(6), 379–379. https://doi.org/10.1038/s43017-021-00179-3

Shah-Hosseini, M., Saleem, A., Mahmoud, A. M. A., & Morhange, C. (2016). Coastal boulder deposits attesting to large wave impacts on the Mediterranean coast of Egypt. Natural Hazards, 83(2), 849-865.

Sigurdsson, H., and 12 others, 2006, Submarine volcaniclastic deposits associated with the Minoan eruption of Santorini volcano, Greece: Eos (Transactions, American Geophysical Union), v. 87, p. 26.

Softa, M., Turan, M., & Sözbilir, H. (2018). Jeolojik, arkeolojik ve Arkeosismolojik Veriler ışığında Myra Antik kenti'nde tarihsel Depremlere Ait Deformasyon Verileri, GB Anadolu. Türkiye Jeoloji Bülteni / Geological Bulletin of Turkey, 52–73. https://doi.org/10.25288/tjb.358177

Stanley, J. D., & Pia Bernasconi, M. (2006). Holocene depositional patterns and evolution in Alexandria's Eastern Harbor, Egypt. Journal of Coastal Research, 283-297.

Sugawara, D., Minoura, K., & Imamura, F. (2008). Tsunamis and tsunami sedimentology. In Tsunamiites (pp. 9-49). Elsevier.

Summary Statement from the Japan - UNESCO - UNU Symposium on The Great East Japan Tsunami on 11 March 2011 and Tsunami Warning Systems: Policy Perspectives 16 - 17 February 2012 UNESCO/IOC 2012.

Suppasri, A., Imamura, F., & Koshimura, S. (2012). Tsunamigenic ratio of the Pacific Ocean earthquakes and a proposal for a tsunami index. Natural Hazards and Earth System Sciences, 12(1), 175–185. https://doi.org/10.5194/nhess-12-175-2012

Şahoğlu, V., Sterba, J. H., Katz, T., Çayır, Ü., Gündoğan, Ü., Tyuleneva, N., Tuğcu, İ., Bichler, M., Erkanal, H., & Goodman-Tchernov, B. N. (2021). Volcanic Ash, victims, and tsunami debris from the late bronze age thera eruption discovered at çeşme-Bağlararası (Turkey). Proceedings of the National Academy of Sciences, 119(1). https://doi.org/10.1073/pnas.2114213118

Şengör, A.M.C., Yilmaz, Y., 1981. Tethyan evolution of Turkey: a plate tectonic approach. Tectonophysics 75 (3–4), 181193203–190199241.

Tan, A., Chilvery, A. K., Dokhanian, M., & Crutcher, S. H. (2012). Tsunami propagation models based on First principles. Tsunami - Analysis of a Hazard - From Physical Interpretation to Human Impact. https://doi.org/10.5772/50508

Tanioka, Y., & Satake, K. (1996). Tsunami generation by horizontal displacement of Ocean Bottom. Geophysical Research Letters, 23(8), 861–864. https://doi.org/10.1029/96gl00736

Tappin, D. R. (2017a). The generation of Tsunamis. Encyclopedia of Maritime and Offshore Engineering, 1–10. https://doi.org/10.1002/9781118476406.emoe523

Tappin, D. R. (2017b). Tsunamis from submarine landslides. Geology Today, 33(5), 190–200. https://doi.org/10.1111/gto.12200

Tjallingii R, Röhl U, Kölling M, Bickert T (2007) Influence of the water content on X-ray fluorescence core-scanning measurements in soft marine sediments. Geochem Geophy Geosy 8:Q02004. https ://doi. org/10.1029/2006G C0013 93

Tongkul, F., Roslee, R., & Mohd Daud, A. K. (2020). Assessment of tsunami hazard in Sabah – level of threat, constraints and future work. Bulletin Of The Geological Society Of Malaysia, 70(1), 1–15. https://doi.org/10.7186/bgsm70202001

Tsuji, Y., Okamura, M., Matsuoka, H., Goto, T., & Hang, S. (2002). Traces of historical and prehistorical tsunamis in the lake-bottom sedimentary sequences at Oh-Ike (Owase City) and Suwa-Ike (Kii-Nagashima Town), Mie Prefecture. Chikyu Monthly 280, 743–747. (In Japanese)

Vött, A., Bruins, H. J., Gawehn, M., Goodman-Tchernov, B. N., De Martini, P., M., Kelletat, D., ... & Willershäuser, T. (2018). Publicity waves based on manipulated geoscientific data suggesting climatic trigger for majority of tsunami finding in the Mediterranean – Response to 'Tsunamis in the geological record: Making waves with a cautionary tale from the Mediterranean' by Marriner et al. (2017). Zeitschrift für Geomorphologie, Supplementary Issues, 62(2), 7-45.

Walton, W. R., & Sloan, B. J. (1990). The genus Ammonia Bruennich, 1772; its geographic distribution and morphologic variability. The Journal of Foraminiferal Research, 20(2), 128–156. https://doi.org/10.2113/gsjfr.20.2.128

Ward, S.N., & Day, S. (2010). The 1958 Lituya Bay landslide and tsunami — a tsunami ball approach. Journal of Earthquake and Tsunami, 04(04), 285–319. https://doi.org/10.1142/s1793431110000893

Werner, V., Baika, K., Fischer, P., Hadler, H., Obrocki, L., Willershäuser, T., & Emde, K., (2018). The sedimentary and geomorphological imprint of the AD 365 tsunami on the coasts of southwestern Crete (Greece)–Examples from Sougia and Palaiochora. Quaternary International 473, 66-90.

Whelan, F., & Kelletat, D. (2002). Geomorphic evidence and relative and absolute dating results for tsunami events on Cyprus. Science of Tsunami Hazards 20(1), 3-16

Wünnemann, K., & Weiss, R. (2015). The meteorite impact-induced tsunami hazard. Philosophical Transactions of the Royal Society A: Mathematical, Physical and Engineering Sciences, 373(2053), 20140381. https://doi.org/10.1098/rsta.2014.0381

Yalciner, A., Zaytsev, A., Aytore, B., Insel, I., Heidarzadeh, M., Kian, R., & Imamura, F. (2014). A possible submarine landslide and associated tsunami at the Northwest Nile Delta, Mediterranean Sea. Oceanography, 27(2), 68–75. https://doi.org/10.5670/oceanog.2014.41

Yeniçeri, M.T. (2020). Geochemical Traces of Historical Eastern Mediterranean Tsunamis in the Sediments of Ölüdeniz Lagoon, SW Turkey. (MSc Thesis, Middle East Technical University).

Yolsal S, Taymaz T, Yalcıner AC (2007) Understanding tsu- namis, potential source regions and tsunami-prone mech- anisms in the Eastern Mediterranean. In: Taymaz T et al (eds) The Geodynamics of the Aegean and Anatolia, vol 291. Geol Soc Spec Publ, London, pp 201–230.